



Schweizerische Eidgenossenschaft  
Confédération suisse  
Confederazione Svizzera  
Confederaziun svizra

Swiss Confederation

Federal Department of Home Affairs FDHA  
**Federal Office of Meteorology and Climatology MeteoSwiss**

**Scientific Report MeteoSwiss No. 93**

# **The HeliMont Surface Solar Radiation Processing**

Reto Stöckli





**ISSN: 1422-1381**

**Scientific Report MeteoSwiss No. 93**

# **The HeliMont Surface Solar Radiation Processing**

Reto Stöckli

*This report is dedicated to Antoine Zelenka and Bruno Dürr. Antoine Zelenka has set a scientific milestone to properly include terrain effects in satellite-based surface radiation calculations. And yet, we neither fully reached nor passed this milestone as shown in the outlook of this report. Bruno Dürr has set a solid foundation for many technical implementations of this report.*

**This report dates from February 27, 2014 and is based on “HeliMont” version 2.1.1.**

**Recommended citation:**

Reto Stöckli: 2013, The HeliMont Surface Solar Radiation Processing, *Scientific Report MeteoSwiss*, 93, 123 pp.

**Editor:**

Federal Office of Meteorology and Climatology, MeteoSwiss, © 2013

**MeteoSwiss**

Krähbühlstrasse 58  
8044 Zürich  
T +41 44 256 91 11  
[www.meteoswiss.ch](http://www.meteoswiss.ch)



## Abstract

Surface incoming solar (SIS) radiation, also referred to as shortwave global irradiance, is an essential climate variable and highly relevant for applications in the fields of climate monitoring, solar energy or agriculture. SIS can be retrieved from geostationary satellite sensors with a continuous spatial and temporal coverage and thus complements station-based estimates. This report documents the “HeliMont” methodology which was developed at MeteoSwiss within the EUMETSAT Satellite Application Facility on Climate Monitoring (CM SAF) project to calculate SIS including its components from Meteosat Second Generation (MSG) Spinning Enhanced Visible and Infrared Imager (SEVIRI) data. The algorithm extends the Heliosat approach to climatological SIS retrieval over mountainous regions and for bright surface targets. The algorithm includes a self-consistent probabilistic cloud mask and a diurnally consistent parametric clear sky compositing. It explicitly separates clouds from snow and includes a physically-based calculation of the clear sky atmosphere. Meter-scale SIS maps can be derived from the kilometer-scale satellite grid by accounting for terrain shadowing, sky view and local plane tilt and aspect angles. Validation results suggest that the resulting gridded SIS dataset has a monthly averaged uncertainty of  $< 5 \text{ W m}^{-2}$  over flat surfaces and  $< 10 \text{ W m}^{-2}$  over mountainous terrain, since it overcomes most terrain and snow related issues found in comparable datasets. Both the methodology and the dataset are now applied in solar energy assessments such as the EU Interreg PV-ALPS project, where the solar energy potential of the Swiss Canton Graubünden and the Italian Region South Tyrol is evaluated.



Le opportunità non hanno confini

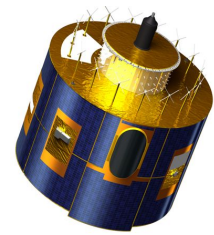
# Contents

<b>Abstract</b>		<b>5</b>
<b>1</b>	<b>Introduction</b>	<b>9</b>
<b>2</b>	<b>Algorithm Overview</b>	<b>11</b>
<b>3</b>	<b>Satellite Data</b>	<b>14</b>
3.1	Geographical Subsetting . . . . .	14
3.2	Reading Digital Numbers . . . . .	15
3.3	Calculating Radiances . . . . .	15
3.4	Calculating Brightness Temperatures . . . . .	16
3.5	Calculating Reflectances . . . . .	16
3.6	Combining Narrow-Band Channels . . . . .	17
3.7	Regridding Infrared Channels . . . . .	17
3.8	Calculating Scan Time . . . . .	18
<b>4</b>	<b>Navigation</b>	<b>19</b>
<b>5</b>	<b>Cloud Masking</b>	<b>21</b>
5.1	Temperature Score . . . . .	22
5.2	Brightness Score . . . . .	23
5.3	Reflectance Score . . . . .	23
5.4	Simple Ratio Score . . . . .	23
5.5	Spatial Texture Uniformity Score . . . . .	24
5.6	Spatial Temperature Uniformity Score . . . . .	24
5.7	Cirrus Score . . . . .	24
5.8	Temporal Temperature Uniformity Score . . . . .	25
5.9	Diurnal Temperature Uniformity Score . . . . .	25
5.10	NDSI Score . . . . .	25
5.11	Freeze Score . . . . .	26
5.12	Snow Detection . . . . .	26
5.13	Cloud Detection . . . . .	27
5.14	Update of Clear Sky Fields . . . . .	28
<b>6</b>	<b>Clear Sky Compositing</b>	<b>30</b>
6.1	Reflectance . . . . .	30
6.2	Brightness Temperature . . . . .	32
6.2.1	Mannstein Model . . . . .	34
6.2.2	Göttsche Model . . . . .	35
6.3	Snow Mask . . . . .	38
6.4	Surface Albedo . . . . .	38
<b>7</b>	<b>Clear Sky Radiation</b>	<b>39</b>
7.1	Kasten Clear Sky Model . . . . .	39
7.2	gnu-MAGIC Clear Sky Model . . . . .	40

<b>8</b>	<b>All Sky Radiation</b>	<b>42</b>
8.1	Maximum Cloud Reflectance . . . . .	42
8.2	Cloud Index (Visible) . . . . .	43
8.3	Cloud Index (IR) . . . . .	44
8.4	Cloud Index (Combined) . . . . .	45
8.5	Clear Sky Index . . . . .	46
8.6	Shadows from Terrain . . . . .	46
8.7	Shadows from Tilted Planes . . . . .	47
8.8	Shadows from Clouds . . . . .	47
8.9	Surface Radiation . . . . .	49
8.9.1	Kasten-based Surface Radiation . . . . .	49
8.9.2	gnu-MAGIC-based Surface Radiation . . . . .	50
8.10	Radiation in Terrain . . . . .	50
8.11	Radiation on a Tilted Plane . . . . .	50
8.12	Global Radiation . . . . .	51
8.13	Sunshine Duration . . . . .	51
<b>9</b>	<b>Static Boundary Conditions</b>	<b>52</b>
9.1	Water Mask . . . . .	52
9.2	Elevation . . . . .	52
9.3	Terrain Aspect and Slope . . . . .	53
9.4	Horizon . . . . .	54
9.5	Sky View Factor . . . . .	55
9.6	Satellite View Angles . . . . .	56
<b>10</b>	<b>Dynamic Boundary Conditions</b>	<b>60</b>
10.1	Sun-Earth Distance . . . . .	60
10.2	Sun View Angles . . . . .	60
10.3	Angle between the sun and normal to the plane . . . . .	61
10.4	Sun-Satellite Angles . . . . .	62
<b>11</b>	<b>Geographic Projections</b>	<b>64</b>
11.1	Meteosat First Generation (forward) . . . . .	64
11.2	Meteosat First Generation (inverse) . . . . .	64
11.3	Meteosat Second Generation (forward) . . . . .	64
11.4	Meteosat Second Generation (inverse) . . . . .	64
11.5	Swiss Orthographic (forward) . . . . .	64
11.6	Swiss Orthographic (inverse) . . . . .	65
11.7	Orthographic (forward) . . . . .	65
11.8	Orthographic (inverse) . . . . .	65
11.9	Rotated Pole (forward) . . . . .	66
11.10	Rotated Pole (inverse) . . . . .	66
11.11	Reprojection . . . . .	66
<b>12</b>	<b>Geometric Projections</b>	<b>68</b>
12.1	Orthorectification . . . . .	68

12.2	Cloud Height . . . . .	69
<b>13</b>	<b>Climatological Compositing</b>	<b>70</b>
13.1	Daily, Monthly and Yearly Mean Values . . . . .	70
13.2	Spatial Downscaling . . . . .	70
13.3	Radiation on a Tilted Plane from Monthly Mean Data . . . . .	70
<b>14</b>	<b>Miscellaneous Algorithms</b>	<b>73</b>
14.1	Temporal Variance . . . . .	73
14.2	Spatial Variance . . . . .	73
<b>15</b>	<b>Validation</b>	<b>75</b>
15.1	Validation with Alpine Surface Radiation Budget network data . . . . .	75
15.2	Validation with Baseline Surface Radiation Network data . . . . .	78
15.3	Validation with SwissMetNet data . . . . .	81
15.4	Validation of Radiation Components . . . . .	83
15.5	Validation of Clear Sky Radiation . . . . .	87
<b>16</b>	<b>Intercomparison</b>	<b>89</b>
16.1	Intercomparison with Duerr et al. 2009 . . . . .	89
16.2	Intercomparison with HelioClim . . . . .	91
16.3	Inter-comparison with ISCCP and GEWEX . . . . .	93
16.4	Intercomparison with ECMWF ERA Interim . . . . .	95
16.5	Intercomparison with CM SAF . . . . .	97
<b>17</b>	<b>Outlook and Suggestions for Improvements</b>	<b>100</b>
17.1	Radiance Inter-Calibration . . . . .	100
17.2	Satellite Sensors . . . . .	101
17.3	Cloud Masking . . . . .	101
17.4	Clear Sky Compositing . . . . .	101
17.5	Cloud Index . . . . .	102
17.6	Surface Radiation . . . . .	102
17.7	Cloud Parallax . . . . .	103
17.8	Bias Correction . . . . .	103
17.9	Uncertainties . . . . .	104
<b>18</b>	<b>Applications</b>	<b>105</b>
	<b>Abbreviations</b>	<b>106</b>
	<b>List of Figures</b>	<b>109</b>
	<b>List of Tables</b>	<b>111</b>
	<b>References</b>	<b>113</b>
	<b>Acknowledgment</b>	<b>120</b>





## 1 Introduction

Climate monitoring has become a scientific endeavor largely driven by societal needs to quantify the effects, mitigate the extent and adapt to the consequences of climate variability and change (Solomon *et al.*, 2007). In turn, homogeneous long term climate data records (CDR's) increasingly serve a wide range of users including inter-disciplinary scientists, decision-makers, resource managers and the private sector (Overpeck *et al.*, 2011). In order to satisfy those needs and guarantee an international coordination for climatological measurements, a set of essential climate variables (ECV's) are defined by the Global Climate Observing System (GCOS) as part of the World Meteorological Organization (WMO) as requested by the United Nations Framework Convention on Climate Change (UNFCCC) (GCOS, 2010).

Among all ECV's, the earth radiation budget, and specifically SIS, can be accurately derived from satellite sensor observations with a significant contribution to the global observing system and with a "high impact to the UNFCCC requirements" (GCOS, 2011). The accurate knowledge of SIS is essential for climate monitoring and climate model evaluation (Wild *et al.*, 1995, 2001; Babst *et al.*, 2008; Jimenez-Munoz *et al.*, 2012; Philipona, 2012; Posselt *et al.*, 2012). In addition, SIS data has substantial socio-economic value since it is used in many application areas in the public and private sector. This for instance includes the site-evaluation for solar energy power plants, the planning and management of electricity grids, solar cadasters, the real-time monitoring of solar energy production, the estimation of crop yield, agricultural pest and disease monitoring or for calculating the energy use of buildings.

MeteoSwiss has built the expertise to derive climate data records of SIS and its components from geostationary satellite sensor data within the EUMETSAT Satellite Application Facility on Climate Monitoring (CM SAF) (Schulz *et al.*, 2009). During the Continuous Development and Operations Phase (CDOP I, 2007-2012) MeteoSwiss and the German Weather Service (DWD) generated a thematic climate data record (TCDR) of SIS, surface incoming direct (SID) radiation and cloud albedo (CAL) from Meteosat First Generation (MFG) data covering the full Meteosat disk (Posselt *et al.*, 2012). MeteoSwiss also evaluated methods useful to bridge several satellite generations which will be used by CM SAF during CDOP II (2012-2017) to build a 30+ year long SIS TCDR (Posselt *et al.*, 2011). Due to its focus on Alpine meteorology and climatology MeteoSwiss has also created algorithms which are specifically suited to retrieve SIS from MSG data over complex terrain (Dürr and Zelenka, 2009; Dürr *et al.*, 2010).

MeteoSwiss takes part of the EU Interreg PV-ALPS project (2012-2014) where the solar energy potential for the Alpine regions of Trento (northern Italy) and Graubünden (eastern Switzerland) is evaluated for supporting the planning of solar energy applications at the communal level. Within this

project MeteoSwiss is responsible for generating the regional climatological satellite data useful for mapping the communal solar energy potential in the selected mountainous areas (Figure 1).

This report documents the “HeliMont” algorithm used by MeteoSwiss to retrieve SIS and its components for the PV-ALPS project. The report includes a validation section which provides evidence for the accuracy of these algorithms in the Swiss Alps and for a set of non-mountainous validation sites covering a wide climatic range distributed over Europe, Africa and the West Indies.

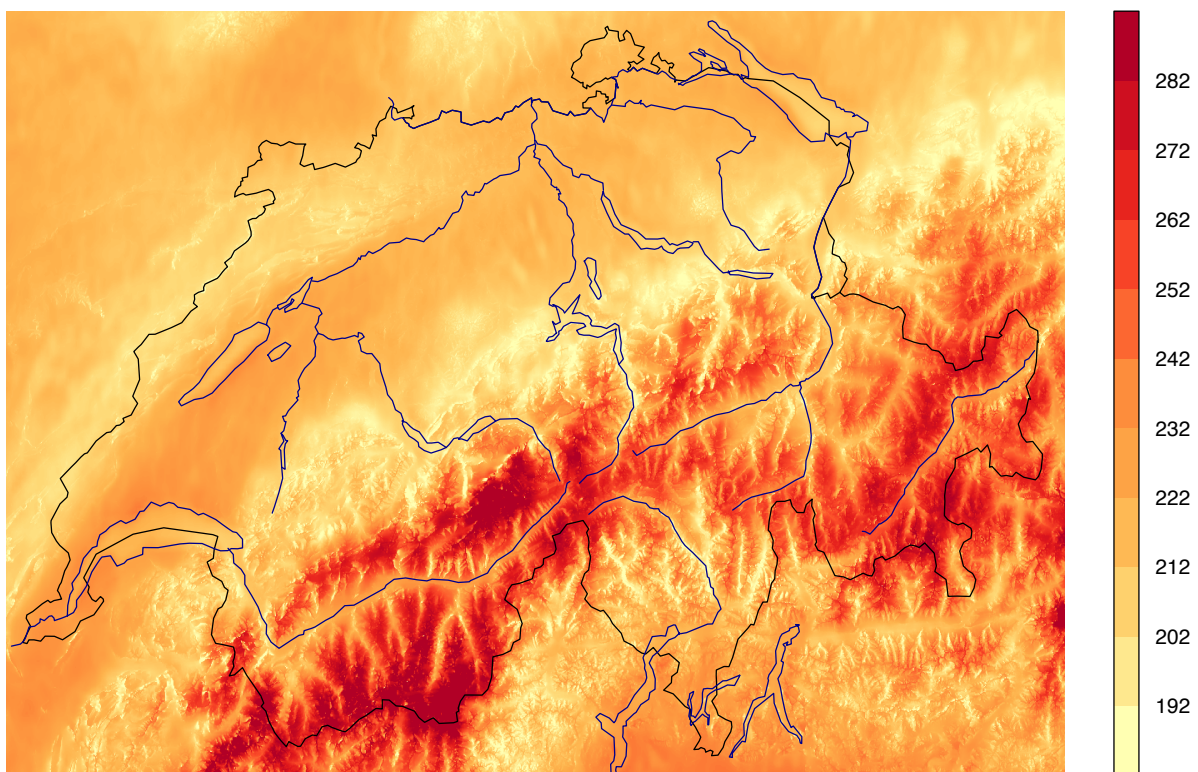


**Figure 1:** Monthly Global Radiation Climatology for May (2004-2011,  $\text{W m}^{-2}$ ) over Switzerland calculated from the MSG SEVIRI HRV channel and with a 100 m spatially resolved terrain model.

## 2 Algorithm Overview

The algorithms described in this report are part of a general processing framework, referred to as “HeliMont”. It provides a foundation suitable for the retrieval of terrestrial, atmospheric, oceanic and cryospheric variables from passive imaging spectro-radiometer sensors on geostationary platforms. It is currently configured (and limited) to perform cloud masking, clear sky compositing and to calculate SIS and its components from MSG SEVIRI data with special attention to the requirements in Alpine terrain. Strong topographic variability in combination with snow cover often substantially decreases the quality of physical variables derived from passive imaging spectro-radiometer data. In order to derive the all-sky forcing on surface radiation from satellite data, the clear sky state (“also termed as background state”) has to be known beforehand. Clear sky compositing is used to estimate the most likely cloudless appearance of the earth’s surface by merging previously cloud masked satellite pixels covering a time period into the past. However, most cloud mask algorithms are not able to consistently separate clouds from snow and planetary boundary layer inversions complicate the thermal separation of low-level clouds (i.e. fog) from the clear sky surface. The clear sky state can thus become contaminated by clouds. In mountainous terrain model-based column-integrated atmospheric boundary conditions are often inadequate in their horizontal scale. In addition, terrain shadow, sky view and the contribution of reflected radiation from the surrounding terrain have to be properly accounted for when calculating SIS from satellite data over mountainous terrain.

“HeliMont” calculates SIS and its components by use of a modified version of the classical Heliosat algorithm (*Möser and Raschke, 1984; Cano et al., 1986; Beyer et al., 1996; Ineichen and Perez, 1999; Hammer et al., 2003; Müller et al., 2004; Posselt et al., 2012*). It employs the MSG SEVIRI High Resolution Visible (HRV; 0.45-1.1  $\mu\text{m}$ ) channel in combination with five other near-infrared and infrared channels (0.6, 0.8, 1.6, 10.8, 12.0  $\mu\text{m}$ ). The MSG SEVIRI data starts in the year 2004 and can be continuously updated. “HeliMont” could optionally be operated with two channels only (HRV and 10.8  $\mu\text{m}$ ) in order to extend the short MSG SEVIRI climatology back in time with MFG MVIRI data (1983–2005). Since the HRV channel is not available on the full Meteosat disk, a broad band visible channel can alternatively be simulated from the two narrow band visible channels (0.6 and 0.8  $\mu\text{m}$ ) by use of the linear combination proposed by *Deneke and Roebeling (2010)*. Geostationary sensors like MVIRI or SEVIRI provide a high temporal resolution with at least half-hourly “slots” (time steps). They are especially suitable to calculate surface radiation fluxes which depend on diurnally highly variable cloud cover.

“HeliMont” relies on inter-calibrated radiances. They are increasingly being provided by space agencies, also for heritage sensors by an WMO coordinated initiative called the Global Space-Based Inter-Calibration System GSICS (*Goldberg et al., 2011*). Thus, instead of raw Meteosat digital counts, physical variables such as reflectances and brightness temperatures are used in all calculations.

The most important part of each passive imaging satellite sensor processing is the ability to separate cloudy from clear sky states. Such a 'cloud mask' is required independently of whether atmospheric, oceanic, cryospheric or terrestrial variables are calculated. For most terrestrial or oceanic applications a clear sky conservative approach is preferred (no clouds allowed, not even partial ones), while for the retrieval of cloud properties a cloud conservative approach has to be used. A new probabilistic cloud mask based on the aggregated rating approach (*Khlopenkov and Trishchenko, 2007*) is used here. In comparison to most decision-tree based cloud masks it provides a continuous field of cloudiness called cloud rating. The cloud rating can be tailored by the downstream application depending on whether a cloud or clear sky conservative cloud screening is needed. It also provides a measure of cloud mask uncertainty and it can operate from two to five channels with increasing quality. The cloud mask is extended here with temporal variance tests for low stratus and thin cloud detection and by making it largely independent from external (model-based) boundary conditions through the concurrent generation of background fields. For each time step the cloud mask performs a clear sky conservative separation of clear sky reflectances and brightness temperatures. At the end of each day they are composited by use of a non-linear parametric fit, weighted by the cloud mask uncertainty. This yields a consistent diurnal course of clear sky reflectance and brightness temperature which in turn serves as the updated background field for the next day's cloud mask. These extensions are only possible with geostationary satellite data since they feature a high (sub-hourly) temporal resolution. The result is a cloud mask which is optimally suited for mountainous conditions where model-based background fields are usually inappropriate in scale.

The all sky incident surface solar radiation fluxes at the earth's surface are calculated by combining the clear sky surface radiation fluxes from a radiative transfer model with the radiative cloud forcing derived from satellite data. This method is commonly referred to as "Heliosat" (*Cano et al., 1986*). It has been developed in the late 1970's for deriving surface solar irradiance from the National Oceanographic and Atmospheric Administration (NOAA) Geostationary Operational Environmental Satellite (GOES) (*Vonder Haar and Ellis, 1978; Tarpley, 1979; Gautier et al., 1980*) and was successively adapted for the EUMETSAT MFG satellite (*Möser and Raschke, 1984*). Heliosat relies on the so-called "cloud index" which exploits the radiative properties of clouds in the visible solar spectrum. When viewed from space, the cloud transmittance is inversely related to the cloud reflectance. The cloud index is thus a surrogate for the radiative cloud forcing in the shortwave solar spectrum. It empirically accounts for the absorption, reflection and scattering of solar radiation in clouds under the assumption that clouds are substantially brighter than the underlying surface.

The cloud index however fails for bright surfaces such as snow covered land or low latitude deserts since they can have a higher reflectance than the overlying clouds. The following modifications are thus made to the Heliosat cloud index, which generally relies on a single visible channel only (*Möser and Raschke, 1984; Posselt et al., 2012*). In "HelioMont" the visible broad-band and the infrared 10.8  $\mu\text{m}$  channels, and optionally the near-infrared 1.6  $\mu\text{m}$  channel, are used to calculate both a visible and an infrared-based cloud index. The infrared cloud index replaces the visible (classical) cloud index over bright surfaces. Also, using both the visible and infrared channels for heritage sensors like MVIRI maximizes the use of available information, specifically for cloud screening and clear sky compositing. The Heliosat cloud index relies on the accurate retrieval of the clear sky reflectance as a reference for cloud free situations. Often a slot-wise approach is used to composite the clear sky reflectance for each time step from e.g. the last month's reflectance values. In "HelioMont" the clear sky compositing calculates a diurnal course of the clear sky reflectance and the clear sky brightness temperature from

cloud masked reflectance and brightness temperature values of the previous days. This guarantees that the clear sky reflectance and brightness temperature values have consistency on the diurnal time scale. This also enables to account for short-term changes in surface reflectance, such as during green-up or during periods of snow fall. Heliosat relies on the characterization of the maximum cloud reflectance as a tuning parameter. Often a self-calibrating procedure is used which analyzes the reflectance of the brightest clouds by for instance deriving the 95% percentile from the reflectance distribution for a given month (*Dürr and Zelenka, 2009; Posselt et al., 2012*). In “HelioMont” the maximum cloud reflectance depends on solar- and view-geometry. Maximum cloud reflectance fields are calculated with a radiative transfer model simulating the radiative properties of ice and water clouds with an optical thickness of 128 at each time step (*Mayer and Kylling, 2005*). In “HelioMont” the maximum cloud reflectance is thus spatially distributed and relies on inter-calibrated radiances.

The clear sky surface radiation is often calculated by use of simplified models of the cloud free atmosphere (*Kasten, 1996; Rigollier et al., 2000; Ineichen and Perez, 2002; Rigollier et al., 2004*). The atmospheric state in these models is characterized by a single integrated turbidity value, the so-called Linke Turbidity (*Linke, 1922*). Climatological Linke Turbidity maps are available on global scale based on surface radiation and aerosol measurements (*Remund et al., 2003*). However, a single atmospheric turbidity parameter cannot account for the molecular absorption and scattering effects of the individual atmospheric constituents on global radiation and its components (*Müller et al., 2004*). Also, the climatological state of the atmosphere can strongly deviate from its instantaneous state with adverse effects on the quality of the calculated clear sky solar radiation fluxes. We thus make use of a radiative transfer model (*Mayer and Kylling, 2005*), parameterized by the so-called Modified Lambert-Beer (MLB) set of equations in combination with a look-up table (LUT) for efficient processing (*Müller et al., 2009*). Specifically, a modified version of the publicly available gnu-MAGIC algorithm (<http://sourceforge.net/projects/gnu-magic/>) with a re-calculated LUT is used. It is constrained by 6-hourly total column water vapor and ozone data from the European Centre for Medium-range Weather Forecast (ECMWF) and by use of a monthly aerosol climatology (*Kinne, 2008*).

SIS and components are calculated by use of a SRTM-based digital elevation model (*Jarvis et al., 2004*). Either the grid-scale or location-specific horizon and sky view factor are derived first. They are then used to calculate the radiative effects of terrain shadowing on the direct radiation and the effects of decreased sky view on the diffuse radiation. The diffuse radiation is augmented with the radiation reflected from the surrounding terrain, which is especially important for snow-covered surfaces. Surface radiation components can optionally be calculated for tilted surfaces such as mountain slopes, solar panels or building facades.

## 3 Satellite Data

The time-varying input data for the “HelioMont” processing consists of 15’ or 30’ Level 1.5 satellite data in the Native (*EUMETSAT*, 2010) or CineSat (<http://www.cinesat.com/>) format for MSG or OpenMTP (*EUMETSAT*, 2000) format for MFG. The CineSat data is a transformed HRIT data stream from the real-time EUMETCast service while the other data sources can be ordered from the EUMETSAT archive. The satellite data is first tailored to the selected geographical domain. Next, radiances, brightness temperatures (for thermal channels) and reflectances (for solar channels) are calculated. Finally, and if applicable, low-resolution visible (VIS), near-infrared (NIR), water vapor (WV) and infrared (IR) channels need to be co-registered on the same grid as the high resolution visible (HRV) channel.

### 3.1 Geographical Subsetting

The geographic boundaries of the selected region, defined by either a longitude/latitude pair in regular or rotated pole coordinates or by specifying metric boundaries in the Swiss or UTM metric grid, are transformed into the Meteosat First or Second generation line/column extent by use of the inverse projection routines given in Section 11.

Meteosat lines start at the southern, and columns at the eastern boundary of the disk. For MSG they range from 1-3712 for regular VIS, NIR and IR channels and from 1-11136 for the HRV channel. MFG lines and columns range from 1-2500 for the WV and IR channels and from 1-5000 for the VIS channel. Columns and all channel data are reversed from east-west direction to west-east direction prior to all processing. Thus, column indices decrease with increasing horizontal pixel count.

If the MSG HRV channel is used in combination with the regular VIS,IR channels, the corresponding column and line extents of the latter can be derived from the HRV column and line extents:

$$\text{col}_{\min}^{\text{VIS,IR}} = \text{round}((\text{col}_{\min}^{\text{HRV}} + 2)/3) \quad (1)$$

$$\text{lin}_{\min}^{\text{VIS,IR}} = \text{round}((\text{lin}_{\min}^{\text{HRV}} + 2)/3) \quad (2)$$

$$\text{col}_n^{\text{VIS,IR}} = \text{round}((\text{col}_n^{\text{HRV}} + 1)/3) \quad (3)$$

$$\text{lin}_n^{\text{VIS,IR}} = \text{round}((\text{lin}_n^{\text{HRV}} + 1)/3). \quad (4)$$

The HRV channel grid corresponds to the VIS,IR channel by shifting it by 2 high resolution pixels to the east and south before dividing by the resolution factor (3). The above formula calculates the VIS,IR channel domain extents corresponding to the HRV channel domain extents. A subgrid-scale inter-channel co-registration (Section 3.7) is carried out for regridding the VIS,IR channels to the HRV

channel resolution as for instance needed for simultaneously analyzing the HRV and VIS,IR channels during cloud masking.

The navigation shifts  $\Delta x$  and  $\Delta y$  (Section 4) are added to the line/column extents. For MSG, if the HRV channel is used in combination with regular VIS,IR channels, 1/3 of the correct navigation shifts  $\Delta x$  and  $\Delta y$  are also added to  $\text{col}_{\min}^{\text{VIS,IR}}$  and  $\text{lin}_{\min}^{\text{VIS,IR}}$ .

### 3.2 Reading Digital Numbers

Level 1.5 (L 1.5) files contain data stored as Digital Numbers (DN). These are sensor counts packed by EUMETSAT to 8, 10 or 16 integer bits by correcting image artifacts, applying gain corrections and post-launch calibration to the sensor data and reprojecting the data to a pre-defined satellite grid based on a 0 degree longitude sub-satellite point (SSP). More details on the MSG L1.5 data format can be found in *EUMETSAT* (2010). A DN= 0 is interpreted as missing data.

During maneuvers or satellite reconfiguration the geometric or radiometric quality of the SEVIRI data may not be adequate for deriving physical products. Various status and quality flags in the Native Level 1.5 header and trailer data are used to identify such periods:

- start and end times of planned satellite maneuvers are given a few hours or even days in advance and allow the exact screening of data;
- the geometric quality has to be at least 2 (for details see code);
- radiometric quality is not evaluated;
- satellite status has to be either “operational” or “commissioning”.

### 3.3 Calculating Radiances

The MSG Level 1.5 data comes with slope and offset parameters (similar to the NetCDF CF-Convention) which enable the unpacking of the DN into radiance values ( $\text{mW m}^{-2} \text{sr}^{-1} (\text{cm}^{-1})^{-1}$ ):

$$R = \text{slope} \cdot \text{DN} + \text{offset} \quad (5)$$

Slope and offset parameters are applied per channel and need to be extracted from the SEVIRI Level 1.5 metadata at each time step since they change over time. EUMETSAT has changed its radiance definition from spectral to effective radiance in 2008 (*EUMETSAT*, 2007a), which affected all Level 1.5 data of the infrared channels after that date (see Section 3.4). Data with the old radiance definition has been re-processed by EUMETSAT and can be re-ordered. For the visible and near-infrared channels no change of the radiance definition took place.

### 3.4 Calculating Brightness Temperatures

ToA brightness temperatures can be calculated from spectral radiances by inverting the Planck function at the center wavelength  $\lambda_0$  ( $\mu\text{m}$ ) of the respective MSG SEVIRI channel (*Schmetz et al.*, 2002). MSG SEVIRI data are provided as effective radiances over the integrated bandwidth of each channel. An error of  $< 1$  K is expected when calculating brightness temperatures with the spectral Planck function and with effective radiances (*EUMETSAT*, 2008). Effective radiances can no longer be related to brightness temperatures by use of an analytic function. Either look-up tables which relate effective radiances to brightness temperatures or parametric models can be used instead. We use a parametric expression with linear regression coefficients to convert the observed effective radiances to equivalent brightness temperatures (*EUMETSAT*, 2012b):

$$T_x = \left( \frac{c_2 \nu_x}{\ln[1 + c_1 \nu_x^3 / R_x]} - \beta_x \right) / \alpha_x, \text{ where } \nu_x = \frac{10^4}{\lambda_x}, \quad (6)$$

and where  $x = 3.9, 6.2, 7.3, 8.7, 9.6, 10.8, 12.0, 13.4 \mu\text{m}$  is one of the MSG SEVIRI Infrared channels,  $c_1 = 2hc^2$  ( $\text{mW m}^{-2} \text{sr}^{-1} (\text{cm}^{-1})^{-4}$ ),  $c_2 = hc/\kappa$  (K cm),  $c$  is the speed of light,  $\kappa$  is the Boltzmann constant,  $h$  is the Planck's constant and  $R$  is the channel integrated blackbody radiance ( $\text{mW m}^{-2} \text{sr}^{-1} (\text{cm}^{-1})^{-1}$ ). The regression coefficients  $\nu$  (the channel's wavenumber ( $\text{cm}^{-1}$ ) which is not the published wavenumber of the central wavelength),  $\alpha_x$  (-) and  $\beta_x$  (K) have to be defined by sensor (*EUMETSAT*, 2012b). The estimated absolute error of the linear regression compared to the numerical (spectral integration) solution is in the order of 0.01 K.

### 3.5 Calculating Reflectances

ToA reflectances are calculated by dividing the ToA radiance with the total solar irradiance (TSI)  $R_s$  ( $\text{W m}^{-2}$ ) for a given band with central wavelength  $\lambda_x$  ( $\mu\text{m}$ ) and bandwidth  $w_x$  ( $\mu\text{m}$ ), normalized by the cosine of the sun zenith angle  $\theta_s$  (note that all angles in this document are given in degrees. They have to be converted to radians in trigonometric functions unless otherwise noted) and the astronomical sun-earth distance  $d_s$  (AU):

$$\rho_x = \frac{R_x \pi d_s^2}{R_s \cos(\theta_s)}, \quad (7)$$

where  $x$  are the 0.6, 0.8, 1.6  $\mu\text{m}$  or HRV MSG SEVIRI visible or near-infrared channels. Radiance is converted from units  $\text{mW m}^{-2} \text{sr}^{-1} (\text{cm}^{-1})^{-1}$  to  $\text{W m}^{-2} \text{sr}^{-1} (\text{um}^{-1})^{-1}$  by multiplying with  $10w_x/\text{lambda}_x^2$  to generate a band-integrated radiance  $R_x$ .  $R_s$  could be derived from spectral TSI by use of a radiative transfer model. It is also provided by *EUMETSAT* (2012a) for MSG SEVIRI solar channels.

The 3.9  $\mu\text{m}$  channel includes both a reflective solar and a thermal component. The channel can thus only be used as a pure thermal channel during night time. During daytime, the two components have to be separated for deriving the channel's reflectance. As a simple approximation the channel's blackbody temperature inferred from the 12.0  $\mu\text{m}$  channel is subtracted from both the channel's radiance  $R_{3.9}$  and the solar radiance  $R_s$  at the channel's wavelength:



$$\rho_{3.9} = \frac{R_{3.9} - B(\lambda_{3.9}, T_{12.0})}{R_s \cos(\theta_s) - B(\lambda_{3.9}, T_{12.0})}, \quad (8)$$

where  $B(\lambda_{3.9}, T_{12.0})$  is Planck's law applied to the 12.0  $\mu\text{m}$  brightness temperature at the center wavelength of the 3.9  $\mu\text{m}$  channel. This relation is only valid for solar zenith angles smaller than  $\theta_s^{\text{max}}$ . The threshold depends on the intensity of the thermal component. The 3.9  $\mu\text{m}$  channel separation into solar and thermal radiance components works better for cold surfaces:

$$\theta_s^{\text{max}} = \arccos \left[ \frac{B(\lambda_{3.9}, T_{12.0} + 10)}{R_s} \right], \quad (9)$$

which was modified after *Khlopenkov and Trishchenko (2007)* by adding a further safety constant of 10 K on top of the 12.0  $\mu\text{m}$  brightness temperature.

### 3.6 Combining Narrow-Band Channels

The Heliosat cloud index has a substantial sensitivity on the spectral characteristics of the surface underlying the clouds. Heliosat has been shown to work best with a broad band visible channel (*Posselt et al., 2011*). "HelioMont" thus relies on the availability of a broad band visible channel. The MSG SEVIRI HRV channel is not available on the full disk, so it has to be simulated by use of the linear combination of reflectances on the full Meteosat disk (*Deneke and Roebeling, 2010*):

$$\rho_{\text{HRV}} = 0.667\rho_{0.6} + 0.368\rho_{0.8} \quad (10)$$

The two narrow band channels do not cover the full spectral bandwidth of the HRV channel. Nevertheless, the above linear approximation explains at least > 95% of the HRV variance on the full Meteosat disk. The linear approximation is a valid approach for cloudy reflectances. A more complex approach for narrow-to-broadband conversion, such as using a combined atmosphere and canopy radiative transfer model or a scene-dependent formulation, would be required to represent the diverse spectral footprints of the underlying land and ocean surface.

### 3.7 Regridding Infrared Channels

If the MSG SEVIRI HRV channel is used in combination with the regular SEVIRI VIS, NIR or IR channels, the latter need to be re-gridded to the spatial resolution of the HRV channel. Bilinear interpolation is employed by taking into account the shifted HRV detector location relative to the regular VIS, NIR and IR detectors of the SEVIRI sensor. Interpolation locations  $x_{\text{int}}$  and  $y_{\text{int}}$  are calculated as follows:

$$x_{\text{int}} = (\text{col}_{\text{max}}^{\text{HRV}} - \text{col}_{\text{min}}^{\text{HRV}})/3 - \Delta x/3 + \lfloor \Delta x/3 \rfloor - (\text{col}_{\text{min}}^{\text{HRV}} + \Delta x_{\text{int}})/3 + \text{col}_{\text{min}}^{\text{VIS,IR}} \quad (11)$$

$$y_{\text{int}} = (\text{lin}^{\text{HRV}} - \text{lin}_{\text{min}}^{\text{HRV}})/3 - \Delta y/3 + \lfloor \Delta y/3 \rfloor + (\text{lin}_{\text{min}}^{\text{HRV}} + \Delta y_{\text{int}})/3 - \text{lin}_{\text{min}}^{\text{VIS,IR}}. \quad (12)$$

Note the reversed column interpolation index calculation in comparison to the line calculation due to the east-west reversing of the channel data performed within this processing. The [...] brackets

denote integer (floor) division. Navigation shifts  $\Delta x$  and  $\Delta y$  are calculated in Section 4.  $\Delta x_{\text{int}} = 2$  and  $\Delta y_{\text{int}} = 2$  correspond to the inter-channel registration shift. While this shift should be fixed to the sensor's detector array configuration, we have found it to vary in the L1.5 data, most likely due to the image rectification and registration process carried out by EUMETSAT. The shift is thus estimated for each 12 UTC slot by regressing the HRV channel with the simulated HRV channel using shift intervals of  $-2 \leq \Delta x_{\text{int}} \leq 2$  and  $-2 \leq \Delta y_{\text{int}} \leq 2$ .

### 3.8 Calculating Scan Time

The MSG SEVIRI sensor has a 15' scan cycle. 12.5 minutes are used to perform the actual scan by successively moving the scan mirror from south to north. The knowledge of the pixel's scan time relative to the initial time of the full disk scan cycle is necessary for co-locating local-scale satellite-derived variables with ground-based measurements. Ground-based measurement are either time integrated or instantaneous. If for instance an instantaneous ground measurement in Switzerland with a 10 minute interval is compared to MSG SEVIRI data, then the 12:00 UTC SEVIRI slot does not correspond to the 12:00 UTC ground measurement. It corresponds best to the 12:10 UTC ground measurement, since Switzerland is covered at the end of the scan cycle, at around 12:11 UTC.

The scan time (minutes) is calculated for each MSG SEVIRI scan line (and not per pixel, since one scan line is completed in less than a second):

$$\Delta t(\text{lin}) = \frac{\text{lin} + (\text{lin}_{\text{sev}} - \text{lin}_{\text{tot}})/2 - 1}{\text{lin}_{\text{sev}}} \cdot t_{\text{full}}, \quad (13)$$

where  $t_{\text{full}} = \text{lin}_{\text{sev}} / (3 \cdot 100)$  is the full disk scan time in minutes, since 3 VIS,IR lines are scanned per MSG revolution and the MSG satellite is rotating with 100 rotations per minute. The sensor has more lines than reported in the Level 1.5 image data:  $\text{lin}_{\text{sev}} = 3750$  (11250 for HRV), where  $\text{lin}_{\text{tot}} = 3712$  (11136 for HRV).

The above calculation assumes that the full disk is scanned. These assumptions do not apply for the MSG rapid scan service, where the above formula would need to be adjusted.

## 4 Navigation

The MSG SEVIRI image rectification and navigation accuracy is generally within the specified accuracy of 3.0 km at the sub-satellite-point (SSP) as documented in *EUMETSAT (2007b)*. This accuracy requirement is not met during periods of satellite manoeuvres. The accuracy requirement is further not sufficient for the HRV channel which has a spatial footprint of 1.1 km at the SSP. An automatic navigation routine is developed to correctly navigate the HRV channel and to account for short-term shifts introduced by manoeuvres and failed navigation attempts by EUMETSAT.

The navigation is based on a coastline matching algorithm using a SEVIRI solar channel (HRV, 0.6 or 0.8  $\mu\text{m}$ ). The navigation procedure is thus restricted to daytime operation and it assumes that the mis-alignment is linear in both north/south and west/east direction. Since the navigation shifts the domain until it best matches the underlying coastline features, the navigation requires to read a larger area than the selected geographical domain. Manually observed navigation errors are in the order of 2-3 HRV pixels under regular conditions and 5-10 HRV pixels in the extreme case (i.e. during manoeuvres). The domain is extended by 15 HRV pixels or 5 VIS, NIR and IR pixels in the east-west and north-south direction. The visible channel selected for navigation is read with this larger domain at the beginning of each time step. After the navigation has been performed, the calculated eastward and northward navigation shifts are applied to all channels.

Navigation is only performed for  $\theta_s < 70^\circ$ . Edge detection becomes difficult at high sun angles due to the atmospheric path length and due to surface BRDF effects. The coastline edges are extracted by calculating the 1-pixel spatial variance on the water mask (Section 9.1):

$$w_{\text{edge}} = \sigma_{xy}(\text{watermask}), \quad (14)$$

where only water bodies with an area of  $> 50\text{km}^2$  are included. Edge sharpness is increased by setting  $w_{\text{edge}} = 0$  for  $w_{\text{edge}} \leq 0.01$ . For each time step the coastline edges of the clear sky visible channel are evaluated. Since the navigation has to occur prior to cloud screening, this simple method is implemented to extract clear sky pixels  $\rho_{\text{cf}}$  needed for the edge detection in the actual satellite data:

- $\rho$  has to be smaller than  $\rho_{\text{thres}}$
- $\rho_{\text{thres}}$  is either the mean of all snow-free and cloud-free pixels over land plus 0.1 (cloud and snow mask of previous day, see Section 6.3 ) or 0.3 if the cloud and snow masks are not available
- a safe boundary of 3 pixels is added around all “cloudy” pixels.

Edges of water surfaces are then calculated from clear sky pixels  $\rho_{cf}$ :

$$\rho_{edge} = \sigma_{xy}(\rho_{cf}), \quad (15)$$

$\rho_{edge}$  is now shifted by  $i = -15 \dots 15$  pixels in the north/south and  $j = -15 \dots 15$  in the west/east directions ( $\pm 5$  pixels for non-HRV channels) in relation to  $w_{edge}$ . For each shift the two fields are multiplied to a “navigation score”:

$$E_{i,j} = \sum_n \min(\rho_{edge}, 0.0022) \cdot w_{edge} / n_E, \quad (16)$$

where  $n_E$  is the sum of all pixels where  $\rho_{edge}$  and  $w_{edge}$  are valid and where  $w_{edge} > 0$ . The best navigation shift  $\Delta x = i$  and  $\Delta y = j$  is estimated by maximizing  $E$ . A successful navigation requires  $\Delta x$  and  $\Delta y$  not to be pegged to their bounds ( $\pm 15$  or  $\pm 5$  pixels) and at least 50% of the coastline edge pixels to be visible. These requirements are not always fulfilled during daytime. A median of the 50 last successful navigation results is thus used for navigating instantaneous MSG SEVIRI data, except when 70% or more coastline edge pixels are visible. In the latter case the instantaneous navigation result can be safely applied. The instantaneous navigation results are also used during manoeuvres (a median filter would not be able to follow rapid geographical shifts observed during manoeuvres).

## 5 Cloud Masking

The Separation of Pixels using an Aggregated Rating over Canada (SPARC) cloud mask algorithm (Khlopenkov and Trishchenko, 2007) is used. It has originally been developed to provide a cloud, cloud shadow and snow detection for the 5 channels of the polar orbiting Advanced Very High Resolution (AVHRR) sensor from the National Oceanic and Atmospheric Administration (NOAA). It is also suitable for the Meteosat Second Generation SEVIRI and Meteosat First Generation MVIRI sensor data (Fontana, 2010). SPARC uses an additive and continuous rating which allows to calculate the cloud mask even with a partial availability of the spectral cloud mask tests (Figure 2). In comparison, most cloud masks use a classification tree in which every test depends on the successful execution of previous (upstream) tests. They thus are not applicable across satellite sensors and satellite sensor generations with differing spectral coverage. Substantial changes were made to the original SPARC algorithm with respect to the detection of snow and for several of the spectral tests for cloud detection. The full cloud mask algorithm is documented here for completeness. The reader is motivated to consult Khlopenkov and Trishchenko (2007) for the original algorithm and Fontana (2010) for the adaptation from AVHRR to Meteosat.

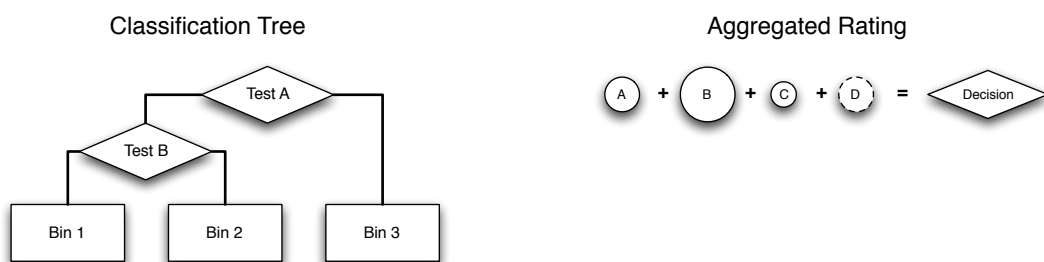


**Figure 2:** The classification tree (left) versus the aggregated rating (right) cloud masking method.

The SPARC algorithm produces an aggregated rating  $F$  from the sum of individual scores  $A$ ,  $B$ ,  $C$ ,  $D$  etc.,

$$F = A + B + C + (D) + \dots \quad (17)$$

where each score generates a continuous measure of cloudiness. It becomes negative for a clear sky and positive for a cloudy scene. The magnitude of the respective score is then a measure of cloud probability. For instance, a score of 0 often occurs in situations of partial cloudiness or at cloud boundaries, and a score of 50 gives a high probability of rather thick clouds. Scores are also allowed to be contradicting. Summing score  $A$  of -10 and score  $B$  of 10 will yield an aggregated score  $F=0$  and thus result in an undecided cloud mask with low confidence for either cloudy or clear sky. A decision

**Table 1:** Offset and scale factors for each of the SPARC scores. These factors are valid for the SEVIRI sensor and might need to be adjusted for other sensors. Most match the original AVHRR-based factors.

No.	score	offset	units	scale	units
1	$T_{\text{score}}$	-5.0	K	-0.4	$\text{K}^{-1}$
2a	$B_{\text{score}}^{0.6}$	0.3	-	67	-
2b	$B_{\text{score}}^{0.8}$	0.24	-	75	-
2c	$B_{\text{score}}^{\text{HRV}}$	0.3	-	60	-
3a	$R_{\text{score}}^{1.6}$	0.025	-	400	-
3b	$R_{\text{score}}^{3.9}$	0.06	-	33 / 110	-
4	$N_{\text{score}}$	0.1	-	-30	-
5	$UR_{\text{score}}$	0.034	-	1200	-
6	$UT_{\text{score}}$	3.5	$\text{K}^2$	1.33	$\text{K}^{-2}$
7	$C_{\text{score}}$	1.5	K	4.0	$\text{K}^{-1}$
8	$TT_{\text{score}}$	5.0	K	0.5	$\text{K}^{-1}$
9	$DT_{\text{score}}$	0.0	K	1.0	$\text{K}^{-1}$
10	$S_{\text{score}}$	0.4	-	40	-
11	$F_{\text{score}}$	-5.0	K	1.0	$\text{K}^{-1}$

tree misses such functionality. It also cannot cope with missing scores. In SPARC the aggregated rating F can still be calculated when for instance score D (in brackets) is missing.

Similar to many other cloud masks the SPARC method is very empirical. Each score needs to be weighted with at least two coefficients per score. These coefficients are given in Table 1.

## 5.1 Temperature Score

The temperature score  $T_{\text{score}}$  tests the brightness temperature of the  $10.8 \mu\text{m}$  thermal channel against the surface skin temperature (SKT).

$$T_{\text{score}} = (T_{10.8} - T_{\text{cf}} - T_{\text{offset}})T_{\text{scale}} \quad (18)$$

The key requirement for this score is to estimate a realistic clear sky (cloud free) brightness temperature  $T_{\text{cf}}$ . *Khlopenkov and Trishchenko (2007)* use a reanalysis-based skin temperature. This was not found to be a suitable option for regions with complex terrain. In comparison to polar orbiting sensors, geostationary satellite sensors capture the diurnal cycle of brightness temperature which is a good constraint for the  $T_{\text{cf}}$  retrieval: for each day a diurnal temperature model is fitted on previously cloud masked  $T_{10.8}$  data in order to estimate the diurnal cycle of  $T_{\text{cf}}$  (Section 6.2).

## 5.2 Brightness Score

The brightness-score  $B_{\text{score}}$  operates during daytime and it tests the reflectance of the visible channel  $\rho$  against a background reflectance  $\rho_{\text{cf}}$ . The narrow-band 0.6 and 0.8  $\mu\text{m}$  channels are used over land and water, respectively. If available, the broadband visible channel (HRV on MSG) can be used independently from surface type.

$$B_{\text{score}} = (\rho - B_{\text{offset}})B_{\text{scale}} \quad (19)$$

By default  $B_{\text{offset}}$  and  $B_{\text{scale}}$  are taken from Table 1. The score is more effective if the actual cloud free background reflectance  $\rho_{\text{cf}}$  is used for  $B_{\text{offset}}$ . In this case  $B_{\text{offset}}$  is replaced by  $\rho_{\text{cf}} + 0.05$ , where  $\rho_{\text{cf}}$  is a clear sky composite for the given time of day (details given in Section 6.1 ) and 0.05 is the new threshold by which cloudy and non-cloudy scenes are identified.

## 5.3 Reflectance Score

The reflectance score  $R_{\text{score}}$  tests the reflectance properties of different surface types to those of clouds in the visible solar (0.6  $\mu\text{m}$ ) and near infrared (1.6  $\mu\text{m}$ ) or middle-wave infrared (3.9  $\mu\text{m}$ ) spectrum. Two types of reflectance tests have to be formulated, because depending on the AVHRR sensor generation, either the 1.6  $\mu\text{m}$  or the 3.9  $\mu\text{m}$  is available. For MSG the reflectance test is always carried out with the 0.6  $\mu\text{m}$  and 1.6  $\mu\text{m}$  channels. It was modified from the original formulation of *Khlopenkov and Trishchenko* (2007) since the latter falsely identified clear sky low latitude deserts as clouds. The published formula including its scale and offset coefficients had to be modified:

$$R_{\text{score}}^{1.6} = \left[ \frac{\rho_{0.6}^2 \rho_{1.6}^2}{1.5 \rho_{1.6}^{2.8} (3.0 \rho_{1.6} + 0.5 \rho_{0.6} + 3.5) + 1.5 \rho_{0.6}^{2.0}} - R_{\text{offset}}^{1.6} \right] R_{\text{scale}}^{1.6} \quad (20)$$

For completeness, the 3.9  $\mu\text{m}$  reflectance score is also given:

$$R_{\text{score}}^{3.9} = (\rho_{3.9} - R_{\text{offset}}^{3.9})R_{\text{scale}}^{3.9}, \quad (21)$$

where  $\rho_{3.9}$  is the reflective component of the 3.9  $\mu\text{m}$  channel, extracted from the combined solar and thermal radiance contributions of this channel (Section 3.5). The first  $R_{\text{scale}}^{3.9}$  entry in Table 1 is applied when  $\rho_{3.9}$  is smaller than  $R_{\text{offset}}^{3.9}$ . The second one is applied when  $\rho_{3.9}$  is equal or larger than  $R_{\text{offset}}^{3.9}$ .

## 5.4 Simple Ratio Score

The simple ratio score  $N_{\text{score}}$  is related to the NDVI and identifies clouds as having a similar signature in the visible and near-infrared spectrum. However, the same applies to bright non-vegetated surfaces. Thus this score is limited to values in the range  $\pm 3$  and should help in the decision of cloud detection when other scores cannot clearly separate cloud-free from cloudy cases:

$$N_{\text{score}} = \left( \left| \frac{\rho_{0.8}}{\rho_{0.6}} - 1 \right| - N_{\text{offset}} \right) N_{\text{scale}} \quad (22)$$

## 5.5 Spatial Texture Uniformity Score

The spatial texture uniformity score  $UR_{\text{score}}$  compensates for the weaknesses of the main scores to detect cloud boundaries. It is calculated by testing the spatial variance  $\sigma_{xy}$  (for details see Section 14.2) of the visible reflectance for each pixel in a surrounding region of  $\pm 2$  pixels. This score is misleading when the background cloud free scene includes a high spatial variance. This might apply in regions with complex terrain and at land-water boundaries. The score is thus limited to a range of  $\pm 4$ , and it is damped with a static map of the spatial variance of the background which is based on the water mask (Section 9.1):

$$UR_{\text{score}} = f_w(\sigma_{xy}(\rho_{\text{vis}}) - UR_{\text{offset}})UR_{\text{scale}}, \quad (23)$$

where  $\rho_{\text{vis}}$  can either be the broad band visible (HRV) or the 0.8  $\mu\text{m}$  channel of MSG, and  $f_w$  is calculated by

$$f_w = 1 - \min(5\sigma_{xy}(\text{watermask}), 1), \quad (24)$$

and by using a spatial variance of  $\pm 2$  pixels.

## 5.6 Spatial Temperature Uniformity Score

Along the same lines the spatial temperature uniformity score  $UT_{\text{score}}$  is calculated:

$$UT_{\text{score}} = (\sigma_{xy}(T_{10.8}) - UT_{\text{offset}})UT_{\text{scale}}. \quad (25)$$

It is limited to the range of  $\pm 4$ . Unlike for the spatial texture uniformity score the variance of the background clear sky radiative temperature field is not taken into account.

## 5.7 Cirrus Score

The cirrus score  $C_{\text{score}}$  is suitable to detect thin and high clouds which only leave a weak trace in the main temperature or brightness score:

$$C_{\text{score}} = (T_{10.8} - T_{12.0} - C_{\text{offset}})C_{\text{scale}} \quad (26)$$

The  $C_{\text{score}}$  is limited to positive values since optically thick clouds may also produce negative values while high ice clouds in general have higher emissivities in the 10.8 compared to the 12.0  $\mu\text{m}$  region.



## 5.8 Temporal Temperature Uniformity Score

Compared to the original SPARC formulation two new temporal scores were added since the analysis of time-varying fields is firstly possible with geostationary satellites, and the temporal variation of brightness temperature is very effective for cloud detection. In analogy to the spatial temperature uniformity a temporal temperature uniformity score  $TT_{\text{score}}$  is created:

$$TT_{\text{score}} = (\sigma_t^{2h}(T_{10.8}) - TT_{\text{offset}})TT_{\text{scale}}, \quad (27)$$

where  $\sigma_t^{2h}(T_{10.8})$  is the temporal variance for each pixel over the last 2 hours. Ideally a time centered temporal variance of  $\pm 1$  hour would be chosen. Details on the calculation of the temporal variance are given in Section 14.1 ). The score is limited to values of  $\pm 4$ . A high temporal variability of the 10.8  $\mu\text{m}$  brightness temperature indicates variable cloud conditions. This score thus helps in the generation of a cloud-conservative cloud mask where the start and the end of cloud occurrence can be detected with more precision.

## 5.9 Diurnal Temperature Uniformity Score

The diurnal temperature uniformity score  $DT_{\text{score}}$  has a different purpose. It helps the detection of low-level stratiform clouds. Since they often occur during synoptic weather situations with a strong inversion of the planetary boundary layer they can have a cloud top temperature which is similar to the underlying surface temperature. With a non-existent or even reversed temperature difference low level stratiform clouds cannot be detected by the main temperature score. These clouds may also have a brightness similar to the underlying surface in the case of snow covering the surface. The new diurnal temperature uniformity score identifies permanent and low-level cloud decks by exploiting their weak diurnal cycle in the 10.8  $\mu\text{m}$  brightness temperature.

$$DT_{\text{score}} = ((5 - \sigma_t^{24h}(T_{10.8}))^2 - DT_{\text{offset}})DT_{\text{scale}}, \quad (28)$$

The score is limited to the positive value range from 0 . . . 20 since it is only effective to detect cloudy but not clear sky cases. The score is only calculated for  $\sigma_t^{24h}(T_{10.8}) < 5$ . It is effective in detecting 24h+ lasting cloud decks, such as occurring during planetary boundary layer inversions in winter time over the Swiss lowland or for coastal regions with upwelling cold water (such as the western coasts of Africa or South and North America).

## 5.10 NDSI Score

The Normalized Difference Snow Index (NDSI) is a well established empirical snow detection method. It was not part of the original SPARC since the 1.6  $\mu\text{m}$  channel is not available on all AVHRR sensors. It is however included here since MSG SEVIRI contains the 1.6  $\mu\text{m}$  channel:

$$S_{\text{score}} = \left( \frac{\rho_{0.6} - \rho_{1.6}}{\rho_{0.6} + \rho_{1.6}} - S_{\text{offset}} \right) S_{\text{scale}}. \quad (29)$$

## 5.11 Freeze Score

In addition to the NDSI score, snow detection is facilitated by the use of the freeze score:

$$F_{\text{score}} = (-|T_{10.8} - T_f + 2| - F_{\text{offset}})F_{\text{scale}}, \quad (30)$$

where  $T_f$  (K) is the seasonally oscillating maximum radiative surface temperature for snow cover:

$$T_f = 273.16 + 2 \sin\left(\frac{2D\pi}{365.25} - \frac{\pi}{10}\right), \quad (31)$$

and where  $D$  is the day of year (1 . . . 366).

## 5.12 Snow Detection

A new snow detection has been implemented which uses the NDSI score and the snow cover information of previous time steps. In analogy to the aggregated cloud rating an aggregated snow rating  $\text{snow}_{\text{score}}$  is created by summing up four individual scores:

$$\text{snow}_{\text{score}} = (3 - T_{\text{score}}) + (3 - R_{\text{score}}) + S_{\text{score}} + F_{\text{score}}, \quad (32)$$

The snow mask and a continuous snow cover factor (surrogate for snow cover probability) is then diagnosed for  $\theta_s < 80^\circ$  and if at least two snow scores are present:

$$\text{snow}_{\text{mask}} = \begin{cases} 0 & \text{if } \text{snow}_{\text{score}} \leq 0; \\ 1 & \text{if } \text{snow}_{\text{score}} > 0. \end{cases} \quad (33)$$

$$f_{\text{snow}} = 1 - \frac{\text{snow}_{\text{score}} - f_{\text{snow}}^{\min}}{f_{\text{snow}}^{\max} - f_{\text{snow}}^{\min}}, \quad (34)$$

with  $f_{\text{snow}}^{\min} = -15$ ,  $f_{\text{snow}}^{\max} = 10$  and  $f_{\text{snow}}$  ranging between 0 (fully snow covered) and 1 (snow free).

The reversing of  $f_{\text{snow}}$  is explained in the next section. The following constraints are set to the snow mask and the snow factor:

- $f_{\text{snow}}$  is set to 0 for  $\theta_s \geq 80^\circ$  if the daily composited snow mask of the previous day (see Section 6.3) has a value of 1;
- the snow mask is set to 0 and the snow factor to 1 if  $T_{10.8} > T_f + 10$ , thus removing pixels with too high brightness temperature;
- the snow mask is set to 0 and the snow factor to 1 if  $\rho < 0.25$ , thus removing pixels with too low reflectance values.
- the snow mask is set to missing when the cloud mask (see below) detects clouds since it is not possible to detect snow through clouds with this simple empirical algorithm.

The SPARC algorithm specifies a cloud mask over snow surfaces. This mask is however not used here since the continuous snow factor is applied for cloud screening those areas.

### 5.13 Cloud Detection

In areas of sun glint the brightness score becomes ineffective. A sun glint damping factor is thus calculated:

$$f_{\text{glint}} = (0.95 - b)^2, \text{ where} \quad (35)$$

$$b = (300 - 180\theta_s)(1 - \cos \delta_f)^2, 0 \leq b \leq 0.95, \text{ and} \quad (36)$$

$$(37)$$

All angles are in radians and  $\delta_f$  is the forward scattering angle as defined in Section 10.4. A night mask factor is calculated:

$$f_{\text{night}} = (\theta_s^{\text{lim}} - \theta_s)/3, 0 \leq f_{\text{night}} \leq 1, \quad (38)$$

and  $\theta_s^{\text{lim}} = 85^\circ$ . The night factor becomes 0 at night and 1 during daytime, with a smooth transition in between.

With the availability of all scores and factors the aggregated SPARC score can be calculated:

$$\begin{aligned} \text{sparc}_{\text{score}} = & (1 - f_{\text{glint}})f_{\text{snow}}f_{\text{night}}B_{\text{score}} + (1 + f_{\text{glint}})(2 - f_{\text{snow}})(2 - f_{\text{night}})T_{\text{score}} \\ & + (1 - 0.6f_{\text{glint}})(2 - f_{\text{snow}})f_{\text{night}}R_{\text{score}} + (1 - f_{\text{glint}})f_{\text{snow}}f_{\text{night}}N_{\text{score}} \\ & + (1 - f_{\text{glint}})f_{\text{snow}}f_{\text{night}}UR_{\text{score}} + (1 - f_{\text{night}})UT_{\text{score}} + C_{\text{score}} \\ & + (1 - f_{\text{night}})TT_{\text{score}} + (1 - f_{\text{night}})DT_{\text{score}}. \end{aligned} \quad (39)$$

The  $\text{sparc}_{\text{score}}$  is only calculated if at least one specific score, the  $T_{\text{score}}$ , is present. This constraint allows the spin-up of the cloud mask with the self-consistent clear sky compositing (Section 6) by using a sensor with only a single thermal channel. This is needed to generate the initial cloud mask for e.g. the MVIRI sensor when no a-priori clear sky reflectance or brightness temperature composite is available or to run the cloud mask during night-only periods when reflectance-based cloud masking is not applicable. From the continuous SPARC score both a discrete cloud mask and an ad-hoc cloud mask classification uncertainty can be derived:

$$\text{cloud}_{\text{mask}} = \begin{cases} 0 & \text{if } \text{sparc}_{\text{score}} < -4; \\ 1 & \text{if } -4 \leq \text{sparc}_{\text{score}} < 4; \\ 2 & \text{if } \text{sparc}_{\text{score}} > 4 \end{cases} \quad (40)$$

$$\text{cloud}_{\text{mask}}^\sigma = \exp\left(-\frac{(\text{sparc}_{\text{score}} - 0.0)^2}{2 \cdot 10^2}\right). \quad (41)$$

The  $\text{cloud}_{\text{mask}}$  is comparable to classical satellite-based cloud masks generated by hierarchical decision tree algorithms (e.g. NWP SAF, CLAVR, APOLLO, MODIS). It can be used to separate cloudy from cloud-free pixels in a scene. The  $\text{cloud}_{\text{mask}}^\sigma$  is large for a  $\text{sparc}_{\text{score}}$  around 0 (undecided: scene can either be cloudy or clear sky) and exponentially decreases towards situations when full

cloud cover or full clear sky is observed. This is a useful quantity for prescribing the uncertainty of each clear sky or cloudy pixel when they are employed in a statistical fitting procedure for the generation of downstream products (e.g. cloud optical thickness, surface albedo or the diurnal cycle of clear sky land surface temperature). The uncertainty is generally high at cloud boundaries, during night or for sensors with less available channels and scores.

## 5.14 Update of Clear Sky Fields

The cloud mask is part of a larger set of clear sky compositing routines which continuously generates its own background fields (Figure 3). At each time step cloud free pixels ( $\text{cloud}_{\text{mask}} = 0$ ) of visible and infrared channels are extracted from the all sky fields. New cloud free pixels of the visible reflectance  $\rho$  (HRV, 0.6 or 0.8  $\mu\text{m}$ , depending on the visible channel chosen for the Heliosat cloud index calculation), infrared brightness temperature  $T_{10.8}$ ,  $\text{snow}_{\text{mask}}$ , and  $\text{cloud}_{\text{mask}}^{\sigma}$  are stored by slot number for the diurnal clear sky compositing (Section 6). For each Meteosat slot, a history of cloud free pixels is thus available. This history includes the pixel's age  $\text{time}_{\text{mask}}$  (i.e. how many days back in time the clear sky state was observed).

At the start of processing, the clear sky state consists of missing values only. With each successful clear sky retrieval the respective entries in the visible, infrared, snow mask and cloud mask uncertainty states are filled with respective clear sky values which are in turn used to determine the new diurnal clear sky composite as a cloud free reference for upcoming cloud masking and surface radiation calculations.

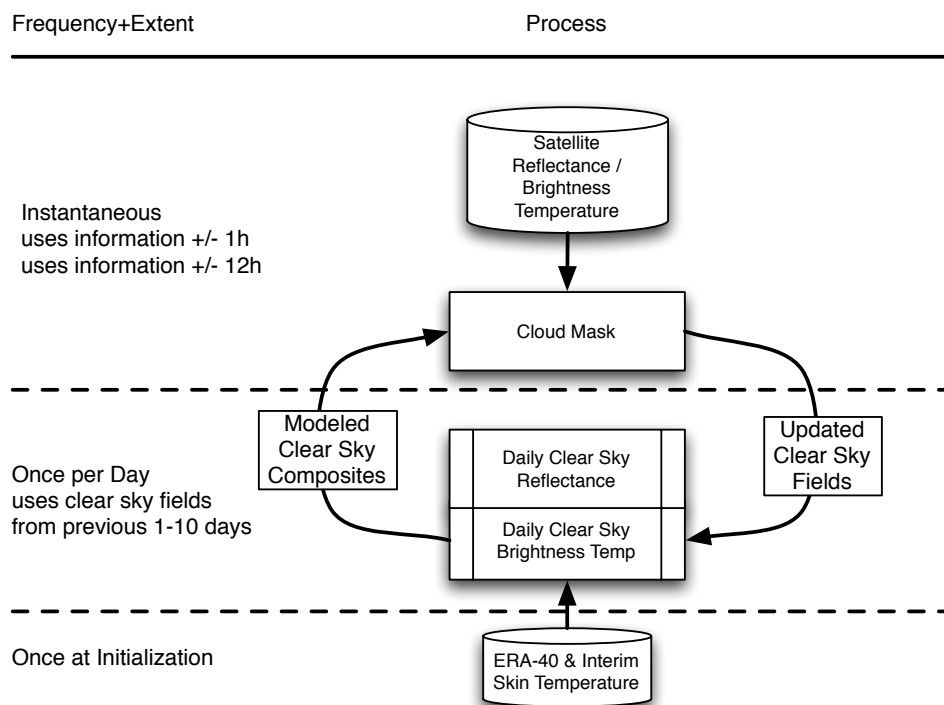


**Figure 3:** The cloud mask is used to separate clear sky from cloudy pixels. The clear sky visible reflectances and infrared brightness temperature fields including their uncertainty are successively used to model the diurnal course of clear sky reflectance and brightness temperature. These composited clear sky diurnal cycles in turn serve as the background fields for the next day's cloud masking. This method requires external model forcing only for spin-up and becomes self-consistent afterwards.

## 6 Clear Sky Compositing

Clear sky compositing for visible reflectances, infrared brightness temperatures and the snow mask is performed once per day at 00:00 UTC when the cloud free states have been updated with current day's values. The clear sky compositing of reflectance and brightness temperature employs parametrized models that are fit on a pixel-by-pixel basis to the daily course of cloud free states. Cloud free states are weighted by use of both the pixel's age  $\text{time}_{\text{mask}}$  (days) and its cloud mask uncertainty  $\text{cloud}_{\text{mask}}^{\sigma}$  (-) for each cloud free state:

$$w = [\text{cloud}_{\text{mask}}^{\sigma} + \max(\text{time}_{\text{mask}}, 1)/\text{time}_{\text{max}}]^{-1}, \quad (42)$$

where  $\text{time}_{\text{max}} = 10$  (days) is the maximum allowed age for a clear sky state. Older states are discarded. Thus, the more recent a clear sky state or the higher its probability of being fully clear sky, the higher the weight it receives during the diurnal reflectance and brightness temperature fitting process.

### 6.1 Reflectance

The clear sky reflectance  $\rho_{\text{cf}}$  is needed as a reference by the cloud mask in order to calculate the brightness score (Section 5). It is also needed by Heliosat in order to calculate the cloud index (Section 8.2). Most known Heliosat algorithms (*Müller et al., 2009; Dürr and Zelenka, 2009; Posselt et al., 2012*) employ a slot-by-slot compositing of clear sky reflectance. They for instance aggregate the slot-wise clear sky fields over a full month. This method may introduce temporal inconsistency since valuable information on the continuous diurnal course of clear sky reflectance is discarded. A monthly composite can also be problematic during times of rapid changes in surface reflectance (green-up, snow fall, snow melt).

In "HelioMont" the diurnal course of the clear sky reflectance  $\rho_{\text{cf}}$  is calculated by fitting a parameterized curve through all valid clear sky retrievals covering a full day. Such a statistical method connects the large number of diurnal clear sky measurements and maximizes the usage of available information. In turn, the maximum required compositing period decreases to a few days. The model is built on the Modified Lambert-Beer equations (*Müller et al., 2004*) for atmospheric scattering, the back-scattering properties of land surfaces (*Zelenka et al., 1999*) and the terrain-dependent illumination conditions (*Tan et al., 2010*):

$$\rho_{\text{cf}} = (A + B)I \cdot S, \quad (43)$$

where  $A$  is the contribution of atmospheric absorption and scattering,  $B$  is the contribution of surface reflectance backscatter,  $I$  is the contribution of illumination in tilted terrain on land pixels and  $S$  is the contribution of sun glint over water pixels to the modeled top-of-atmosphere clear sky reflectance  $\rho_{cf}$ :

$$A = \rho_A (\cos \theta_s)^a \quad (44)$$

$$B = \rho_B \left( \frac{\delta_b^{\max} - \delta_b}{\delta_b^{\max} - \delta_b^{\min}} \right)^2 \quad (45)$$

$$I = \rho_I \frac{\cos \theta_{s-p}}{\cos \theta_s} + 1 \quad (46)$$

$$S = \rho_S \left[ (0.95 - \min(\max(50(\pi/2 - \theta_s)(1 - \cos \delta_f)^2, 0), 0.95)) \phi_{v-s}^{\lim} \right]^2 + 1 \quad (47)$$

where

$$\phi_{v-s}^{\lim} = 1 - (\min(\max(1/20(180 - |\phi_{v-s}|), 0), 1))^3 \quad (48)$$

and where  $\theta_s$  is the sun zenith angle,  $\delta_f$  and  $\delta_b$  is the sun-satellite forward and backward scattering angles (Section 10.4),  $\delta_b^{\min}$  is the minimum sun-satellite backward scattering angle during the day (e.g. at solar noon, and when  $\phi_{v-s} = 0$ ) and  $\theta_{s-p}$  is the angle between the sun direction and normal to the plane (Section 10.3). All angles are per-pixel and are calculated for each time step. The model parameters  $\rho_A$ ,  $\rho_B$ ,  $\rho_I$ ,  $\rho_S$ ,  $a$  and  $\delta_b^{\max}$  are estimated by use of a robust non-linear least square solver (<http://www.physics.wisc.edu/~craigm/idl/fitting.html>) based on MINPACK-1 (<http://www.netlib.org/minpack>). Start values and parameter bounds are found in Table 2. Fitting is performed only if the longest gap in the observed clear sky data over the diurnal cycle is no longer than 7 hours.

**Table 2:** Parameters of the clear sky reflectance model

No.	name	start value	lower bound	upper bound
1	$\rho_A$	0.1	0.01	1
2	$a$	-0.1	-2.5	1
3	$\rho_B$	0.01	0	0.5
4	$\delta_b^{\max}$	70	50	120
5	$\rho_I$	0.01	0	10
6	$\rho_S$	0.01	0	10

Figure 4 demonstrates model estimates (orange) for the observed (blue) diurnal course of clear sky reflectance at four locations (For details see Table 3). The upper left panel shows a location within the lake of Geneva in Switzerland which has simple illumination conditions (flat surface) with minor BRDF backscatter during mid-day. The atmospheric scattering component becomes larger at high solar zenith angles due to the higher air mass. The upper right panel shows a location in the north-eastern part of the Swiss plateau. It includes significant uncertainty in the cloud screened clear sky reflectances during the second part of the day. While a slot-by-slot compositing would have resulted in overestimated clear sky reflectances during that period, the weighted model fit allows a realistic and continuous reconstruction of the diurnal course of clear sky reflectance.

Outliers in  $\rho$  are removed by only considering the 5-95% percentile in clear sky reflectances. The

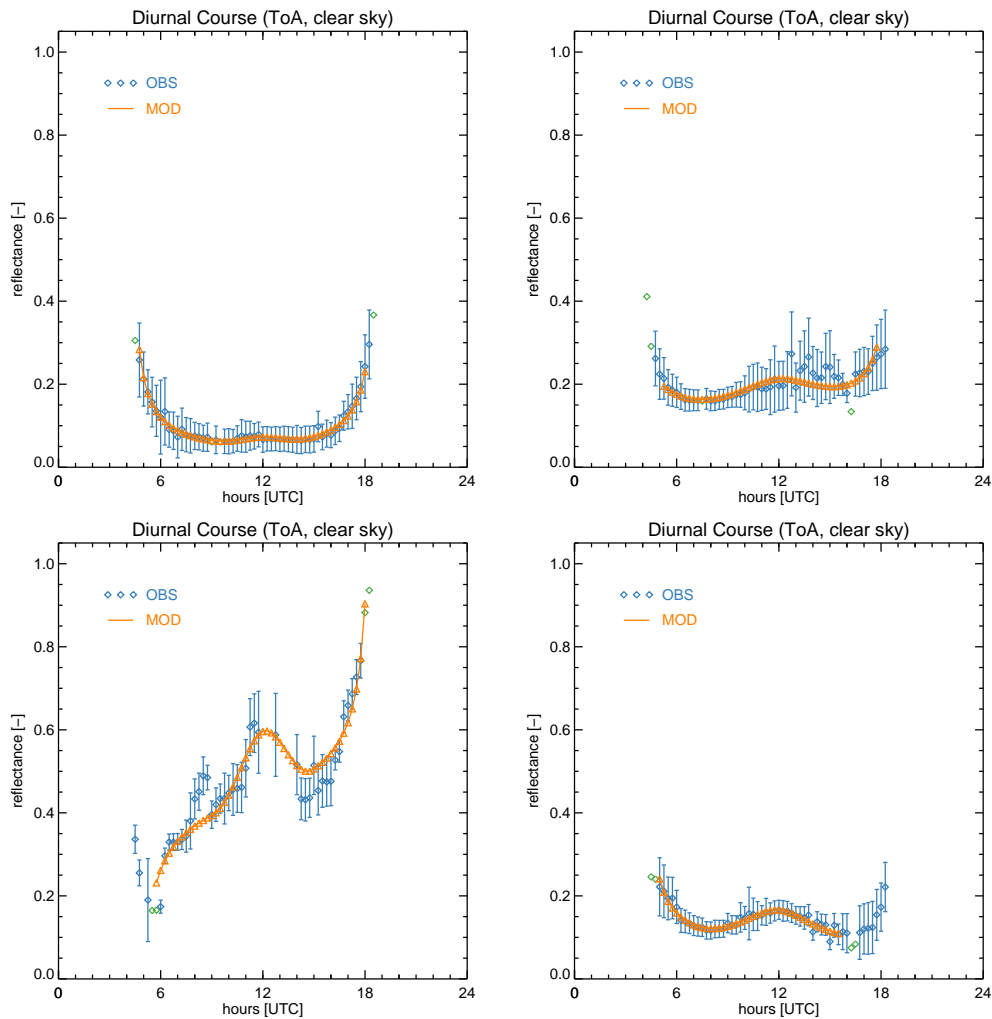


**Figure 4:** Meteosat clear sky reflectance (blue) and corresponding model fits to the cloud masked data of the last 10 days (orange) at four Alpine locations (see Table 3) on 5 August 2008.

removed pixels (shown in green) for instance correspond to cloud shadows or to missed clouds. The lower left panel shows a high elevation region which is permanently snow-covered. It is located in the canton of Wallis in Switzerland on a westerly oriented slope where solar illumination of the surface raises during the day. During mid-day either the snow exhibits a strong backscatter or missed clouds are falsely interpreted as snow. The lower right panel displays an easterly oriented slope in southern Switzerland with intermediate surface backscatter during noon. The surface receives more illumination in the morning and becomes shadowed in late afternoon. Terrain shadows are calculated, but their effect on the clear sky reflectance are not part of the simple model. Thus model estimates are discarded after 16 UTC.

## 6.2 Brightness Temperature

The clear sky brightness temperature  $T_{cf}$  is needed by the cloud mask (Section 5) in order to calculate the temperature score.  $T_{cf}$  can only be derived after the  $T_{10.8}$  channel data have been separated into clear sky and cloudy data. This chicken and egg causality is often found in cloud



**Table 3:** Geographic locations of diurnal clear sky composites displayed in Figures 4, 5 and 6.

Panel	Place	Longitude (° E)	Latitude (° N)	Elevation (m a.s.l.)
upper left	Lake Geneva (near Lausanne)	6.46	46.47	370
upper right	Swiss Lowland (near Wattwil)	9.11	47.31	922
lower left	Alpine (near Saas Fee)	7.88	46.04	3510
lower right	Alpine (Misox valley)	9.19	46.37	2090

masks that generate their own boundary conditions in order to be less dependent on external (often model-based) data sets. The problem is solved here by initializing the system with external constraints and then letting it become self-consistent after spin-up. 6-hourly surface skin temperature forecasts are ingested from the ECMWF ERA Interim (*Berrisford et al., 2009*) or from the ECMWF operational 24h forecast (<http://www.ecmwf.int>) and are used in the initial fitting process for the diurnal course of the clear sky brightness temperature  $T_{cf}$ . Skin temperature  $T_{skt}$  (K) is corrected for the total column water vapor in the satellite's view path:

$$T_{cf} = T_{skt} - 10(1 - \cos(\theta_v)) \cdot H_2O/30, \quad (49)$$

where  $H_2O$  is the total column water vapor ( $\text{kg m}^{-2}$ ). Since uncertainty is not part of the ECMWF data, a weight of 1.0 is assigned to ECMWF skin temperature data. As soon as cloud screened  $T_{10.8}$  become available from cloud screening after spin-up, they replace the ECMWF skin temperature data. ECMWF skin temperature data continue to be ingested during processing. They are used as a backup when long term cloud cover inhibits the compositing of clear sky brightness temperature. This is the case when cloud cover beyond  $\text{time}_{\text{max}}$  generates gaps of more than 7 hours in the diurnal clear sky brightness temperature data.

The diurnal cycle of clear sky brightness temperature  $T_{cf}$  is calculated by fitting a curve through all valid clear sky retrievals of  $T_{10.8}$ . Outliers in  $T_{10.8}$  are removed by only considering the 5-100% percentile for the clear sky diurnal time series of each pixel (only low outliers can occur, due to missed clouds during cloud screening).

For the diurnal temperature modeling the following sun orbital parameters need to be calculated. True solar time  $t$  (hours) is calculated from UTC (hours):

$$t = \text{UTC} + \lambda/15, \quad (50)$$

where  $\lambda$  is the longitude (degrees east) and  $t$  is cyclic within the bounds  $0 \dots 24$ . The sun's declination  $\delta$  (degrees) is approximated by:

$$\delta = 23.45 \sin\left(\frac{2\pi}{365}(D + 284)\right), \quad (51)$$

where  $D$  is the Day of Year ( $1 \dots 365$ ; leap years are constrained to 365 days for simplicity).

The diurnal cycle of clear sky  $T_{cf}$  is modeled by fitting either the thermal model by *Mannstein et al.* (1999) or by *Göttsche and Olesen* (2009) to the diurnal distribution of observed clear sky  $T_{10.8}$  values. Fitting is performed if the longest gap in the data covering the observed diurnal cycle is no longer than

7 hours. The *Mannstein et al.* (1999) model is chosen in the case when less than 10 clear sky observations are present for the whole day (for spin-up with 4 ECMWF skin temperature values or for prolonged periods of cloudiness) since only three instead of six parameters need to be estimated. Both models are suitable to represent the diurnal cycle of clear sky radiative surface temperature, which is needed as reference for cloud screening. They however cannot account for cloud effects needed to model the all sky radiative surface temperature.

### 6.2.1 Mannstein Model

The radiative surface temperature model by *Mannstein et al.* (1999) was modified by B. Dürr (2008, personal communication). The number of daylight hours  $N_d$  (hours) is first calculated:

$$N_d = \frac{24}{\pi} \arccos(\min(\max(-\tan \phi \cdot \tan \delta, -1), 1)), \quad (52)$$

where  $\phi$  is the latitude (degrees N) and  $N_d > 0.01$ . Note that all angles in this document are given in units degrees. They have to be converted to units radians when they are used as arguments to trigonometric functions except when otherwise noted. The diurnal course of clear sky brightness temperature is then calculated:

$$T_{cf}(t) = T_{\min} + T_a \left[ \exp \left( -8 \left( \frac{t - t_m}{N_d} \right)^2 \right) + 0.1 \sin \left( \frac{\pi}{12} (t - t_m) \right) \right]. \quad (53)$$

The exponential function describes daytime heating of the surface by use of a Gaussian curve and the sinusoidal term accounts for a time-lagged decay of radiative surface temperature after sunset. The function is analytical, has cyclic boundary conditions and can be differentiated. It contains three free parameters: minimum daily temperature  $T_{\min}$  (K), diurnal temperature amplitude  $T_a$  (K) and  $t_m$  (hours), the solar time of maximum heating. These three parameters can be estimated by use of a robust non-linear least square solver

(<http://www.physics.wisc.edu/~craigm/idl/fitting.html>) based on MINPACK-1

(<http://www.netlib.org/minpack>). Start values and parameter bounds are found in Table 4.

**Table 4:** Parameters of the *Mannstein et al.* (1999) model

No.	name	start value	lower bound	upper bound
1	$T_{\min}$	$\min(T_{10.8})$	$\min(T_{10.8}) - 10$	$\min(T_{10.8}) + 10$
2	$T_a$	$\max(T_{10.8}) - \min(T_{10.8})$	0.1	$\max(T_{10.8}) - \min(T_{10.8}) + 10$
3	$t_m$	12.5	10	16

The *Mannstein et al.* (1999) model has cyclic boundary conditions, which might be violated when synoptic weather conditions yield substantial temperature changes from one day to the next. This is demonstrated in Figure 5: in the lower left panel, the midnight temperature of the previous day is around 3-4 K lower than the midnight temperature 24 hours later not reproduced by the model. The three parameter model however is very robust to data quality issues as shown in the upper right panel: during the second half of the day brightness temperatures become affected by clouds. Cloudy brightness temperatures are lower than the clear sky brightness temperatures. The model is able to

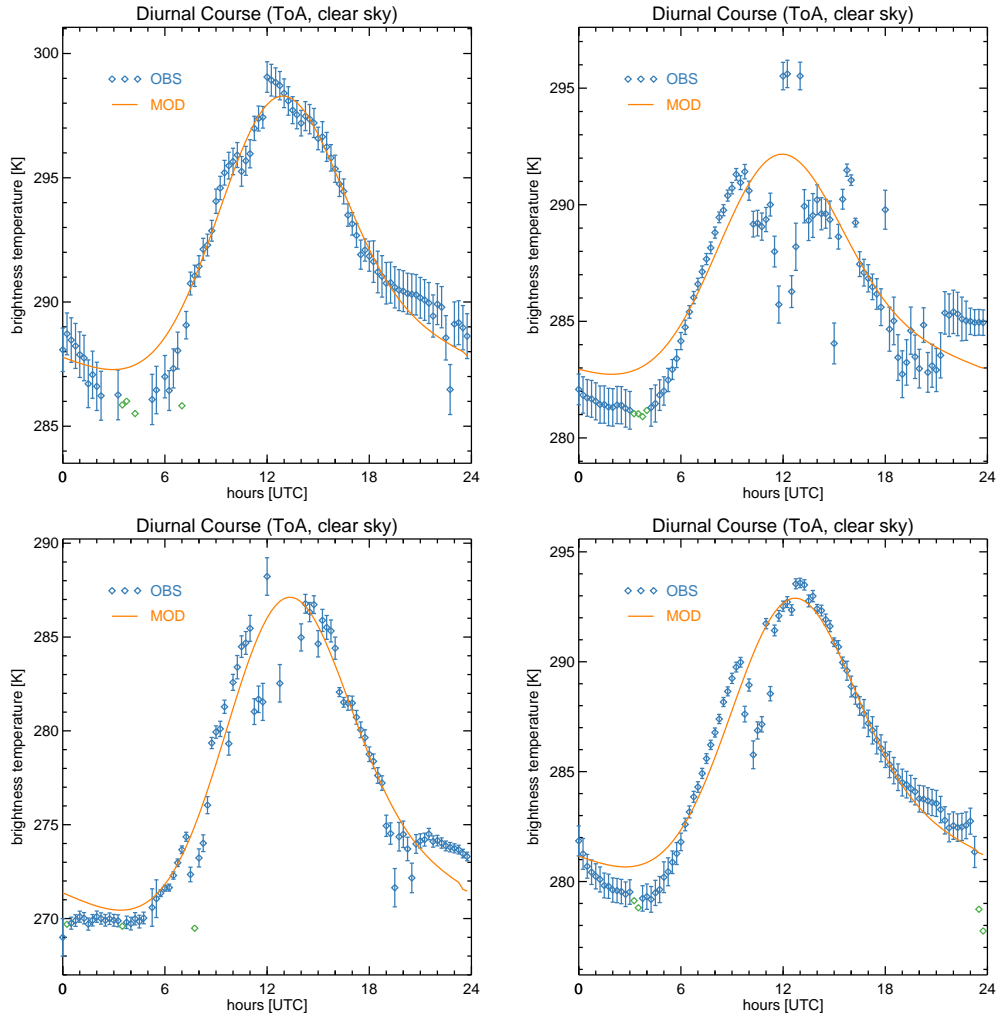


**Figure 5:** Meteosat clear sky brightness temperatures (blue) and corresponding model fits to the cloud masked data of the last 10 days by use of the *Mannstein et al.* (1999) model (orange) at four Alpine locations (see Table 3) on 5 August 2008.

partially reconstruct the midday peak of  $T_{cf}$  for this day. However, it cannot fully represent the continuous transition between the end of the night and the rapid increase of the  $T_{cf}$  after sunrise (upper left and right, and lower right panels).

The *Mannstein et al.* (1999) model uses only three parameters and is ideally suited to fit a “rough” diurnal course of  $T_{cf}$  with few cloud free observations available.

### 6.2.2 Göttsche Model

The diurnal course of clear sky brightness temperature is calculated:

$$T_{cf}(\theta) = \begin{cases} T_{\min} + T_a \cos(\theta_z) \frac{e^{\tau(m_{\min} - m(\theta_z))}}{\cos \theta_{z, \min}} & \text{if } \theta_h < \theta_s \\ T_{\min} + \delta T + \left[ T_a \cos \theta_{zs} \frac{e^{\tau(m_{\min} - m(\theta_{zs}))}}{\cos(\theta_{z, \min})} - \delta T \right] e^{\frac{-12}{\pi k}(\theta_h - \theta_s)} & \text{if } \theta_h \geq \theta_s, \end{cases} \quad (54)$$

where  $\theta_h = \frac{\pi}{12}(t - t_m)$  (radians) is the thermal hour angle with respect to the “thermal” noon at local solar time  $t_m$ ,  $\theta_s = \frac{\pi}{12}(t_s - t_m)$  (radians) is the thermal hour angle when “thermal” sunset occurs, with respect to the “thermal” noon at local solar time  $t_m$ .  $\theta_z = \arccos(\sin \delta \sin \phi + \cos \delta \cos \phi \cos \theta_h)$  (radians) is the sun zenith angle for hour angle  $\theta_h$  (analogous formulation for  $\theta_{zs}$  at zenith angle  $\theta_s$  and for the minimum zenith angle  $\theta_{z, \min}$  at “thermal” noon  $\theta_h = 0$ ). The optical air mass  $m$  (-) in dependence of the sun zenith angle  $\theta_z$  is calculated after *Vollmer and Gedzelmann* (2006):

$$m(\theta_z) = -\frac{R_E}{H} \cos \theta_z + \sqrt{\left(\frac{R_E}{H} \cos \theta_z\right)^2 + 2\frac{R_E}{H} + 1}, \quad (55)$$

where  $R_E = 6371000$  m is the earth’s radius and  $H = 8430$  m is the scale height of the dry atmosphere. The exponential decay constant  $k$  can be calculated by assuming differentiability everywhere and setting the derivatives of both equations for  $T_{cf}(\theta)$  equal at  $\theta_s$ :

$$k = \frac{12}{\pi} \frac{\frac{\partial \theta_z(\theta_s)}{\partial \theta_s} \cos \theta_{zs} - \frac{\delta T}{T_a} \frac{\cos \theta_{z, \min}}{e^{\tau(m_{\min} - m(\theta_{zs}))}}}{\sin \theta_{zs} + \tau \cos \theta_{zs} \frac{\partial m(\theta_{zs})}{\partial \theta_{zs}}}, \quad (56)$$

and where

$$\frac{\partial \theta_z(\theta_s)}{\partial \theta_s} = \frac{\sin \theta_s \cos \delta \cos \phi}{\sin \delta \sin \phi + \cos \delta \cos \phi \sin \theta_s}, \quad (57)$$

and where

$$\frac{\partial m(\theta_{zs})}{\partial \theta_{zs}} = \frac{R_E}{H} \cos \theta_{zs} - \frac{\frac{R_E^2}{H^2} \cos \theta_{zs} \sin \theta_{zs}}{\sqrt{\left(\frac{R_E}{H} \cos \theta_{zs}\right)^2 + 2\frac{R_E}{H} + 1}}. \quad (58)$$

The model contains six free parameters: the minimum daily temperature  $T_{\min}$  (K), diurnal temperature amplitude  $T_a$  (K), the solar time of maximum heating  $t_m$  (hours), the solar time of “thermal” sunset  $t_s$  (hours), the temperature difference between two consecutive days  $\delta T$  (K) and the atmospheric optical thickness  $\tau$  (-). These six parameters can be estimated by use of a robust non-linear least square solver (<http://www.physics.wisc.edu/~craigm/idl/fitting.html>) based on MINPACK-1 (<http://www.netlib.org/minpack>). Start values and parameter bounds are found in Table 5. The numerical fixes required in the model are:  $t_s > t_m$  and  $k > 1$ .

**Table 5:** Parameters of the *Göttsche and Olesen* (2009) model

No.	name	start value	lower bound	upper bound
1	$T_{\min}$	$\min(T_{10.8})$	$\min(T_{10.8}) - 10$	$\min(T_{10.8}) + 10$
2	$T_a$	$\max(T_{10.8}) - \min(T_{10.8})$	0.1	$\max(T_{10.8}) - \min(T_{10.8}) + 10$
3	$t_m$	12.5	12	15
4	$t_s$	17	14	20
5	$\delta T$	0	-5	5
6	$\tau$	0.03	0.001	2

The *Göttsche and Olesen* (2009) model does not have cyclic boundary conditions. Figure 6 demonstrates that it is able to accommodate changes in day-to-day surface temperature conditions. The two lower panels show that in comparison to the *Mannstein et al.* (1999) model the continuous

response of  $T_{cf}$  at sunrise is realistically simulated. However, at the expense of a missing decay after mid-night: the model assumes a constant  $T_{cf}$  prior to sunrise which is valid for the situation at the lower left panel but not at the lower right panel. The model specifically reproduces the asymmetric shape of the diurnal course of  $T_{cf}$  between morning and afternoon hours, which results in much more realistic slopes of the rising  $T_{cf}$  during morning hours compared to Figure 5. Like the *Mannstein et al.* (1999) model it is able to reconstruct the diurnal course of  $T_{cf}$  even with a substantial amount of cloud-affected clear sky brightness temperature observations.

The *Götttsche and Olesen* (2009) model uses six parameters and provides a realistic empirical approximation of the diurnal course of  $T_{cf}$  for a wide range of surfaces types and surface states. The fitting of six instead of three parameters, combined with a more complicated formulation, however make it around 5–10 times more computationally demanding when compared with the *Mannstein et al.* (1999) model.

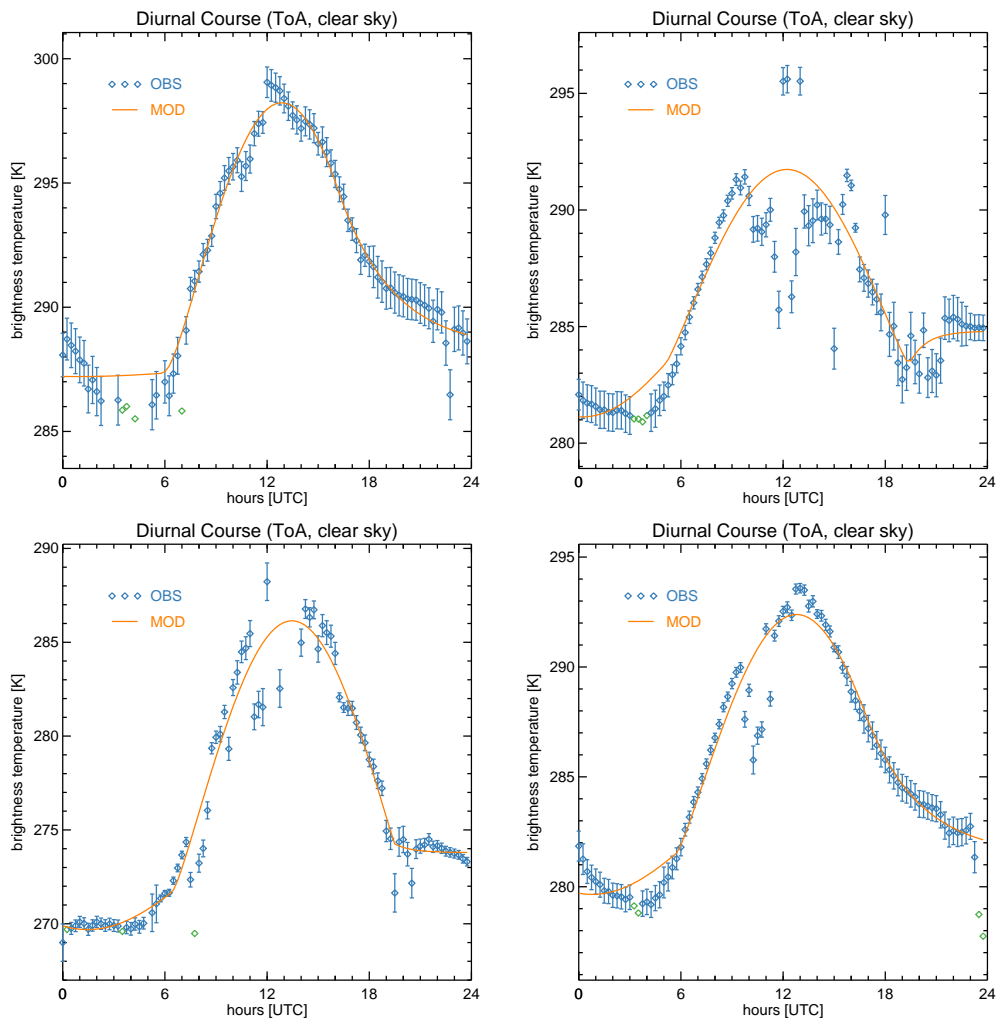


**Figure 6:** Meteosat clear sky brightness temperatures (blue) and corresponding model fits to the cloud masked data of the last 10 days by use of the *Götttsche and Olesen* (2009) model (orange) at four Alpine locations (see Table 3) on 5 August 2008.

### 6.3 Snow Mask

Daily snow compositing is performed by analyzing all valid diurnal  $\text{snow}_{\text{mask}}$  values from the most recent clear sky composites ( $\text{time}_{\text{mask}} < 5$  days) and setting the daily snow mask:

$$\text{snow}_{\text{mask}}^{\text{day}} = \begin{cases} 1 & \text{if } > 25\% \text{ of } \text{snow}_{\text{mask}} = 1 \\ 0 & \text{in all other cases} \end{cases}, \quad (59)$$

with the constraint that at least 10 valid  $\text{snow}_{\text{mask}}$  values from clear sky compositing need to be available.

### 6.4 Surface Albedo

The surface albedo  $\alpha_s$  is the broad-band hemispherical surface albedo in dependence of solar zenith angle. It is currently approximated by using the 25% quantile of the diurnal course of  $\rho_{\text{cf}}$ . However, since  $\rho_{\text{cf}}$  is narrow-band and it includes substantial scattering from atmospheric constituents at high solar and view angles, it should be replaced by a true physical retrieval of surface albedo with an accurate surface bidirectional reflectance function parameterization.

## 7 Clear Sky Radiation

Clear sky radiation defines the global radiation reaching the earth's surface under cloud free conditions. It can be estimated by use of empirical relationships that account for air mass or it can be calculated with an atmospheric radiative transfer model using individual components of atmospheric water vapor, ozone and aerosol content. Two clear sky models are implemented in "HelioMont": The empirical clear sky model by F. Kasten and the gnu-MAGIC libRadtran-based clear sky model by R. Müller. The latter one is selected for processing "HelioMont" datasets.

### 7.1 Kasten Clear Sky Model

The clear sky model by *Kasten et al.* (1984) is based on the integrated measure of the cloud-free atmospheric optical thickness called Linke Turbidity Factor  $T_L$  with an altitude-dependent correction (*Ineichen and Perez, 2002*). The algorithm was adapted and re-calibrated for Switzerland by *Dürr and Zelenka (2009)*:

$$I_{cf} = a_1 I_0 \epsilon \cos(\theta_s) \exp(-a_2 m_0 (f_{h_1} + f_{h_2}(T_L - 1))), \quad (60)$$

where

$$a_1 = 1.74 \cdot 10^{-5} z + 0.868 \quad (61)$$

$$a_2 = 6.81 \cdot 10^{-6} z + 0.0387 \quad (62)$$

$$f_{h_1} = \exp(-z/8000) \quad (63)$$

$$f_{h_2} = \exp(-z/1250), \quad (64)$$

and where  $z$  is the surface elevation (m),  $I_0 = 1367 \text{ W m}^{-2}$  is the solar constant (total solar irradiance) and  $\epsilon = d_s^{-2}$  is the correction for the earth's eccentricity with  $d_s$  being the astronomical sun-earth distance (AU).  $m_0$  is the optical air mass relative to the one of a standard atmosphere (*Kasten and Young, 1989*):

$$m = (\cos(\theta_s) + a_3(h + a_4)^{-a_5})^{-1}, \quad (65)$$

where  $a_3 = 0.15$ ,  $a_4 = 3.885$  and  $a_5 = 1.253$  and  $h$  is the solar elevation angle ( $90^\circ - \theta_s$ ). Further details can be found in above references. Monthly climatological  $T_L$  values are derived from a global turbidity database (<http://www.soda-is.com>) for the grid point  $47^\circ \text{ N}$  and  $7.5^\circ \text{ E}$  at 500 m elevation

and linearly interpolated to daily values by still allowing the daily means to reproduce the monthly mean value. A correction of  $\Delta T_L = -0.9$  is applied after *Dürr and Zelenka (2009)*. For regions lying outside of Switzerland new  $T_L$  climatologies would have to be acquired from the global turbidity database. Also, the month-to-month and inter-annual variability of  $T_L$  cannot be accounted for by using this method. A scientifically better and more flexible calculation of clear sky radiation fluxes is provided by the gnu-MAGIC clear sky model.

The Kasten model only calculates the clear sky global radiation flux. The splitting into direct beam and diffuse radiation components are performed during the all sky calculation in Section 8.9.1.

## 7.2 gnu-MAGIC Clear Sky Model

The open source and GNU-licensed Mesoscale Atmospheric Irradiance Code (MAGIC) is a computing-efficient and accurate estimation of clear sky global and direct beam irradiance (<http://sourceforge.net/projects/gnu-magic/>). It uses Radiative Transfer Model (RTM) calculations based on libRadtran (*Mayer and Kylling, 2005*). The RTM is executed offline for a range of atmospheric and surface states (aerosol optical depth, aerosol single scattering albedo, total column water vapor, total column ozone, solar zenith angle and surface albedo) using the DISORT solver (*Stamnes et al., 2000*) with 16 streams and the correlated-k distribution of the solar spectrum (*Kato et al., 1999*). This yields a lookup table with clear sky global and direct radiation fluxes depending on a discrete set of atmospheric and surface states. This look-up table (LUT) is then used during the clear sky irradiance calculations to reproduce the otherwise computationally inefficient RTM calculations with a few empirical equations, called Modified Lambert-Beer (MLB) equations. The MLB/LUT approach, also referred to as a “hybrid-eigenvector” approach (*Müller et al., 2004; Matsoukas, 2005; Müller et al., 2009*), assumes that the different atmospheric states (aerosols, water vapor, ozone) more or less act additively (independently from each other, or orthogonal) on the broadband shortwave atmospheric transmission. The MLB for clear sky global  $G_{cf}$  and direct beam  $B_{cf}$  radiation can be formulated as follows:

$$G_{cf} = G_{0,enh} \exp\left(\frac{-\tau_G}{\cos^{a_G}(\theta_s)}\right) \cos(\theta_s) + \Delta G_{H_2O} \cos^{b_G}(\theta_s) + \Delta G_{O_3} \cos^{c_G}(\theta_s) \quad (66)$$

$$B_{cf} = B_{0,enh} \exp\left(\frac{-\tau_B}{\cos^{a_B}(\theta_s)}\right) \cos(\theta_s) + \Delta B_{H_2O} \cos^{b_B}(\theta_s) + \Delta B_{O_3} \cos^{c_B}(\theta_s), \quad (67)$$

where  $G_{0,enh}$ ,  $B_{0,enh}$ ,  $\tau_G$ ,  $\tau_B$ ,  $a_G$ ,  $a_B$  are empirical parameters of the MLB model describing the aerosol forcing on clear sky global and direct beam radiation. They can be calculated from the LUT by aerosol optical depth, aerosol single scattering albedo and aerosol asymmetry factor. For aerosol optical depth and aerosol single scattering albedo the  $1^\circ \times 1^\circ$  monthly climatology by *Kinne (2008)* is used with bilinear interpolation. The LUT for aerosol optical depth ranges between 0 . . . 2 (-) in steps of 0.1. The LUT encompasses three single scattering albedo values (0.7, 0.85 and 1.0) and has a fixed value for the aerosol asymmetry factor (0.75).  $\Delta G_{H_2O}$ ,  $\Delta B_{H_2O}$ ,  $b_G$ ,  $b_B$  are the empirical parameters of the MLB model describing the total column water vapor forcing on global and direct beam radiation. The LUT for  $H_2O$  covers the range of 0.0 . . . 42.5 ( $\text{kg m}^{-2}$ ) in steps of 2.5. The ERA Interim total column water vapor (*Dee et al., 2011*) is used at a 6-hourly time step with bilinear interpolation from the  $1^\circ \times 1^\circ$  spatial resolution to the MSG HRV spatial resolution. Total column  $H_2O$



is downscaled to the actual topography on the MSG HRV spatial resolution by pressure (*Morland et al.*, 2006) with the use of an exponential vertical decay function and a scale height of 1000 m (scale heights of 500 . . . 3000 m are reported in literature).  $\Delta G_{O_3}$ ,  $\Delta B_{O_3}$ ,  $c_G$ ,  $c_B$  are the empirical parameters of the MLB model describing the total column ozone forcing on global and direct beam radiation. Since the sensitivity of clear sky global and direct beam radiation components to  $O_3$  is weak the ozone LUT only discriminates three values (200, 350 and 500 DU). ERA Interim total column ozone is used at a 6-hourly time step with bilinear interpolation from the  $1^\circ \times 1^\circ$  to the MSG HRV spatial resolution. No topographic downscaling is performed for ozone since ERA Interim primarily covers stratospheric ozone.

The original gnu-MAGIC keeps the  $a, b, c$  exponents, which account for the solar zenith angle dependency of RTM approximations, constant at values of 0.9 and 1.0, respectively. In our implementation these exponents are also parameterized since they vary between 0.4 - 1.0 depending on atmospheric state.  $G_{0,enh}$  and  $B_{0,enh}$  are empirical parameters to the MLB equations replacing the total solar irradiance  $I_0 = 1365 \text{ W m}^{-2}$  at the top of atmosphere (solar constant, integrated over all wavelengths of the spectral correlated-k distribution of *Kato et al.* (1999) ):

$$G_{0,enh} = \left( 1 + I_0 \frac{G - B}{B \cdot G} \right) I_0 \quad (68)$$

$$B_{0,enh} = G_{0,enh}, \quad (69)$$

They account for the enhanced clear sky global and direct beam irradiance due to the diffuse fraction at very low visibilities, where  $G$  and  $B$  are RTM-calculated clear sky global and direct beam radiation retrieved from the LUT for a given atmospheric and surface state. Specifically the use of  $G_{0,enh}$  provides a better fit than  $I_0$  to the RTM solution of  $G_{cf}$ . R. Müller (personal communication) suggests to use  $I_0$  instead of  $B_{0,enh}$  for the calculation of  $B_{cf}$ , which was not tested here.

Since all LUT values are calculated with the sun-earth distance set to 1 AU,  $G_{cf}$  and  $B_{cf}$  are next multiplied with the correction for the earth's eccentricity  $\epsilon = d_s^{-2}$  with  $d_s$  being the astronomical sun-earth distance (AU). In the original gnu-MAGIC this correction is only applied to the aerosol but not to the water vapor and ozone correction. Our implementation is thought to be more consistent as the sun-earth distance has a multiplicative effect on the total incoming radiation including its additive components.

The effect of surface albedo  $\alpha_s$  on diffuse radiation is empirically accounted for with the following fit:

$$G_{cf} = G_{cf}(0.98 + 0.1\alpha_s) \quad (70)$$

A script for the re-calculation of the clear sky LUT's is part of "HeliMont". It has been developed and tested with libRadtran version 1.6 (<http://www.libradtran.org>).

## 8 All Sky Radiation

The calculation of the all sky radiation fluxes is performed as follows: Firstly the maximum cloud reflectance needed by the Heliosat cloud index is calculated. Then the visible (Heliosat) cloud index and the newly developed infrared cloud index are calculated. They are combined into a single cloud index depending on the clear sky reflectance. The clear sky index is next derived from this combined cloud index. The surface solar radiation is calculated from the clear sky radiation and the clear sky index. Orographic shading, sky view and reflections from surrounding surfaces are taken into account. Daily sums of sunshine and mean radiation components are finally diagnosed from the instantaneous fields of surface solar radiation.

### 8.1 Maximum Cloud Reflectance

This section defines how the maximum cloud reflectance  $\rho_{\max}$  is calculated for the visible band selected for the Heliosat cloud index (either HRV, 0.6 or 0.8  $\mu\text{m}$ ). It can be empirically derived or calculated by use of a radiative transfer model. Both options are implemented in “Heliomont”. The radiative transfer model is selected for final processing.

The empirically derived  $\rho_{\max}$  primarily serves as a normalization factor for scaling relative to absolute cloud reflectance. It secondarily provides a means to account for uncalibrated satellite data (*Posselt et al.*, 2012). In Heliosat-based applications  $\rho_{\max}$  is often set to the 95% value of the reflectance histogram for a defined region with stratiform cloudiness. Since MSG data is well calibrated,  $\rho_{\max}$  has been set to a fixed reflectance value of 0.78. This value gives the best empirical fit to global radiation data at ASRB and BSRN stations.

A second and more physically-based method is to vary  $\rho_{\max}$  by the view and solar geometry of each pixel in order to account for directional properties of clouds. In order to achieve this the radiative transfer model libRadtran is executed for a set of sun zenith ( $0^\circ \dots 85^\circ$ ), view zenith ( $0^\circ \dots 85^\circ$ ), relative sun-view azimuth ( $0^\circ \dots 180^\circ$ ) angles and surface albedo (0.0  $\dots$  0.8) values using the U.S. standard atmospheric profile (*Anderson et al.*, 1986) with a cloud optical thickness of 128 (very thick clouds!) for the MSG SEVIRI high resolution visible (HRV) channel. The set-up uses the channel’s spectral filter function with the pseudo-spectral solar flux (correlated-k with SBDART by *Ricchiazzi et al.* (1998)). The DISORT radiative transfer solver (*Stamnes et al.*, 1988, 2000) is used to calculate ToA reflectances for the full range of sun-sensor geometries and surface albedos. Two look-up tables are generated, one for water and one for ice clouds. The water and ice cloud parameterization after *Hu and Stamnes* (1993) and *Fu et al.* (1998), respectively, have been used.

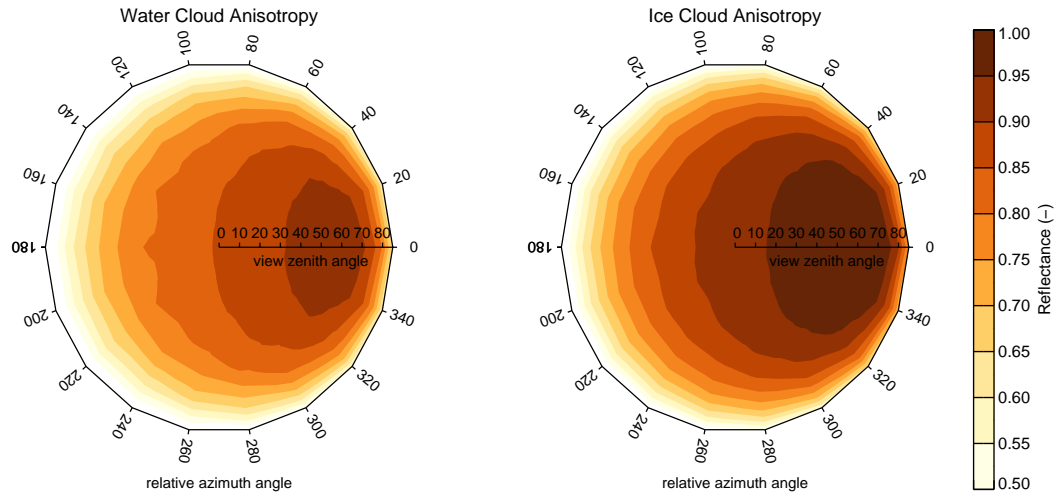


**Figure 7:** Cloud anisotropy for water (left) and ice (right) clouds using a cloud optical thickness of 128, a sun zenith angle of  $40^\circ$  and a surface albedo of 0.2.

The result is a look-up table useful to parameterize  $\rho_{\max}$  by view and solar geometry. An example is given in Figure 7 and demonstrates the generally high forward scattering anisotropy of clouds which is stronger for ice than for water clouds. The relative azimuth angle  $\phi_{v-s}$  follows the libRadtran definition (Section 10.4) where  $0^\circ$  azimuthal difference corresponds to the opposite direction of the sun and the satellite sensor. The anisotropy of the maximum cloud reflectance is calculated for each time step. Surface albedo is currently set to 0.2, since  $\rho_{\max}$  was found to be insensitive to surface albedo. The distinction between water and ice clouds is made with a simple formula where the fraction of water clouds  $\phi_{wc}$  of each pixel depends on the  $10.8 \mu\text{m}$  brightness temperature (*lpe*, submitted):

$$\phi_{wc} = \min \left( \max \left( \frac{T_{10.8} - T_{\min}}{T_{\max} - T_{\min}}, 0 \right), 1 \right), \quad (71)$$

where  $T_{\min} = 245\text{K}$  and  $T_{\max} = 265\text{K}$ . The LUT values for Ice and water clouds are then combined linearly by use of  $\phi_{wc}$ . The benefit of using a varying rather than a constant  $\rho_{\max}$  becomes apparent in regions with a high background reflectance. There, the dynamic range between the clear sky reflectance  $\rho_{cf}$  and cloudy reflectance  $\rho_{\max}$  decreases and the cloud index (see Section 8.2) has a stronger dependence on  $\rho_{\max}$ .

The  $\rho_{\max}$  LUT depends on the spectral properties of the channel which is used for the cloud index calculation. It needs to be re-calculated if a narrow-band channel like the SEVIRI  $0.6 \mu\text{m}$  or  $0.8 \mu\text{m}$  are used for the cloud index. All scripts required to re-calculate the LUT are provided with the MSG processing code. The latest version of libRadtran can be obtained as an open source code on <http://www.libradtran.org>.

## 8.2 Cloud Index (Visible)

The cloud index  $N_{\text{vis}}$  using the visible channel information is calculated by following the original HELIOSAT method (*Cano et al.*, 1986),

$$N_{\text{vis}} = \frac{\rho - \rho_{\text{cf}}}{\rho_{\text{max}} - \rho_{\text{cf}}} \quad (72)$$

where  $\rho$  is the instantaneous reflectance of the visible channel,  $\rho_{\text{cf}}$  is the slot-wise cloud free composite of previous visible channel reflectances (Section 6.1), and  $\rho_{\text{max}}$  is the maximum reflectance (Section 8.1) of a fully cloud covered pixel.  $N_{\text{vis}}$  is limited to values between -0.2 and 1.1 (Hammer *et al.*, 2003).

The visible cloud index has various deficiencies. Shadowed pixels receive a negative cloud index and are thus identified as exceptionally clear sky when  $\rho$  becomes smaller than  $\rho_{\text{cf}}$ . A treatment of shadows would also need to be accompanied by the treatment of the parallax effect including the proper adjustment of the three-dimensional sun-satellite-cloud view geometry. Due to the directional effects of snow reflectance, snow covered pixels on the other hand can have a high or unrealistically varying visible cloud index due to the small (or even negative) dynamic range between  $\rho_{\text{cf}}$  and  $\rho_{\text{max}}$  over snow.

### 8.3 Cloud Index (IR)

An infrared- and near-infrared cloud index  $N_{\text{ir}}$  is introduced by applying a power function to the T score and the modified R score of the cloud mask algorithm (Khlopenkov and Trishchenko, 2007),

$$N_{\text{ir}} = \min(\max(a(T_{\text{score}} - b) + c(R_{\text{score}} - d), 0)^e + N_{\text{min}}, N_{\text{max}}) \quad (73)$$

where

$$T_{\text{score}} = T_{\text{cf}} - T_{10.8} \quad (74)$$

and

$$R_{\text{score}} = 500 \frac{\rho_{0.6}^2 \rho_{1.6}^2}{1.5 \rho_{1.6}^{2.8} (3.0 \rho_{1.6} + 0.5 \rho_{0.6} + 3.5) + 1.5 \rho_{0.6}^{2.0}} \quad (75)$$

The  $T_{\text{score}}$  detects high and thick clouds independent of surface type and the  $R_{\text{score}}$  has a high performance of detecting even low clouds over bright surfaces.  $T_{\text{cf}}$  is the slot-wise cloud free composite (Section 6.2).

The power function provides the best regression of the infrared cloud index to the visible cloud index. Optical thickness of clouds only correlates to intermediate brightness temperature differences in the  $T_{\text{score}}$ . There is no sensitivity at very high and very low brightness temperature differences. “Thermal thickness” becomes unrelated to optical thickness with very thick clouds since the brightness temperature of optically thick clouds has a small penetration depth. On the other hand optically thick stratus clouds can have no thermal signature if they occur close to the surface. The  $R_{\text{score}}$  alleviates some of these issues. Further, optically thin clouds like cirrus do not leave any thermal signature in the  $T_{\text{score}}$ . It is recommended to add for instance the  $C_{\text{score}}$  or some information on temporal brightness temperature variability to above equations in order to account for cirrus clouds.

The coefficients  $a$ ,  $b$ ,  $c$ ,  $d$  and  $e$  are estimated once per day by fitting all daily  $N_{\text{ir}}$  to  $N_{\text{vis}}$  for pixels of the current day with a cloud free reflectance  $\rho_{\text{cf}} \leq 0.5$  (i.e. non snow covered pixels). Fitting is performed by three-dimensional regional bins covering 50 x 50 satellite pixels (north-south x

**Table 6:** Infrared cloud index parameter start values, lower and upper bounds and default values in the case of unsuccessful fitting.

No.	name	start value	lower bound	upper bound	default value
1	a	0.03	0.001	0.1	0.002
2	b	5	-20	30	-30
3	c	0.03	0.001	0.1	0.03
4	d	5	-20	30	4.6
5	e	1.5	1	5	1.1

west-east) and 500 m surface elevation difference. A set of parameters is estimated for each regional bin. The parameter sets are stratified by surface elevation since different cloud types in a regional scene are often bound to orographic features (low level fog, convective cells, orographic lifting). The fitting parameter start values including their lower and upper bounds are given in Table 6.

Parameters are estimated by use of the Leuvenberg-Marquardt least squares solver (<http://www.physics.wisc.edu/~craigm/idl/fitting.html>) based on the MINPACK-1 algorithm as part of Netlib (<http://www.netlib.org/minpack>) under the constraint that the parameters  $N_{\min} = 0$  and  $N_{\max} = 1.05$  are fixed. A fit is performed if at least 100 pixels in each bin have a valid visible cloud index and satisfy the above cloud free reflectance criterion. Successful fits are identified by having a Pearson correlation  $r > 0.7$ . Gaps in the three-dimensional set of bins are then filled by successively applying a volumetric inverse distance weighted spatial smoothing with radius 2, 3 and 4. Pixel-wise parameters are finally calculated by interpolating the parameter values from the regional bins to each pixel's  $x$ ,  $y$  and  $z$  location. Remaining gaps in the parameters are filled by using the default (start) parameter values. The pixel-wise infrared cloud index is finally calculated by applying the pixel-wise parameters to Equation 73.

## 8.4 Cloud Index (Combined)

A combined cloud index is calculated by using the visible cloud index for dark surfaces and the infrared cloud index for bright surfaces:

$$N = fN''_{\text{ir}} + (1 - f)N_{\text{vis}} \quad (76)$$

where

$$f = \min \left( \max \left( \frac{\rho_{\text{cf}} - 0.3}{0.5 - 0.3}, 0 \right), 1 \right), \quad (77)$$

$$N''_{\text{ir}} = N'_{\text{ir}} - \alpha N'_{\text{ir}} + \alpha N'^2_{\text{ir}}, \quad (78)$$

$$N'_{\text{ir}} = (N_{\text{ir}} - b)/a. \quad (79)$$

The combined cloud index  $N$  is thus a linear combination of the visible and the infrared cloud index, where only the visible cloud index is used for  $\rho_{\text{cf}} \leq 0.3$  and only the infrared cloud index is used for

$\rho_{cf} \geq 0.5$ . The infrared cloud index is also used if the visible cloud index cannot be estimated due to missing  $\rho_{cf}$ , such as for instance for prolonged periods of permanent cloud cover.

The infrared cloud index  $N'_{ir}$  is modified from  $N_{ir}$  in dependence of surface albedo  $\alpha_s$ . This empirically decreases the radiative effects of clouds for bright surfaces in an attempt to account for multiple surface-cloud reflections especially over snow cover. The parameters  $a = 1.45$  and  $b = 0.075$  were estimated with ASRB station data.

## 8.5 Clear Sky Index

The clear sky index  $K$  is calculated from the cloud index  $N$  by use of empirical relationships presented in *Hammer et al. (2003)*:

$$N \leq -0.2 : K = 1.2 \quad (80)$$

$$-0.2 < N \leq 0.8 : K = 1 - N \quad (81)$$

$$0.8 < N \leq 1.1 : K = 2.0667 - 3.6667N + 1.6667N^2 \quad (82)$$

$$1.1 < N : K = 0.05 \quad (83)$$

Full clear sky yields a  $K = 1.2$  (120% transmittance for global radiation) and full cloud cover yields a  $K = 0.05$  (5% transmittance for global radiation).  $K$  is above 100% for negative cloud indices and thus very dark surfaces (darker than the background). Such situations very often result from cloud shadows and not from exceptionally clear skies. A better treatment of cloud shadows however requires the simultaneous treatment of cloud parallax. The  $K$  parameterization should also be re-calibrated with long term climatological surface radiation measurements.

## 8.6 Shadows from Terrain

Terrain shadow from the surrounding horizon  $S_t$  is calculated by comparing the solar elevation angle  $H_s = 90^\circ - \theta_s$  to the horizon elevation angle  $H_t$  in the mean direction of the horizon azimuthal sector  $a$  ( $0 \dots [n_a - 1]$ ) closest to the actual sun azimuth direction  $\phi_s$ ,

$$a = \min(\text{ceil}(\phi_s n_a / 360 - 0.5), n_a - 1), \quad (84)$$

The number of azimuthal sectors  $n_a$  is a user definable parameter. In "HelioMont" it was set to 100 corresponding to a azimuthal sector width of  $3.6^\circ$ .

$$H_s \leq H_t : S_t = 1 \quad (85)$$

$$H_s > H_t : S_t = 0 \quad (86)$$

## 8.7 Shadows from Tilted Planes

In addition to terrain shadow on flat surfaces, tilted planes (e.g. solar modules or local terrain) can generate self-shadowing due to their decreased sky view and orientation. Tilted plane shadow  $S_p$  is diagnosed from  $\theta_{s-p}$  (Section 10.3),

$$\theta_{s-p} > 90^\circ : S_p = 1 \quad (87)$$

$$\theta_{s-p} \leq 90^\circ : S_p = 0. \quad (88)$$

Note that all angles in this document are given in units degrees. They have to be converted to units radians when they are used as arguments to trigonometric functions unless otherwise noted. The above calculation can be omitted in flat terrain where  $\theta_p = 0^\circ$ .

## 8.8 Shadows from Clouds

There is both a radiometric and a geometric cloud shadow detection implemented. The radiometric cloud shadow detection empirically diagnoses a continuous shadow metric from the clear sky and all sky reflectance:

$$S_c = 1 - \min \left( \max \left( \frac{\rho - a\rho_{cf}}{b\rho_{cf} - a\rho_{cf}}, 0 \right), 1 \right), \quad (89)$$

where  $a = 0.5$  and  $b = 0.9$  give the dynamic range of the shadow in relation to the clear sky reflectance. Thus,  $S_c$  becomes larger for surfaces which are darker than the non-shadowed clear sky reflectance.  $S_c$  is 1 when the all sky reflectance falls below 50% of  $\rho_{cf}$  and decreases to 0 when it reaches 90% of  $\rho_{cf}$ .

Cloud shadow can also be detected based on geometric calculations when cloud height, sun and satellite position are known (*Simpson and Stitt*, 1998; *Simpson et al.*, 2000b,a). The eastward and northward shift  $\Delta x$  (m) and  $\Delta y$  (m) of the cloud shadow for cloudy pixels (cloud mask value 1 or 2, see Section 5) in relation to the cloud position itself is calculated by using the previously calculated cloud height  $H_c$  (m) from Section 12.2, corrected by a cloud height shift  $\delta H_c$  (m):

$$\Delta r_v = \frac{H_c + \delta H_c}{\tan(90 - \theta_v)} \quad (90)$$

$$\Delta x_v = \Delta r \sin(\phi_v - 180) \quad (91)$$

$$\Delta y_v = \Delta r \cos(\phi_v - 180) \quad (92)$$

$$\Delta r_s = \frac{H_c + \delta H_c}{\tan(90 - \theta_s)} \quad (93)$$

$$\Delta x_s = -\Delta r \sin(\phi_s - 180) \quad (94)$$

$$\Delta y_s = -\Delta r \cos(\phi_s - 180). \quad (95)$$

Note that all angles in this document are given in units degrees. They have to be converted to units radians when they are used as arguments to trigonometric functions unless otherwise noted. These shifts are translated back into geographic coordinates:

$$\Delta \lambda_c = \frac{360(\Delta x_v + \Delta x_s)}{2\pi R \cos(\phi)} \quad (96)$$

$$\Delta \phi_c = \frac{360(\Delta y_v + \Delta y_s)}{2\pi R}, \quad (97)$$

where  $R$  (m) is the radius of the earth. These shifts are added to the geographic coordinates of Meteosat pixels:

$$\lambda_c = \lambda_{col,lin} + \Delta \lambda_c \quad (98)$$

$$\phi_c = \phi_{col,lin} + \Delta \phi_c. \quad (99)$$

For each cloudy pixel a new shifted column and line pair  $col_c$  and  $lin_c$  are calculated by use of the forward projection routines given in Section 11. In the ideal case the pixels covering the shifted column and line pairs should provide the geometric location of cloud shadows. The following adaptations are required to make the algorithm perform under real conditions:

- Cloud shadows cannot be present for pixels that are simultaneously marked as cloudy (the shifted cloud shadow may fall on another cloud top). Shadow-casting of a cloud onto another cloud cannot be resolved by this simplified algorithm.
- Cloud shadowed pixels are extended by use of spatial convolution with a binary kernel of 2 x 2 pixels. This procedure is required to fill gaps in the above geometric shift calculation. A cloud geometric reprojection by use of triangulation or bilinear interpolation would resolve this issue.
- The cloud height  $H_c$  can be biased and thus yield a wrong geometric shift of cloud shadows. A iterative optimization procedure is thus applied, where  $\delta H_c$  is varied by  $\pm 1000$  m in steps of 100 m. The most suitable value of  $\delta H_c$  is found by minimizing the mean reflectance of cloud shadowed pixels. Thus, wrong cloud heights potentially include cloudy or non-shadowed pixels in the geometric cloud shadow locations which raises the mean reflectance value.



Finally, a binary cloud shadow metric  $S_c$  is found by setting all pixels with cloud shadow to 1.

## 8.9 Surface Radiation

The surface radiation and its components are calculated differently for the Kasten clear sky model and for the gnu-MAGIC clear sky model. Both formulations are given here for completeness. The gnu-MAGIC clear sky model option is used for final processing.

### 8.9.1 Kasten-based Surface Radiation

The following calculations are carried out for solar zenith angles below  $\theta_s = 88^\circ$ . Global radiation  $G$  is calculated according to the original Heliosat method by *Cano et al.* (1986). It uses the clear sky index  $K$  and clear sky (cloud free) surface irradiance  $I_{cf}$ ,

$$G = K * I_{cf} \quad (100)$$

The fraction  $f_{dif}$  of diffuse relative to global radiation is calculated according to the model of *Skartveit and Olseth* (1987),

$$K < k_0 : f_{dif} = 1.0 \quad (101)$$

$$k_0 \leq K \leq \alpha k_1 : f_{dif} = f(K) \quad (102)$$

$$K > \alpha k_1 : f_{dif} = 1 - \alpha k_1 (1 - f(\alpha k_1)) / K, \quad (103)$$

where

$$f(K) = f(l) = 1 - (1 - d_1)(a\sqrt{l} + bl + (1 - a - b)l^2), \quad (104)$$

and where

$$l = 0.5 \left( 1 + \sin \pi \left( \frac{K - k_0}{k_1 - k_0} - 0.5 \right) \right). \quad (105)$$

The original empirically defined coefficients  $k_0 = 0.20$ ,  $k_1 = 0.87 - 0.56e^{-0.06h}$ ,  $\alpha = 1.09$ ,  $d_1 = 0.15 + 0.43e^{-0.06h}$ ,  $a = 0.27$ ,  $b = 0.00$  are used and  $h$  is the solar elevation angle in degrees ( $h = 90 - \theta_s$ ). Direct beam  $B$  and diffuse  $D$  radiation are calculated without shadowing effects on the horizontal plane,

$$B = (1 - f_{dif})G \quad (106)$$

$$D = f_{dif}G \quad (107)$$

Direct beam radiation receives a simple empirical adjustment for surface albedo  $\alpha_s$  effects (Richard Mueller, pers. comm.):

$$B = B(0.98 + 0.1\alpha_s) \quad (108)$$

### 8.9.2 gnu-MAGIC-based Surface Radiation

The gnu-MAGIC clear sky model calculates both clear sky global and clear sky direct beam radiation. This enhances the realism of the all sky direct beam component since the clear sky atmospheric content has a much higher impact on direct beam radiation than it has on global radiation. By having separate clear sky global and direct beam radiation fluxes a simple formulation can be used for calculating the non-shadowed all sky global, direct beam and diffuse radiation on the horizontal plane:

$$G = K * G_{cf} \quad (109)$$

$$B = f_{dir} B_{cf} \quad (110)$$

$$D = G - B, \quad (111)$$

where

$$f_{dir} = \begin{cases} (K - 0.38(1 - K))^{2.5} & \text{if } K \geq 0.5; \\ 0 & \text{if } K < 0.5 \end{cases} \quad (112)$$

According to Müller *et al.* (2009) the above empirical equation for  $f_{dir}$  is derived from the Skartveit and Olseth (1987) model.  $B$  is set to 0 below a clear sky index of 0.5 since direct beam radiation can be ignored beyond a certain cloud optical thickness.

### 8.10 Radiation in Terrain

Terrain and cloud shadows are added to calculate the direct normal  $DNI$ , direct beam  $B$  and diffuse  $D$  radiation components:

$$DNI_t = B(1 - S_t)(1 - S_c)/\cos(\theta_s) \quad (113)$$

$$B_t = B(1 - S_t)(1 - S_c) \quad (114)$$

$$D_t = f_{sky} D + \alpha_s(1 - f_{sky})(B + D), \quad (115)$$

where terrain shadow  $S_t$  and cloud shadow  $S_c$  inhibit direct beam radiation.

### 8.11 Radiation on a Tilted Plane

A tilted plane can generate self-shadowing  $S_p$  (Section 8.7). The direct beam radiation is reprojected onto the tilted plane by using the angle between the sun direction and normal to the plane  $\theta_{s-p}$  (Section 10.3). For a horizontal surface  $\theta_{s-p}$  equals to  $\theta_s$ . For a tilted plane the sky view factor  $f_{sky,p}$

is calculated differently than for surfaces with a regular horizon (see Section 9.5 ).

$$DNI_p = DNI_t(1 - S_p) \quad (116)$$

$$B_p = B_t(1 - S_p)\cos(\theta_{s-p})/\cos(\theta_s) \quad (117)$$

$$D_p = f_{sky,p}D_t + \alpha_s(1 - f_{sky,p})(B + D), \quad (118)$$

For a tilted plane the surface area relative to the horizontal surface area becomes larger. This “effective” surface area is optionally accounted for when the radiation flux per tilted surface area is requested instead of the usual radiation flux per horizontal surface area:

$$B_e = \frac{B_p}{\cos \theta_p}. \quad (119)$$

## 8.12 Global Radiation

Global radiation is finally summed up from direct beam and diffuse radiation components:

$$G_x = B_x + D_x, \quad (120)$$

where x represents either the horizon-free non-terrain-shadowed, terrain-shadowed (t) or tilted plane (p) solar surface radiation flux components.

## 8.13 Sunshine Duration

The daily absolute sunshine duration [h] is calculated at the end of each day by summing up  $\Delta t$  over all daily time steps where the pyranometric criterion of sunshine duration (*World Meteorological Organization*, 2008) is fulfilled:

$$B/\cos(\theta_s) > 120\text{Wm}^{-2}. \quad (121)$$

The criterion has to be applied to  $B$  normalized by the cosine of the solar zenith angle (Section 8.2 of *World Meteorological Organization* (2008)). Daily relative sunshine duration is calculated at the end of the day by dividing absolute sunshine duration with the sum of all time steps where the pyranometric criterion is fulfilled for non-shadowed clear sky irradiance,

$$I_{cf}/\cos(\theta_s)(1 - S_T) > 120\text{Wm}^{-2}. \quad (122)$$

No correction is applied in the case of missing daytime satellite data . Both absolute and relative sunshine duration will be underestimated in such a case.

## 9 Static Boundary Conditions

### 9.1 Water Mask

A water mask is needed for navigation (using a coastline matching method) and for separating cloud masks tests over land and ocean. The water mask is based on the publicly available Global, Self-consistent, Hierarchical, High-resolution Shoreline (GSHHS) database (*Wessel and Smith, 1996*), version 2.1. The GSHHS vector data is available in a spatial resolution of up to 100 m, which allows a precise delineation of water bodies with an area of 1 km<sup>2</sup> or higher coherent with the maximum pixel resolution of the HRV channel on the MSG SEVIRI sensor. GSHHS includes four levels of detail: 1: ocean vs. land; 2: lake on land; 3: island on lake; 4: pond on island. Only levels 1 and 2 are used in “HelioMont”. The water mask is calculated by firstly filling the polygons with the level 1 GSHHS data for delineating ocean from land and then filling the polygons for the lakes within the land. In order to separate individual water bodies for navigation, each polygon and its content is numbered from 1..*n* where 1 is the global ocean and higher numbers are lakes on land.

The water mask is available on a regular longitude/latitude grid with 300 pixels per degree grid spacing based on the GSHHS vector data. It is then reprojected to both the orthorectified and non-orthorectified MSG SEVIRI grid in the HRV or VIS, NIR and IR resolution by taking the median of the area covered by the elevation data for each MSG pixel.

### 9.2 Elevation

A digital elevation model (DEM) is needed for several parts of the “HelioMont” processing:

- orthorectification of the satellite data
- downscaling of meteorological boundary conditions like surface skin temperature or total column water vapor
- normalizing surface reflectances with respect to terrain slope and aspect
- calculation of the horizon, the sky view factor and terrain shadow for deriving surface solar radiation in terrain
- empirical fitting of geospatial coefficients when for instance relating the visible to the infrared cloud index.

The Consultative Group on International Agricultural Research (CGIAR) Shuttle Radar Topography Mission (SRTM) DEM data is applied in “HelioMont”. In contrast to the original SRTM data provided by

the United States Geographical Survey (USGS) the CGIAR SRTM (<http://srtm.csi.cgiar.org>, Version 4) is almost free of artifacts and gaps. It offers a seamless coverage from 60° N to 60° S. Beyond these geographical bounds the GTOPO30 DEM (USGS, 1996) is used.

The elevation data  $z_{\text{srtm}}$  (m) is first reprojected from the regular geographical grid at its native resolution of 3" into the MSG SEVIRI projection of the HRV or VIS, NIR and IR resolution by taking the median of the area covered by the elevation data for each MSG pixel:

$$z(\text{col}, \text{lin}) = \tilde{z}_{\text{srtm}}(\lambda(\text{col}, \text{lin}) \pm 0.5\Delta\lambda(\text{col}, \text{lin}), \phi(\text{col}, \text{lin}) \pm 0.5\Delta\phi(\text{col}, \text{lin})), \quad (123)$$

where  $\pm\Delta\lambda(\text{col}, \text{lin})$  and  $\pm\Delta\phi(\text{col}, \text{lin})$  are the longitude and latitude spacing for a MSG SEVIRI pixel with line number lin and column number col.

The elevation data  $z_{\text{srtm}}$  (m) is secondly reprojected from the regular geographical grid at its native resolution of 3" into the "raw" non-orthorectified MSG SEVIRI projection in order to allow elevation-dependent calculations prior to orthorectification. Meteosat line and column orthorectification shifts are calculated as given in Section 12.1. Triangulation is used to reverse-orthorectify the longitude and latitude values for the MSG SEVIRI grid into the "raw" non-orthorectified grid  $\lambda_{\text{raw}}$  and  $\phi_{\text{raw}}$ . The elevation data is then projected into the "raw" non-orthorectified grid by taking the median of the area covered by the elevation data for each MSG pixel:

$$z_{\text{raw}}(\text{col}, \text{lin}) = \tilde{z}_{\text{srtm}}(\lambda_{\text{raw}}(\text{col}, \text{lin}) \pm 0.5\Delta\lambda(\text{col}, \text{lin}), \phi_{\text{raw}}(\text{col}, \text{lin}) \pm 0.5\Delta\phi(\text{col}, \text{lin})). \quad (124)$$

### 9.3 Terrain Aspect and Slope

In order to calculate the terrain aspect and slope for MSG SEVIRI pixels, the longitude and latitude values of each pixel are first converted into an orthographic projection (forward projection, see Section 11 ). The orthographic north-south and west-east pixel distances  $\Delta x$  (m) and  $\Delta y$  (m) for each grid point are then calculated by subtracting each pixel's x and y location from its neighbor location. The north-south and west-east elevation gain  $\dot{z}_x$  and  $\dot{z}_y$  are calculated by using convolution to run a pixel-centered finite differencing on the elevation data  $z$  (m), normalized by the pixel's orthographic distances:

$$\dot{z}_x(\text{col}, \text{lin}) = \frac{\sum_{i=0}^{k-1} z(s, \text{lin})K_i}{(k-1)\Delta x}, \text{ where} \quad (125)$$

$$s = \min(\max(\text{col} + i - k/2, \text{col}_{\text{min}}), \text{col}_{\text{max}}), \quad (126)$$

$$\dot{z}_y(\text{col}, \text{lin}) = \frac{\sum_{i=0}^{k-1} z(\text{col}, t)K_i}{(k-1)\Delta y}, \text{ where} \quad (127)$$

$$t = \min(\max(\text{lin} + i - k/2, \text{lin}_{\text{min}}), \text{lin}_{\text{max}}), \quad (128)$$

where  $K = [-1, 0, 1]$  is the convolution kernel of size  $k = 3$ . Slope  $\theta_t$  and aspect  $\phi_t$  of each pixel can then be calculated:

$$\theta_t = \arctan(\sqrt{\dot{z}_x^2 + \dot{z}_y^2}) \quad (129)$$

$$\phi_t = \text{mod}[180 + \arctan(\dot{z}_x, \dot{z}_y), 360] \quad (130)$$

Note that all angles in this document are given in units degrees. They have to be converted to units radians when they are used as arguments to trigonometric functions unless otherwise noted.

## 9.4 Horizon

The horizon calculation follows standard procedures used in geographical data analysis. The horizon is defined as the maximum elevation angle of the terrain in a given azimuthal direction. The algorithm used for the “HelioMont” processing requires some specific thoughts. Firstly, the horizon should be representative for an area covering the footprint of a Meteosat SEVIRI pixel instead of a point location. Secondly, the algorithm should further be computationally efficient in order to allow pixel-wise horizon calculations. The algorithm as formulated by *Funk* (1984) was implemented by *Dürr and Zelenka* (2009) in “HelioMont” and successively adapted here for performance and scalability.

The horizon calculation for Meteosat requires some pre-processing of the elevation data (see Section 9.2 ). It is read with its boundary extended by  $0.25^\circ$  in each direction with respect to the maximum geographical extent of the irregular MSG SEVIRI grid. It is then upsampled to the satellite resolution by area-averaging to  $0.01^\circ$  grid spacing for the HRV channel ( $0.025^\circ$  for regular SEVIRI channels). The averaged elevation data is then reprojected into the orthographic projection (see Section 11 ) where the center longitude and latitude of the projection is given by the mean of the MSG SEVIRI longitudes and latitudes. The reprojection uses bilinear interpolation and results in a regular orthographic elevation grid with grid extents corresponding to the maximum extents of the input elevation grid in geographical coordinates and grid spacing corresponding to the mean latitudinal grid spacing (approximately 1100 m for SEVIRI HRV) of the input elevation grid.

In order to calculate the horizon  $H_t$  ( $^\circ$  Elevation), each MSG SEVIRI pixel is reprojected onto the above orthographic grid. The maximum elevation angle by azimuthal direction is then diagnosed with a search radius of 25 km. The number of azimuthal direction can be freely chosen. It is however recommended to keep it above 50 for getting reasonably accurate horizons in complex terrain. The original code performed a pixel-wise rotation of the whole orthographic grid by azimuthal direction. Similar accuracy is now achieved with higher computational efficiency by pre-computing the radial indices for each azimuthal direction and performing a bilinear interpolation of cartesian to polar coordinates for each pixel. The polar representation of the area surrounding each pixel is then tested for the maximum elevation angle. 10–20 m are added to the center elevation in order to avoid the so-called “shoe box effect”, where a false horizon can be generated from a numerical artifact when surrounding elevation grid boxes are slightly higher than the center grid box. The horizon  $H_t$ , as defined here, is limited to positive values and the earth’s curvature is neglected.

## 9.5 Sky View Factor

The sky view factor algorithm was developed by Antoine Zelenka (MeteoSwiss, pers. comm.) for use with tilted planes. It has been successfully applied to numerical weather prediction by *Buzzi* (2008). The sky view factor  $f_{\text{sky}}$  is calculated by a discrete integration of the horizon through  $n_a$  azimuthal sectors  $i$  by use of a constant horizon for each sector:

$$f_{\text{sky}} = \frac{1}{\pi} \sum_{i=0}^{n_a-1} f_i. \quad (131)$$

Each azimuthal sector  $i$  covers the azimuth range  $\Delta\phi_a = 360^\circ/n_a$ , centered at the respective azimuthal direction. The tilted plane aspect angle  $\phi_p$  defines the starting point of the integration, which is the left edge of the tilted plane when viewed in the direction of  $\phi_p$ :

$$\phi_a^i = i\Delta\phi_a - (\phi_p - 90^\circ), \quad (132)$$

where  $\phi_a^i$  is constrained to the range of  $0^\circ \dots 360^\circ$  by use of a modulo operation. The tilted plane slope  $\theta_p$  generates a second horizon  $H_p$  in addition to the horizon of the surrounding terrain  $H_t$ :

$$H_p^i = \arctan \left( -\sin \phi_a^i \frac{\sin \theta_p}{\cos \theta_p} \right) \quad (133)$$

The sky view factor is then integrated clockwise. The integration firstly covers the  $180^\circ$  range where the plane elevation is always lower than the horizon followed by the  $180^\circ$  range where the plane elevation can be higher than the horizon. If  $H_t^i > H_p^i$  and  $H_t^i \geq H_p^{i+1}$ :

$$f_i = \frac{\cos \theta_p}{2} (\cos H_t^i)^2 (\phi_a^{i+1} - \phi_a^i) - \frac{\sin \theta_p}{2} (H_t^i + \sin H_t^i \cos H_t^i) (-\cos \phi_a^{i+1} + \cos \phi_a^i). \quad (134)$$

If  $H_t^i > H_p^i$  and  $H_t^i < H_p^{i+1}$ :

$$f_i = \frac{\cos \theta_p}{2} (\cos H_t^i)^2 (\phi_{g1}^i - \phi_a^i) - \frac{\sin \theta_p}{2} (H_t^i + \sin H_t^i \cos H_t^i) (-\cos \phi_{g1}^i + \cos \phi_a^i) + \frac{\sin \theta_p}{2} (H_p^{i+1} \cos \phi_a^{i+1} - H_t^i \cos \phi_{g1}^i) + \frac{1}{2} (\arctan \frac{\tan \phi_a^{i+1}}{\cos \theta_p} - \arctan \frac{\tan \phi_{g1}^i}{\cos \theta_p}), \quad (135)$$

where the  $\arctan$  function equals the nominator of the function when the nominator is  $\pi/2$  and  $3\pi/2$ , respectively, and where

$$\phi_{g1}^i = \arcsin \left( \frac{\tan H_t^i}{\tan \theta_p} \right) + \pi. \quad (136)$$

If  $H_t^i \leq H_p^i$  and  $H_t^i \leq H_p^{i+1}$ :

$$f_i = \frac{\sin \theta_p}{2} (H_p^{i+1} \cos \phi_a^{i+1} - H_p^i \cos \phi_a^i) + \frac{1}{2} (\arctan \frac{\tan \phi_a^{i+1}}{\cos \theta_p} - \arctan \frac{\tan \phi_a^i}{\cos \theta_p}). \quad (137)$$

And finally, if  $H_t^i \leq H_p^i$  and  $H_t^i > H_p^{i+1}$ :

$$f_i = \frac{\sin\theta_p}{2}(H_t^i \cos\phi_{g2}^i - H_p^i \cos\phi_a^i) + \frac{1}{2}(\arctan \frac{\tan\phi_{g2}^i}{\cos\theta_p} - \arctan \frac{\tan\phi_a^i}{\cos\theta_p}) + \frac{\cos\theta_p}{2}(\cos H_t^i)^2(\phi_a^{i+1} - \phi_{g2}^i) - \frac{\sin\theta_p}{2}(H_t^i + \sin H_t^i \cos H_t^i)(-\cos\phi_a^{i+1} + \cos\phi_{g2}^i), \quad (138)$$

where

$$\phi_{g2}^i = 2\pi - \arcsin\left(\frac{\tan H_t^i}{\tan\theta_p}\right). \quad (139)$$

## 9.6 Satellite View Angles

The satellite view zenith angle  $\theta_v$  and view azimuth angle  $\phi_v$  are calculated for each satellite pixel. They give the view geometry of the observer at the center of the pixel in the direction of the satellite sensor. For geostationary satellite platforms these angles could be handled as static fields. However, during the operation period the satellite position can drift by as much as  $1^\circ$ . This requires the constant re-adjustment of the satellite view angles. Also, two redundant operational geostationary satellites are often located at slightly different orbital positions. They provide imagery in alternating mode in order to guarantee a continuous data stream even during times when one instrument performs maintenance. For MSG, sub-satellite longitude are known to vary between  $-3.4^\circ$  East and  $10^\circ$  East.

Despite the view geometry being rectified to a standard ( $0^\circ$  East for Meteosat Prime) centered grid by EUMETSAT, the view geometry of the rectified grid still needs to be adjusted based on the true sub-satellite longitude (the sub-satellite latitude is assumed to be  $0^\circ$  North for geostationary platforms), and possibly, the actual satellite height. Currently only the actual sub-satellite longitude is examined for each slot and satellite view angles are re-calculated at every sub-satellite longitude change.

First, the geocentric latitudes of the observer  $\phi'_{\text{obs}}$  and the satellite instrument  $\phi'_{\text{sat}}$  are calculated from their geographic (geodetic, corresponding to the WGS84 ellipsoid) latitudes  $\phi_{\text{obs}}$  and  $\phi_{\text{sat}}$ :

$$\phi' = \arctan\left[\tan(\phi)(1-f)^2\right], \quad (140)$$

where

$$f = \frac{R_E - R_P}{R_E} \quad (141)$$

is the earth's flattening, and where  $\phi_{\text{obs}}$  corresponds to the pixel's center latitude  $\phi$  and the equatorial and polar earth radius  $R_E$  (m) and  $R_P$  (m) are defined as given in *Coordination Group for Meteorological Satellites* (1999). Geocentric longitude exactly corresponds to geographic (geodetic) longitude. Next the observer height in relation to the earth's center is calculated from the observer latitude:

$$H_{\text{obs}} = R_E \left(1 - \frac{e^2 s^2}{2} + \frac{e^4 s^2}{2} - \frac{5e^4 s^4}{8}\right) + z_{\text{obs}}, \quad (142)$$



where

$$e = \frac{\sqrt{R_E^2 - R_P^2}}{R_E} \quad (143)$$

$$s = \sin \phi_{\text{obs}}, \quad (144)$$

where  $e$  is the earth's eccentricity and  $z_{\text{obs}}$  (m) is the elevation of the observer, corresponding to the pixel's center elevation  $z$ . The geodetic observer and satellite coordinates are then transformed into earth-centered earth-fixed (ECEF) coordinates including their vector norms:

$$X_{\text{obs}} = H_{\text{obs}} \cos \phi'_{\text{obs}} \cos \lambda_{\text{obs}} \quad (145)$$

$$Y_{\text{obs}} = H_{\text{obs}} \cos \phi'_{\text{obs}} \sin \lambda_{\text{obs}} \quad (146)$$

$$Z_{\text{obs}} = H_{\text{obs}} \sin \phi'_{\text{obs}} \quad (147)$$

$$N_{\text{obs}} = \sqrt{X_{\text{obs}}^2 + Y_{\text{obs}}^2 + Z_{\text{obs}}^2} \quad (148)$$

$$X_{\text{sat}} = H_{\text{sat}} \cos \phi'_{\text{sat}} \cos \lambda_{\text{sat}} \quad (149)$$

$$Y_{\text{sat}} = H_{\text{sat}} \cos \phi'_{\text{sat}} \sin \lambda_{\text{sat}} \quad (150)$$

$$Z_{\text{sat}} = H_{\text{sat}} \sin \phi'_{\text{sat}} \quad (151)$$

$$N_{\text{sat}} = \sqrt{X_{\text{sat}}^2 + Y_{\text{sat}}^2 + Z_{\text{sat}}^2}. \quad (152)$$

For the observer location, the ECEF coordinates need to first be transformed to the components of the vector which is normal on the to the surface of the earth's geoid:

$$X'_{\text{obs}} = Z_{\text{obs}} \frac{\cos \lambda_{\text{obs}}}{\tan \phi_{\text{obs}}} \quad (153)$$

$$Y'_{\text{obs}} = Z_{\text{obs}} \frac{\sin \lambda_{\text{obs}}}{\tan \phi_{\text{obs}}} \quad (154)$$

$$Z'_{\text{obs}} = Z_{\text{obs}} \quad (155)$$

$$N'_{\text{obs}} = \sqrt{(X'_{\text{obs}})^2 + (Y'_{\text{obs}})^2 + (Z'_{\text{obs}})^2}, \quad (156)$$

and

$$N_{\text{sat-obs}} = \sqrt{(X_{\text{sat}} - X_{\text{obs}})^2 + (Y_{\text{sat}} - Y_{\text{obs}})^2 + (Z_{\text{sat}} - Z_{\text{obs}})^2}. \quad (157)$$

The geocentric angle between the direction of the satellite and the observer is:

$$\delta_{\text{sat-obs}} = \arccos \left( \frac{X_{\text{sat}} X_{\text{obs}} + Y_{\text{sat}} Y_{\text{obs}} + Z_{\text{sat}} - Z_{\text{obs}}}{N_{\text{sat}} H_{\text{obs}}} \right) \quad (158)$$

The satellite view zenith angle can then be calculated as:

$$\theta_v = \arccos\left(\frac{X_{\text{obs}}(X_{\text{sat}} - X_{\text{obs}}) + Y_{\text{obs}}(Y_{\text{sat}} - Y_{\text{obs}}) + Z_{\text{obs}}(Z_{\text{sat}} - Z_{\text{obs}})}{H_{\text{obs}}N_{\text{sat-obs}}}\right) \quad (159)$$

In order to determine the view azimuth angle the vector V90 in the meridional plane perpendicular to the vertical of the observation point and pointing to the north pole is calculated:

$$X_{V90} = -X'_{\text{obs}}Z'_{\text{obs}} \quad (160)$$

$$Y_{V90} = -Y'_{\text{obs}}Z'_{\text{obs}} \quad (161)$$

$$Z_{V90} = (X'_{\text{obs}})^2 + (Y'_{\text{obs}})^2 \quad (162)$$

$$N_{V90} = \sqrt{X_{V90}^2 + Y_{V90}^2 + Z_{V90}^2} \quad (163)$$

The vector V0 orthogonal to V90 and the observation vector is formed (3 axis right-hand system with V0 pointing eastwards):

$$X_{V0} = Y_{V90}Z'_{\text{obs}} - Z_{V90}Y'_{\text{obs}} \quad (164)$$

$$Y_{V0} = Z_{V90}X'_{\text{obs}} - X_{V90}Z'_{\text{obs}} \quad (165)$$

$$Z_{V0} = X_{V90}Y'_{\text{obs}} - Y_{V90}X'_{\text{obs}} \quad (166)$$

$$N_{V0} = \sqrt{X_{V0}^2 + Y_{V0}^2 + Z_{V0}^2} \quad (167)$$

The vector SS pointing to the satellite from the observation point is calculated:

$$X_{SS} = X_{\text{sat}} - X_{\text{obs}} \quad (168)$$

$$Y_{SS} = Y_{\text{sat}} - Y_{\text{obs}} \quad (169)$$

$$Z_{SS} = Z_{\text{sat}} - Z_{\text{obs}} \quad (170)$$

$$N_{SS} = \sqrt{X_{SS}^2 + Y_{SS}^2 + Z_{SS}^2} \quad (171)$$

The vector on the tangent plane to the observation point and pointing to the satellite is calculated:

$$(Y'_{\text{obs}}Z_{SS} - Z'_{\text{obs}}Y_{SS}) \quad (172)$$

$$(Z'_{\text{obs}}X_{SS} - X'_{\text{obs}}Z_{SS}) \quad (173)$$

$$(X'_{\text{obs}}Y_{SS} - Y'_{\text{obs}}X_{SS}) \quad (174)$$

$$(175)$$

$$X_P = Z'_{\text{obs}}(Z'_{\text{obs}}X_{\text{SS}} - X'_{\text{obs}}Z_{\text{SS}}) - Y'_{\text{obs}}(X'_{\text{obs}}Y_{\text{SS}} - Y'_{\text{obs}}X_{\text{SS}}) \quad (176)$$

$$Y_P = X'_{\text{obs}}(X'_{\text{obs}}Y_{\text{SS}} - Y'_{\text{obs}}X_{\text{SS}}) - Z'_{\text{obs}}(Y'_{\text{obs}}Z_{\text{SS}} - Z'_{\text{obs}}Y_{\text{SS}}) \quad (177)$$

$$Z_P = Y'_{\text{obs}}(Y'_{\text{obs}}Z_{\text{SS}} - Z'_{\text{obs}}Y_{\text{SS}}) - X'_{\text{obs}}(Z'_{\text{obs}}X_{\text{SS}} - X'_{\text{obs}}Z_{\text{SS}}) \quad (178)$$

$$N_P = \sqrt{X_P^2 + Y_P^2 + Z_P^2}. \quad (179)$$

The view azimuth angle is calculated as:

$$\phi_v = \begin{cases} \alpha & \text{if } \beta \leq 90^\circ; \\ 360^\circ - \alpha & \text{if } \beta > 90^\circ \end{cases}, \quad (180)$$

where

$$\alpha = \arccos\left(\frac{X_{V90}X_P + Y_{V90}Y_P + Z_{V90}Z_P}{N_{V90}N_P}\right) \quad (181)$$

$$\beta = \arccos\left(\frac{X_{V0}X_P + Y_{V0}Y_P + Z_{V0}Z_P}{N_{V0}N_P}\right). \quad (182)$$

The above formulation has various limitations (polar areas, satellite vector pointing in the same direction as the observer vector) which have to be handled during the actual implementation. *Gieske et al. (2005)* point out to inaccuracies in the above formulation and suggest a simpler approach which should be carefully evaluated as a next step.

## 10 Dynamic Boundary Conditions

### 10.1 Sun-Earth Distance

The relative sun-earth distance in AU is calculated after *World Meteorological Organization (2008)*, Appendix 7D. The formulas are given here for completeness:

$$d_s = 1.00014 - 0.01671 \cos g - 0.00014 \cos 2g \quad (183)$$

$$g = 357.528 + 0.9856003n, \text{ where } 0 \leq g < 360, \quad (184)$$

and where  $n = \text{JD} - 2451545.0$  and JD is the Julian Day (fractional day number since January 1, 4713 BC 12:00 UTC).

### 10.2 Sun View Angles

Sun zenith  $\theta_s$  and azimuth  $\phi_s$  angles are calculated for each MSG SEVIRI pixel and at each time step. For a given date, the equation of time ET (minutes) and the earth's declination with respect to the orbital plane  $\delta_s$  (degrees) can be approximated by:

$$\text{ET} = e_1(e_2 + e_3 \cos \gamma - e_4 \sin \gamma - e_5 \cos 2\gamma - e_6 \sin 2\gamma) \quad (185)$$

$$\delta_s = d_1 - d_2 \cos \gamma + d_3 \sin \gamma - d_4 \cos 2\gamma + d_5 \sin 2\gamma - d_6 \cos 3\gamma + d_7 \sin 3\gamma \quad (186)$$

where  $\gamma = 2\pi D/365$  is the fractional year (radians) for day of year  $D$  and the fourier series coefficients  $e$  and  $d$  are given in Table 7. The true solar time (TST, minutes) can be calculated from the universal time coordinate (UTC, minutes) for longitude  $\lambda$ :

$$\text{TST} = \text{UTC} + \text{ET} + 4\lambda \quad (187)$$

The hour angle HA (radians) is then:

$$\text{HA} = \frac{2\pi}{180} \left( \frac{\text{TST}}{4} - 180 \right) \quad (188)$$

**Table 7:** Empirical coefficients needed to calculate the equation of time and declination

No.	$e$	$d$
1	229.18	0.006918
2	0.000075	0.399912
3	0.001868	0.070257
4	0.032077	0.006758
5	0.014615	0.000907
6	0.040849	0.002697
7	-	0.00148

which allows the calculation of the sun zenith angle  $\theta_s$ :

$$\theta_s = \arccos(\min(\max(\sin \phi \sin \delta_s + \cos \phi \cos \delta_s \cos HA, -1), 1)) \quad (189)$$

and the sun azimuth angle  $\phi_s$ :

$$\phi_s = \arccos\left(\min(\max\left(\frac{-(\sin \phi \cos \theta_s - \sin \delta_s)}{\cos \phi \sin \theta_s}, -1\right), 1)\right) \quad (190)$$

where  $\phi_s$  with TST > 720 minutes are converted from the range  $-180^\circ \dots 0^\circ$  to  $180^\circ \dots 360^\circ$ . This conversion is required because  $\phi_s$  is defined clock-wise with  $0^\circ$  pointing towards North,  $90^\circ$  East,  $180^\circ$  South and  $270^\circ$  West.

### 10.3 Angle between the sun and normal to the plane

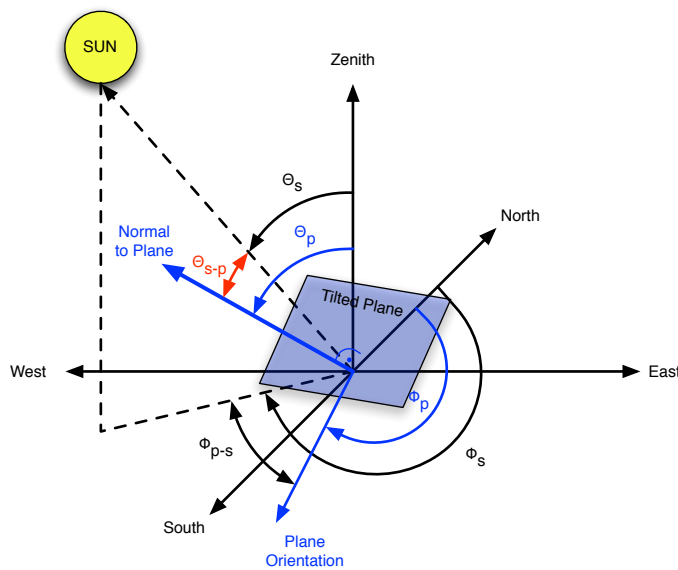


**Figure 8:** Illustration of the geometrical relationships between the sun position and a tilted plane from an observer viewpoint on the earth's surface.

Tilted planes can be included in “HeliMont” by specifying a plane orientation and elevation (e.g. for calculating the solar radiation incident on solar modules or roofs) or by using the pixel-wise local terrain aspect and slope calculated from the digital elevation model (e.g. for calculating the solar radiation incident on agricultural fields).

For a tilted plane with tilt angle  $\theta_p$  and azimuth angle  $\phi_p$  the angle between the sun direction and normal to the plane  $\theta_{s-p}$  (Figure 8) is calculated,

$$\theta_{s-p} = \arccos(\cos(\theta_p) \cos(\theta_s) + \sin(\theta_p) \sin(\theta_s) \cos(\phi_p - \phi_s)). \quad (191)$$

## 10.4 Sun-Satellite Angles

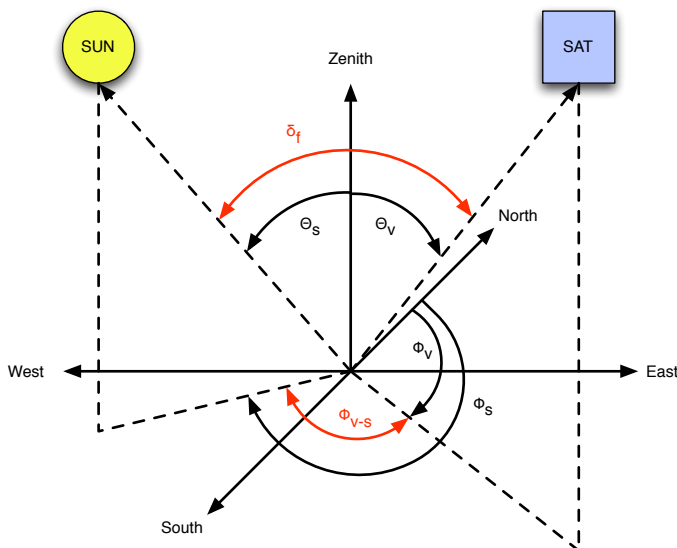


**Figure 9:** Illustration of the geometrical relationships between the sun position and the satellite position from an observer viewpoint on the earth's surface.

Radiative transfer model applications often require the specification of the relative sun – satellite view geometry. The relative sun – satellite azimuth angle is calculated as follows:

$$\phi_{v-s} = \phi_v - \phi_s, \quad (192)$$

where  $\phi_{v-s}$  is defined as  $0^\circ$  for the sun and the satellite located in the same direction and  $180^\circ$  for the sun and the satellite located opposite from each other. The radiative transfer model libRadtran for instance assumes  $\phi_{v-s}$  to be defined as  $0^\circ$  for the sun and the the satellite located opposite from each other. The definition of the relative sun – satellite azimuth angle can thus differ by  $180^\circ$ . While the satellite sensor azimuth angle is always defined with a clockwise rotation and  $0^\circ$  pointing North, the sun azimuth angle can also be defined as  $0^\circ$  pointing South with a clockwise (such as in libRadtran) or anti-clockwise rotation. In this document we define all azimuth angles as  $0^\circ$  pointing North with a clockwise rotation (Figure 9).

The sun–satellite scattering angle is the relative angle enclosed by the two vectors pointing to the sun

and the satellite. Here again, two definitions can be found in literature, and they are both used depending on the application. The backward scattering angle  $\delta_b$  gives the amount of backward scattering and is often used in bidirectional reflectance calculations. It is at its maximum when the satellite is located in the direction of the sun:

$$\delta_b = \arccos(\cos \theta_v \cos \theta_s + \sin \theta_v \sin \theta_s \cos \phi_{v-s}). \quad (193)$$

The forward scattering angle  $\delta_f$  gives the amount of forward scattering and is often used in specular reflection calculations (e.g. sun glint). It is at its maximum when the satellite is located opposite of the sun:

$$\delta_f = \arccos(\cos \theta_v \cos \theta_s - \sin \theta_v \sin \theta_s \cos \phi_{v-s}). \quad (194)$$

## 11 Geographic Projections

### 11.1 Meteosat First Generation (forward)

The forward projection formulas for the Meteosat First Generation satellites as published by *EUMETSAT* (2011) are used.

### 11.2 Meteosat First Generation (inverse)

The inverse projection formulas for the Meteosat First Generation satellites as published by *EUMETSAT* (2011) are used.

### 11.3 Meteosat Second Generation (forward)

The forward projection formulas for geostationary satellites as published by *Coordination Group for Meteorological Satellites* (1999) are used.

### 11.4 Meteosat Second Generation (inverse)

The inverse projection formulas for geostationary satellites as published by *Coordination Group for Meteorological Satellites* (1999) are used.

### 11.5 Swiss Orthographic (forward)

The approximate forward reprojection formula published by *Swisstopo* (2005) are used. They are appropriate for up to 1 m accuracy.



## 11.6 Swiss Orthographic (inverse)

The approximate inverse reprojection formula published by *Swisstopo* (2005) are used. They are appropriate for up to 1 m accuracy.

## 11.7 Orthographic (forward)

The orthographic projection is a commonly used map projection in cartography. It is used here to calculate north-south or west-east distances for each pixel to its neighboring pixel on either the irregular satellite grid or on the regular longitude/latitude grid. The equations to project latitude  $\phi$  ( $^{\circ}$ N; radians) and longitude  $\lambda$  ( $^{\circ}$ E; radians) onto the x and y northing [m] and easting [m] coordinates of the tangent plane are:

$$x = R \cos \phi \sin(\lambda - \lambda_0) \quad (195)$$

$$y = R [\cos \phi_0 \sin \phi - \sin \phi_0 \cos \phi \cos(\lambda - \lambda_0)], \quad (196)$$

where  $\phi_0$  and  $\lambda_0$  are the center latitude and longitude of the geographic domain [radians] and  $R$  is the radius [m] of the spherical earth. Orthographic projection of the ellipsoidal earth is not implemented. The potential gain in accuracy of such a transformation would not be justified for the application in "HeliMont". Areas outside of the projectable area, such as areas on the other side of the hemisphere, should not be projected. They are excluded by assuring that  $\cos c = \sin \phi_0 \sin \phi + \cos \phi_0 \cos \phi \cos(\lambda - \lambda_0) \geq 0$ , where  $c$  is the distance of  $\phi$  and  $\lambda$  to the projection center (thus, negative distances are not allowed).

## 11.8 Orthographic (inverse)

The inverse orthographic projection is required to calculate longitude and latitude for orthographic coordinates, as for instance needed when calculating bilinear interpolation indices for the orthographic forward projection:

$$\phi = \arcsin \left[ \cos c \sin \phi_0 + \frac{y \sin c \cos \phi_0}{\rho} \right] \quad (197)$$

$$\lambda = \lambda_0 + \arctan \left[ \frac{x \sin c}{\rho \cos \phi_0 \cos c - y \sin \phi_0 \sin c} \right], \quad (198)$$

where

$$\rho = \sqrt{x^2 + y^2} \quad (199)$$

$$c = \arcsin(\rho/R), \quad (200)$$

and where the `arctan` formula needs to separate all four quadrants, thus the Fortran or C `atan2(x,y)` function with two arguments has to be used.

## 11.9 Rotated Pole (forward)

Rotated pole coordinates are often used in regional climate models like the COntortium for Small-scale MOdeling (COSMO) model. The following formulas are used to project latitude  $\phi$  ( $^{\circ}$ N; radians) and longitude  $\lambda$  ( $^{\circ}$ E; radians) onto rotated latitude  $\phi_r$  ( $^{\circ}$ N; radians) and rotated longitude  $\lambda_r$  ( $^{\circ}$ E; radians):

$$\phi_r = \arcsin [\cos \phi_p \cos \phi \cos(\lambda - \lambda_p) + \sin \phi_p \sin \phi] \quad (201)$$

$$\lambda_r = \arctan \left[ \frac{-\sin(\lambda - \lambda_p) \cos \phi}{-\sin \phi_p \cos \phi \cos(\lambda - \lambda_p) + \cos \phi_p \sin \phi} \right], \quad (202)$$

where  $\phi_p$  and  $\lambda_p$  are the rotated pole latitude and longitude. The `arctan` formula needs to separate all four quadrants, thus the Fortran or C `atan2(x,y)` function with two arguments has to be used.

## 11.10 Rotated Pole (inverse)

The inverse formula is for instance needed to generate reverse indices for bilinear interpolation of regular to rotated pole coordinates:

$$\phi = \arcsin [\cos \phi_p \cos \phi \cos \lambda + \sin \phi_p \sin \phi] \quad (203)$$

$$\lambda = \arctan \left[ \frac{\sin \lambda_p (-\sin \phi_p \cos \lambda \cos \phi + \cos \phi_p \sin \phi) - \cos \lambda_p \sin \lambda \cos \phi}{\cos \lambda_p (-\sin \phi_p \cos \lambda \cos \phi + \cos \phi_p \sin \phi) + \sin \lambda_p \sin \lambda \cos \phi} \right], \quad (204)$$

where the `arctan` formula needs to separate all four quadrants, thus the Fortran or C `atan2(x,y)` function with two arguments has to be used.

## 11.11 Reprojection

Above forward and inverse projection formulas are part of a reprojection toolset specifically created for the “HelioMont” processing. The reprojection can be carried out from any regular input to any regular output grid. For instance, the regular line / column grid of the geostationary satellite projection can be projected onto the rotated pole longitude / latitude grid of the COSMO model by a single call to a wrapper function which carries out the following reprojection steps:

1. reprojection of input grid  $x_i$  and  $y_i$  to input grid  $\lambda_i$  and  $\phi_i$  coordinates (inverse projection)
2. reprojection of input grid  $\lambda_i$  and  $\phi_i$  to output  $x_o$  and  $y_o$  coordinates (forward projection)
3. reprojection of output grid  $x_o$  and  $y_o$  to output grid  $\lambda_i$  and  $\phi_i$  coordinates (inverse projection)

4. reprojection of output grid  $\lambda_i$  and  $\phi_i$  coordinates to input  $x_i$  and  $y_i$  coordinates (forward projection)

If input or output coordinates are already in the geographic projection, either step 1 or 3 are not needed. Delaunay triangles and a histogram of the number and locations of input grid points covering each grid cell of the regular output grid are then calculated with the irregular grid from step 2. Reverse indices for nearest neighbor sampling are then calculated, relating each grid point of the output grid onto its nearest location in the input grid, based on step 4. Triangles, the histogram and the indices are cached for subsequent reprojection calls within the same processing.

Depending on the type of variable a different reprojection method is chosen. For continuous fields, triangulation is chosen. For discrete data (such as the cloud mask or land cover data) predominant pixel sampling is chosen, where the median of the input grid values covering the output grid cell is derived by use of the previously allocated histogram for each output grid cell. If the output grid is of much finer resolution than the input grid, nearest-neighbor sampling is used to fill output grid cells where the histogram contains empty bins with no covering input grid cells.

## 12 Geometric Projections

### 12.1 Orthorectification

Meteosat data with a pixel size of less than 2-3 km has to be orthorectified because the slant viewing geometry of non-nadir Meteosat pixels generates artificial geometric shifts in terrain. Currently,  $N$ ,  $N_{\text{vis}}$ ,  $N_{\text{ir}}$ ,  $\rho$  and  $\rho_{\text{cf}}$  are orthorectified since they depend on the HRV channel. The HRV channel has a pixel resolution of 1-2 km, which is in the same order of magnitude as the mean terrain elevation of some Meteosat pixels in the Alps. Orthorectification of the “raw” Meteosat grid onto a orthorectified Meteosat grid can be achieved by using a surface elevation dataset projected on the orthorectified Meteosat grid  $z_{\text{ortho}}$  (see Section 9.2 ) to generate shifted locations for each Meteosat pixel for reprojecting the “raw” Meteosat grid into the orthorectified Meteosat grid.

Firstly, the orthographic shift  $\Delta x$  (m) and  $\Delta y$  (m) for each Meteosat pixel is calculated as:

$$\Delta r = \frac{z_{\text{ortho}}}{\tan(90 - \theta_v)} \quad (205)$$

$$\Delta x = \Delta r \sin(\phi_v - 180) \quad (206)$$

$$\Delta y = \Delta r \cos(\phi_v - 180). \quad (207)$$

Orthographic shifts are translated back into shifts in geographic coordinates:

$$\Delta \lambda_{\text{ortho}} = \frac{360 \Delta x}{2\pi R \cos(\phi)} \quad (208)$$

$$\Delta \phi_{\text{ortho}} = \frac{360 \Delta y}{2\pi R}, \quad (209)$$

where  $R$  (m) is the radius of the earth. These shifts are added to the geographic coordinates of Meteosat pixels:

$$\lambda_{\text{ortho}} = \lambda_{\text{col,lin}} + \Delta \lambda_{\text{ortho}} \quad (210)$$

$$\phi_{\text{ortho}} = \phi_{\text{col,lin}} + \Delta \phi_{\text{ortho}}. \quad (211)$$

For each Meteosat pixel a new shifted column and line pair  $\text{col}_{\text{ortho}}$  and  $\text{lin}_{\text{ortho}}$  is calculated by use of the forward projection routines for Meteosat given in Section 11. With these shifted column and lines bilinear interpolation for floating point data or NN re-sampling (for boolean or integer data) is used to

transform the “raw” Meteosat grid into the orthorectified Meteosat grid. The orthorectification shift for a location at 2000 m altitude at a latitude of 45° N corresponds to around 1–2 HRV pixels.

In general, clear sky compositing and cloud masking is carried out on the “raw” non-orthorectified grid. Only specific fields, such as the cloud index or the visible clear sky composite, are orthorectified in order to guarantee a better match with surface observations. Inverse orthorectification is needed for projecting orthorectified features, such as clear sky composited surface fields, back onto the “raw” non-orthorectified grid. In this case the irregular “raw” Meteosat grid given by  $col_{ortho}$  and  $lin_{ortho}$  is transformed into a regular grid by use of triangulation.

## 12.2 Cloud Height

Cloud top height  $H_c$  (m) is calculated according to *Khlopenkov and Trishchenko (2007)*. By assuming a constant atmospheric lapse rate  $\lambda_a = 0.006 \text{ K m}^{-1}$ , the cloud top height for opaque clouds is calculated as:

$$H_c = \frac{T_{10.8} - T_{cf}}{\lambda_a} \frac{1}{1 - 0.039C_{score}} \quad (212)$$

where  $T_{10.8}$  is the all sky brightness temperature of the 10.8  $\mu\text{m}$  channel and  $T_{cf}$  is the clear sky brightness temperature from the clear sky compositing of Section 6.2.  $T_{cf}$  is only a rough approximation for the surface air temperature required for this calculation. Ideally  $T_{cf}$  would also have to be corrected for atmospheric water vapor and cloud forcing. However, in mountainous terrain  $T_{cf}$  can be a better constraint than the air temperature field from a large-scale numerical weather model.

For semi-transparent clouds the brightness temperature contains a mixture of surface and cloud information which leads to an underestimation of the cloud top height. *Stephens (1994)* suggest a correction by use of the different thermal emissivities of the earth’s surface compared to ice clouds which continuously decreases for semi-transparent and fully vanishes opaque clouds. Thus the cirrus score  $C_{score}$  of the cloud mask (Section 5 ) is used to “raise” the cloud top height for semi-transparent clouds, where  $C_{score}$  is limited to values in the range of 0 . . . 18.

Cloud height is given relative to the orographic height (the mean orographic height of the 10.8  $\mu\text{m}$  channel resolution). Cloud height is set to 0 m for clear sky pixels (see the cloud mask in Section 5). For a missing 12.0  $\mu\text{m}$  channel  $C_{score}$  is set to 0. In turn the cloud top height of semi-transparent high clouds will be consistently underestimated.

## 13 Climatological Compositing

### 13.1 Daily, Monthly and Yearly Mean Values

Climatological compositing is performed by first calculating the daily mean values  $X_d$ .  $X$  can be global  $G$ , direct  $B$ , diffuse  $D$  radiation or direct normal  $DNI$  irradiance. From the daily mean values the monthly mean  $X_m$  and yearly mean  $X_y$  values are calculated. Daily mean values are derived from instantaneous values as follows *Müller et al.* (2009):

$$X_d = X_{cf,d} \frac{\sum_{i=1}^{n_v} X_i}{\sum_{i=1}^{n_v} X_{cf,i}}, \quad (213)$$

where  $X_{cf,d}$  is the daily mean of the clear sky global radiation flux (alternatively, the respective component of the clear sky radiation flux may be used),  $X_i$  and  $X_{cf,i}$  are the slot-wise fluxes for  $n_v$  valid time slots per day. This calculation reconstructs the daily mean radiation flux even when missing data is present (such as during night or during satellite maintenance and manoeuvres), by weighting the remaining data with the diurnal cycle of clear sky solar radiation and cloudiness.  $X_d$  is calculated when the clear sky radiation of the available time slots covers at least 75% of the total diurnal clear sky radiation.

### 13.2 Spatial Downscaling

The climatological compositing includes the option for spatial downscaling. Thus, a previously calculated slot-wise time series on the original satellite resolution may be composited on a much finer spatial grid by accounting for local terrain effect. This post-processing option is useful since it does not require the complex satellite data pre-processing, cloud masking and clear sky compositing anymore. It however requires the re-calculation of the radiation by use of the new topographic parameters such as horizon and sky view (see Section 8.9). The radiation post-processing also includes the option for user-specified surface tilt and aspect angles and it can occur on any of the geographic projection defined in Section 11.

### 13.3 Radiation on a Tilted Plane from Monthly Mean Data

Monthly mean surface solar radiation on a tilted plane should be calculated from sub-hourly horizontal global and direct radiation fluxes as described in Section 8.9. However, it can be approximated from

monthly mean fluxes of global and direct radiation as described here. This procedure is useful for users of gridded monthly surface solar radiation data which do not have access to the underlying sub-hourly data. The monthly mean global  $G_m$  and direct  $B_m$  radiation fluxes are re-distributed to a diurnal cycle, followed by geometrical transformations from the horizontal to the tilted plane.

The re-distribution requires knowledge of a mean monthly diurnal cycle of clear sky global and direct beam radiation which can be calculated by use of a radiative transfer model as described in Section 7. This approximate calculation assumes that cloudiness is evenly distributed during the day and that cloudiness has no effect on the diffuse fraction of global radiation. An even simpler approach is to use the mean monthly diurnal cycle of the sun zenith angle after Section 10.2 for redistributing monthly mean values across each hour of the day.

The following static and time-dependent boundary conditions need to be known:

- the horizon  $H_t$  and sky view factor  $f_{\text{sky}}$  (Section 9.4 and Section 9.5)
- the sky view factor of the tilted plane  $f_{\text{sky,p}}$  (Section 9.5)
- the hourly sun zenith angle  $\theta_{s,h}$  and sun azimuth angle  $\phi_{s,h}$  for the mean day of the month (Section 10.2)
- the hourly terrain shadow  $S_{t,h}$  for the mean day of the month (Section 8.6)
- the monthly mean surface albedo  $\alpha_s$  (Section 6.4)
- optional: the hourly clear sky (cloud free “cf”) global  $G_{\text{cf,h}}$  and direct  $B_{\text{cf,h}}$  radiation fluxes for the mean day of the month (Section 7)

Hourly direct and diffuse radiation is approximated from the monthly mean global and direct radiation and the hourly clear sky global and direct radiation data as follows:

$$B_h = B_m \frac{n_h B_{\text{cf,h}} (1 - S_{t,h})}{\sum_{i=1}^{n_h} B_{\text{cf,i}} (1 - S_{t,i})} \quad (214)$$

$$D_h = G_m \frac{n_h G_{\text{cf,h}}}{\sum_{i=1}^{n_h} G_{\text{cf,i}}} - B_m \frac{n_h B_{\text{cf,h}}}{\sum_{i=1}^{n_h} B_{\text{cf,i}}}, \quad (215)$$

where  $n_h = 24$  are the number of hours per day. It is assumed that  $G_m$  and  $B_m$  already account for terrain shadow effects. The term  $1 - S_{t,h}$  weights the influence of terrain shadow on the hourly direct beam radiation. The calculation can also be performed from non-terrain-shadowed  $G_m$  and  $B_m$ . In this case the term  $1 - S_{t,h}$  can be omitted.

If hourly clear sky global and direct radiation fluxes are not available, the sun zenith angle can be used as a surrogate:

$$B_h = B_m \frac{n_h \max(\cos \theta_{s,h}, 0) (1 - S_{t,h})}{\sum_{i=1}^{n_h} \max(\cos \theta_{s,i}, 0) (1 - S_{t,i})} \quad (216)$$

$$D_h = G_m \frac{n_h \max(\cos \theta_{s,h}, 0)}{\sum_{i=1}^{n_h} \max(\cos \theta_{s,i}, 0)} - B_m \frac{n_h \max(\cos \theta_{s,h}, 0)}{\sum_{i=1}^{n_h} \max(\cos \theta_{s,i}, 0)}. \quad (217)$$

This simplification assumes that the diurnal course of both direct and diffuse radiation are linearly related to the sun zenith angle, which is a valid approximation for direct but not for diffuse radiation. Empirical parameterizations of the diffuse fraction of solar irradiance, such as described in *Skartveit*

and Olseth (1987), could be used to redistribute monthly mean diffuse radiation to the diurnal cycle in a more realistic way.

If the monthly radiation fluxes  $B_m$  and  $G_m$  do not already include terrain shadow effects, terrain shadow has to be added to hourly direct beam and diffuse radiation fluxes  $B_{h,t}$  and  $D_{h,t}$  after Section 8.10.  $B_{h,p}$  and  $D_{h,p}$  can next be calculated for a tilted plane after Section 8.11. Global radiation  $G_{h,p}$  on the tilted plane is finally derived after Section 8.12. Monthly mean  $G_{m,p}$  can be derived from hourly values by simply taking the mean over  $n_h$  values.

The rough assumptions behind these calculations using monthly mean data as input increase the uncertainty of the resulting monthly mean radiation fluxes on the tilted plane when compared to the calculation of with sub-hourly input data. The validity of the approximation strongly depends on the day-to-day variability and also on the diurnal course of cloudiness. It also depends on the magnitude of the chosen plane tilt and azimuth angle. A sensitivity test for the ASRB / BSRN site in Payerne was performed for 2005 comparing the calculation with monthly mean input data compared to the exact (sub-hourly) calculation. For a  $30^\circ$  plane tilt and  $120^\circ$  plane azimuth the mean absolute bias (mab) is  $0.5 \text{ W m}^{-2}$  or  $3 \text{ W m}^{-2}$  when using clear sky radiation fluxes for diurnal weighting. The mab increases to  $3 \text{ W m}^{-2}$  when using the sun zenith angle for diurnal weighting. For a  $60^\circ$  plane tilt and  $120^\circ$  plane azimuth the mab is  $2 \text{ W m}^{-2}$  when using clear sky radiation fluxes for diurnal weighting. It increases to  $8 \text{ W m}^{-2}$  when using the sun zenith angle for diurnal weighting. These uncertainties increase for locations with more complex terrain.



## 14 Miscellaneous Algorithms

### 14.1 Temporal Variance

The temporal variance for each pixel of a two-dimensional field of size  $n_x \times n_y$  is calculated by use of a moving window, also known as First-in-First-out (FIFO), approach. The FIFO starts up with missing values. At every time step old data are pushed out of the moving window and new ones are pushed in. The spin-up required to fill the moving window is thus equal to the length of the temporal variance. Temporal variances are calculated during climatological processing and in near-realtime applications. In the latter case the state of the FIFO is conserved in restart files.

### 14.2 Spatial Variance

The spatial variance of a two-dimensional field of size  $n_x \times n_y$  is defined here as the variance of all surrounding pixels within a circular distance of radius  $r$  of a given pixel with location  $x, y$ :

$$\text{VAR}(X_{x,y}) = \frac{1}{n} \sum_{x \pm \Delta x, y \pm \Delta y} (X_{x,y} - \bar{X})^2, \text{ where } \sqrt{\Delta x^2 + \Delta y^2} < r, \quad (218)$$

It is computationally not efficient to run the above calculation pixel by pixel. For the calculation of the spatial variance in time-dependent spatial fields (such as in the Meteosat cloud masking) normalized spatial convolution can be used in a two step approach. First, the spatial mean is calculated:

$$\bar{X}_{x,y} = \frac{1}{n_k} \sum_{i=0, j=0}^{k-1, l-1} X_{s,t} K_{i,j} \quad (219)$$

$$s = \min(\max(x + i - k/2, 0), n_x - 1) \quad (220)$$

$$t = \min(\max(y + j - l/2, 0), n_y - 1) \quad (221)$$

$$n_k = \sum (K > 0), \quad (222)$$

where  $n_k$  is the normalization of the spatial convolution and where  $K$  is a two-dimensional kernel with size  $2\Delta x + 1 \times 2\Delta y + 1$ :

$$K_{i,j} = \begin{cases} 1 & \text{if } \sqrt{(i + \Delta x)^2 + (j + \Delta y)^2} < r; \\ 0 & \text{if } \sqrt{(i + \Delta x)^2 + (j + \Delta y)^2} \geq r \end{cases}; \quad (223)$$

The spatial mean of  $X^2$  is calculated accordingly. The spatial variance is then calculated by:

$$\text{VAR}(X_{x,y}) = \bar{X}^2_{x,y} - (\bar{X}_{x,y})^2. \quad (224)$$

Missing data and areas where the moving kernel extends beyond  $(0; n_x - 1)$  and  $(0; n_y - 1)$  are not counted in the convolution.

## 15 Validation

### 15.1 Validation with Alpine Surface Radiation Budget network data

The Alpine Surface Radiation Budget (ASRB) network is a set of 10 selected and high quality radiation measurement stations in the Swiss alps (*Philipona et al. (1996); Marty et al. (2002)*, [http://www.meteoschweiz.admin.ch/web/en/research/completed\\_projects/asrb.html](http://www.meteoschweiz.admin.ch/web/en/research/completed_projects/asrb.html)). ASRB stations are co-located with SwissMetNet stations and are distributed between 370 and 3580 m a.s.l. over an area of about 200 by 200 km<sup>2</sup>. ASRB sites operated between 1994 to 2010 and are selected as the main validation source to check the performance of “HelioMont” over mountainous terrain.

On the inter-annual time scale mean absolute bias and mean bias error are below  $\pm 5 \text{ W m}^{-2}$  (Table 8), except at Jungfrauoch, where the local horizon has a substantial influence even on the yearly mean solar irradiance. This particular station demonstrates one of the key problems which can arise when comparing station to satellite data. Correlation between yearly averages ranges from  $r=0.6\text{--}0.9$  for the majority of stations. These statistics are likely to improve once a longer time series can be compared. At SLF-Versuchsfeld and Weissfluhjoch for instance, the inter-annual variability in the 7 considered years is small in both station measurements and satellite data, which yields a low negative correlation. However, both the ground and satellite observed yearly mean values are consistent with a low mean bias error (mbe) of below  $2 \text{ W m}^{-2}$ .

Mean bias errors are independent of aggregation. The monthly and daily mbe values (Table 9 and Table 10) thus correspond to the ones for yearly (inter-annual) time scale. However, mean absolute bias (mab) increases with increasing time resolution. It ranges between  $5\text{--}10 \text{ W m}^{-2}$  for monthly and  $10\text{--}20 \text{ W m}^{-2}$  for daily values where mountainous stations have around twice the mab compared to the lowland stations Locarno-Monti and Payerne.

Mean bias errors are slightly higher for hourly data compared to daily, monthly and inter-annual data since the latter ones are averaged over the night period. Mean absolute biases for hourly data are around  $40 \text{ W m}^{-2}$  for lowland stations and around  $60\text{--}70 \text{ W m}^{-2}$  for mountainous stations (Table 11).

The correlation between ASRB station data and the corresponding MSG data is  $0.97\text{--}0.99$  for monthly,  $0.90\text{--}0.99$  for daily and above 0.9 (except for the Eggishorn station) for hourly data. The high correlation coefficient of hourly, daily and monthly data can be partly attributed to the high dependence of global radiation to the solar zenith angle. In order to determine the actual skill of the algorithm to reproduce the effect of clouds on global radiation, the anomaly correlation (ac) of monthly mean values is also performed. The ac remains above 0.9 except for the stations SLF-Versuchsfeld, Eggishorn and Jungfrauoch. The low ac for Jungfrauoch can be explained by the mismatch of the

**Table 8:** Inter-annual validation of the “Heliomont” Global Radiation with ASRB (2004–2010). n = number of observations, mbe = mean bias error, mab = mean absolute bias, r = Pearson correlation. Values marked with a (\*) have a distinct local horizon influencing station measurements.

Station		“Heliomont”			
No	Name	n	mbe	mab	r
			W m-2	W m-2	-
1	Locarno-Monti	7	-3.12	3.16	0.927
2	Payerne	7	0.30	0.87	0.980
3	Davos	7	1.44	2.39	0.610
4	Cimetta	6	0.17	1.83	0.921
5	Maennlichen	7	-1.31	2.11	0.850
6	SLF-Versuchsfeld	7	-0.79	3.41	-0.259
7	Weissfluhjoch	7	-4.28	4.28	-0.230
8	Eggishorn	7	2.70	3.13	0.967
9	Gornergrat	7	0.51	1.67	0.732
10	Jungfrauoch	6	26.33*	26.33*	0.972*

**Table 9:** Monthly validation of the “Heliomont” Global Radiation with ASRB (2004–2010). n = number of observations, mbe = mean bias error, mab = mean absolute bias, r = Pearson correlation, ac = correlation of anomalies. Values marked with a (\*) have a distinct local horizon influencing station measurements.

Station		Heliomont				
No	Name	n	mbe	mab	r	ac
			W m-2	W m-2	-	-
1	Locarno-Monti	84	-2.92	4.99	0.998	0.942
2	Payerne	82	0.25	3.03	0.999	0.977
3	Davos	84	1.36	7.32	0.990	0.920
4	Cimetta	72	0.06	5.49	0.996	0.931
5	Maennlichen	84	-1.64	7.49	0.989	0.855
6	SLF-Versuchsfeld	83	-1.26	9.02	0.975	0.657
7	Weissfluhjoch	84	-4.30	7.85	0.989	0.903
8	Eggishorn	74	1.87	13.99	0.968	0.736
9	Gornergrat	84	0.15	6.35	0.996	0.912
10	Jungfrauoch	57	25.28*	25.28*	0.975*	0.759*

local and the pixel-averaged horizon. However, the rather low ac of 0.66 for SLF-Versuchsfeld and 0.74 for Eggishorn are due to the unrealistic temporal variability of the modeled cloud forcing on global radiation, especially during the summer season. Since daily and hourly anomalies cannot be calculated with the few years available, clear sky normalized correlation coefficients ( $r^*$ ) have been calculated on the daily and hourly time scale (normalization is achieved by dividing all-sky by clear sky

global radiation). On the daily time scale all  $r^*$  values remain above 0.85 except at Eggishorn. On the hourly time scale SLF-Versuchsfeld, Eggishorn and Gornergrat show deficiencies in reproducing the variability of global radiation to clouds. Interestingly the Weissfluhjoch station which is nearby the SLF-Versuchsfeld station performs much better ( $r^*=0.7$  instead of  $r^*=0.4$ ).

**Table 10:** Daily validation of the “HelioMont” Global Radiation with ASRB (2004–2010).  $n$  = number of observations,  $mbe$  = mean bias error,  $mab$  = mean absolute bias,  $r$  = Pearson correlation,  $r^*$  = Pearson correlation of clear sky normalized values. Values marked with a (\*) have a distinct local horizon influencing station measurements.

No	Station		HelioMont			
	Name	$n$	$mbe$ W m-2	$mab$ W m-2	$r$ -	$r^*$ -
1	Locarno-Monti	2476	-2.84	11.54	0.986	0.960
2	Payerne	2424	0.20	9.63	0.991	0.949
3	Davos	2487	1.35	15.69	0.963	0.886
4	Cimetta	2089	0.16	15.51	0.977	0.932
5	Maennlichen	2484	-1.58	19.61	0.960	0.900
6	SLF-Versuchsfeld	2443	-1.31	19.88	0.934	0.826
7	Weissfluhjoch	2488	-4.27	18.98	0.946	0.849
8	Eggishorn	2080	2.09	26.51	0.905	0.786
9	Gornergrat	2487	0.23	18.79	0.960	0.856
10	Jungfrauoch	1533	23.72*	29.47*	0.929*	0.834*

**Table 11:** Hourly validation of the “HelioMont” Global Radiation with ASRB (2004–2010).  $n$  = number of observations,  $mbe$  = mean bias error,  $mab$  = mean absolute bias,  $r$  = Pearson correlation,  $r^*$  = Pearson correlation of clear sky normalized values. Values marked with a (\*) have a distinct local horizon influencing station measurements.

No	Station		HelioMont			
	Name	$n$	$mbe$ W m-2	$mab$ W m-2	$r$ -	$r^*$ -
1	Locarno-Monti	29849	-5.61	40.87	0.970	0.842
2	Payerne	29251	0.65	38.90	0.973	0.787
3	Davos	29865	2.57	56.71	0.942	0.655
4	Cimetta	25334	0.02	50.80	0.954	0.804
5	Maennlichen	30090	-3.76	64.55	0.927	0.721
6	SLF-Versuchsfeld	29597	-2.14	67.13	0.903	0.417
7	Weissfluhjoch	30113	-8.22	60.60	0.924	0.704
8	Eggishorn	25297	4.56	78.18	0.871	0.596
9	Gornergrat	30214	0.38	61.36	0.937	0.559
10	Jungfrauoch	18817	47.09*	74.52*	0.926*	0.659*

## 15.2 Validation with Baseline Surface Radiation Network data

The Baseline Surface Radiation Network (BSRN, *Ohmura et al. (1998)*) is a project of the Radiation Panel from the Global Energy and Water Cycle Experiment GEWEX under the umbrella of the World Climate Research Programme (WCRP). BSRN data is currently maintained by the Alfred Wegener Institute (AWI, <http://www.bsrn.awi.de/en/home/bsrn/>). The data are of very high quality and are of primary importance in supporting the validation of satellite-based surface radiation estimates. BSRN data of 11 stations covering the full Meteosat disk are used here to validate “HelioMont” for temperate, mediterranean and tropical climatic regions. The stations Illorin, Solar Village and Florianopolis have been excluded from the analysis due to either data quality issues or short temporal coverage. The BSRN station Payerne is also included in the analysis even though Payerne has already been covered by the analysis at ASRB stations. The BSRN instrumentation is of higher quality than the ASRB instrumentation. However, both station time series have a very high correlation with less than  $2 \text{ W m}^{-2}$  difference for monthly means.

The performance of “HelioMont” over wide range of climatic regions covered by the BSRN station network is similar (Tables 12, 13, 14 and 15) to the high performance over the Swiss Alps. The only systematic deviations are seen in Lerwick with a systematic negative mbe and corresponding high mab across all time scales and Sede-Boqer with a positive mbe. Lerwick is located on the northern border of the Meteosat disc and thus is observed with a large satellite view zenith angle. The associated effects of a long atmospheric path length possibly include an overestimation of cloudiness and large cloud parallax errors. Similar problems are reported in *Posselt et al. (2012)*. For Sede-Boqer, the problem is likely related to un-detected cirrus clouds or an unrealistic aerosol forcing over the bright desert target region. Possible solutions includes the extension of the infrared cloud index with a cirrus detection score by using for instance a combination of the 10.8 and the 12  $\mu\text{m}$  channels. The comparison at the station Bermuda reveals a large negative mbe on the daily and hourly time step. This problem has been identified and will be corrected. It is related to the sun glint which affects the Bermuda pixel during June - August. The Bermuda pixel is almost entirely a water pixel. Sun glint is falsely been associated to cloud cover when it should be part of the background field (cloud free reflectance).

**Table 12:** Inter-annual comparison of “HeliMont” Global Radiation with BSRN (2004–2011). n = number of observations, mbe = mean bias error, mab = mean absolute bias, r = Pearson correlation.

No	Station Name	n	“HeliMont”		
			mbe W m-2	mab W m-2	r -
1	Bermuda	7	-6.63	6.63	0.993
2	Cabauw	6	-1.40	1.40	0.980
3	Camborne	4	5.11	5.11	0.997
4	Carpentras	7	2.92	3.12	0.893
5	De-Aar	1	1.85	1.85	-
6	Lerwick	4	-6.81	10.43	1.000
7	Lindenberg	3	-6.27	6.27	0.998
8	Palaiseau	3	1.33	3.09	0.999
9	Sede-Boqer	7	15.66	15.66	0.609
10	Tamanrasset	7	2.30	2.30	0.908
11	Toravere	7	-4.59	4.59	0.994

**Table 13:** Monthly validation of “HeliMont” Global Radiation with BSRN (2004–2011). n = number of observations, mbe = mean bias error, mab = mean absolute bias, r = Pearson correlation, ac = correlation of anomalies.

No	Station Name	n	HeliMont			
			mbe W m-2	mab W m-2	r -	ac -
1	Bermuda	74	-6.67	9.52	0.989	0.841
2	Cabauw	71	-1.10	4.17	0.998	0.962
3	Camborne	37	4.65	6.14	0.998	0.954
4	Carpentras	84	3.02	3.70	0.999	0.958
5	De-Aar	12	1.50	3.09	0.999	-
6	Lerwick	25	3.06	7.11	0.992	0.977
7	Lindenberg	36	-6.06	6.97	0.998	0.979
8	Palaiseau	23	1.71	5.41	0.999	0.989
9	Payerne	72	1.72	3.16	0.999	0.975
10	Sede-Boqer	84	14.99	15.01	0.997	0.763
11	Tamanrasset	84	2.25	6.44	0.989	0.944
12	Toravere	81	-3.58	6.17	0.997	0.943

**Table 14:** Daily comparison of “HelioMont” Global Radiation with BSRN (2004–2011). n = number of observations, mbe = mean bias error, mab = mean absolute bias, r = Pearson correlation, r\* = Pearson correlation of clear sky normalized values.

Station			HelioMont			
No	Name	n	mbe	mab	r	r*
			W m-2	W m-2	-	-
1	Bermuda	1906	-6.51	23.83	0.931	0.874
2	Cabauw	1930	-0.96	11.31	0.988	0.937
3	Camborne	966	4.92	16.26	0.973	0.917
4	Carpentras	2435	3.00	8.36	0.994	0.977
5	De-Aar	359	1.46	8.37	0.982	0.954
6	Lerwick	696	3.73	15.36	0.962	0.838
7	Lindenberg	1012	-6.10	12.31	0.986	0.917
8	Palaiseau	620	1.89	11.63	0.990	0.965
9	Payerne	2162	1.71	10.25	0.990	0.946
10	Sede-Boqer	2482	14.94	17.02	0.984	0.869
11	Tamanrasset	2533	2.23	13.66	0.964	0.922
12	Toravere	2145	-3.90	12.80	0.983	0.890

**Table 15:** hourly comparison of “HelioMont” Global Radiation with BSRN (2004–2011). n = number of observations, mbe = mean bias error, mab = mean absolute bias, r = Pearson correlation, r\* = Pearson correlation of clear sky normalized values.

Station			HelioMont			
No	Name	n	mbe	mab	r	r*
			W m-2	W m-2	-	-
1	Bermuda	21681	-13.05	84.51	0.905	0.552
2	Cabauw	22879	-2.55	41.02	0.965	0.721
3	Camborne	11532	9.99	52.27	0.948	0.649
4	Carpentras	29286	7.35	31.57	0.984	0.672
5	De-Aar	4351	5.07	32.47	0.985	0.489
6	Lerwick	8480	8.01	51.45	0.915	0.597
7	Lindenberg	11948	-10.72	44.83	0.952	0.692
8	Palaiseau	7091	3.05	42.56	0.966	0.755
9	Payerne	26048	2.83	40.34	0.972	0.645
10	Sede-Boqer	30235	27.76	43.02	0.985	-0.083
11	Tamanrasset	30637	0.96	42.46	0.982	0.305
12	Toravere	25857	-7.60	44.28	0.950	0.687



### 15.3 Validation with SwissMetNet data

SwissMetNet is a network of ground-based automatic weather stations operated by MeteoSwiss ([http://www.meteoschweiz.admin.ch/web/en/climate/observation\\_systems/surface/swissmetnet.html](http://www.meteoschweiz.admin.ch/web/en/climate/observation_systems/surface/swissmetnet.html)). SwissMetNet is the successor of the Automatisches Messnetz (ANETZ) with higher quality and better calibrated instrumentation. It started with 16 stations in 2005, had 94 stations in 2011 and will be extended to 130 stations by 2013.

As shown by Table 16 the mab for monthly means of all SMN stations is  $5.34 \text{ W m}^{-2}$  with a consistent positive mbe of around  $3 \text{ W m}^{-2}$ . Figure 10 documents that the mab for monthly means is below  $5 \text{ W m}^{-2}$  for lowland stations and below  $10 \text{ W m}^{-2}$  for most mountainous stations. Larger biases are observed at high elevation stations located in complex terrain like Grimsel-Hospiz ( $19 \text{ W m}^{-2}$ ), Col-du-Grand-St-Bernard ( $20 \text{ W m}^{-2}$ ), Jungfrauoch ( $15 \text{ W m}^{-2}$ ), Elm ( $17 \text{ W m}^{-2}$ ), Zermatt ( $16 \text{ W m}^{-2}$ ), Monte-Rosa-Plattje ( $14 \text{ W m}^{-2}$ ), Ulrichen ( $14 \text{ W m}^{-2}$ ), Pilatus ( $13 \text{ W m}^{-2}$ ) and S.-Bernardino ( $13 \text{ W m}^{-2}$ ). These biases are very likely due to local terrain shading not represented in the horizon calculations employed at the native satellite resolution. The mean absolute bias of hourly means is around 50% larger compared to the one of (mostly flat) BSRN stations (Table 15). This is likely due to difficult and heterogeneous terrain and snow conditions in a substantial part of the SMN stations. The low Pearson correlation of clear sky normalized values ( $r^*$ ) for hourly values points out to remaining problems in the simple formulations that were used to account for snow-cloud-radiation effects in complex terrain. Future investigation could evaluate whether the use of subgrid-scale terrain and surface albedo parameterizations, such as for instance presented in *Helbig and Loewe (2012)*, and a cloud index based on a radiative transfer model, could yield a better SIS estimate for SMN stations in complex terrain.

**Table 16:** Validation of Global Radiation with SMN (2004–2011). n = number of observations, mbe = mean bias error, mab = mean absolute bias, r = Pearson correlation,  $r^*$  = Pearson correlation of clear sky normalized values, ac = correlation of anomalies.

Granularity	n	HeliMont				
		mbe W m-2	mab W m-2	r	ac	$r^*$
Inter-annual	408	$3.45 \pm 5.89$	$5.34 \pm 4.54$	$0.964 \pm 0.074$		
Monthly	4277	$3.21 \pm 5.80$	$7.71 \pm 3.98$	$0.994 \pm 0.005$	$0.941 \pm 0.038$	
Daily	126961	$3.11 \pm 5.76$	$14.74 \pm 4.71$	$0.961 \pm 0.093$		$0.885 \pm 0.107$
Hourly	1520781	$7.02 \pm 12.24$	$65.09 \pm 10.94$	$0.928 \pm 0.048$		$0.543 \pm 0.083$

SwissMetNet will be useful to analyze the spatial structure of the SIS bias, which then should enable to develop a bias correction on the daily and monthly time scale in order to generate a gridded solar irradiance dataset over Switzerland which becomes more consistent with the station measurements.

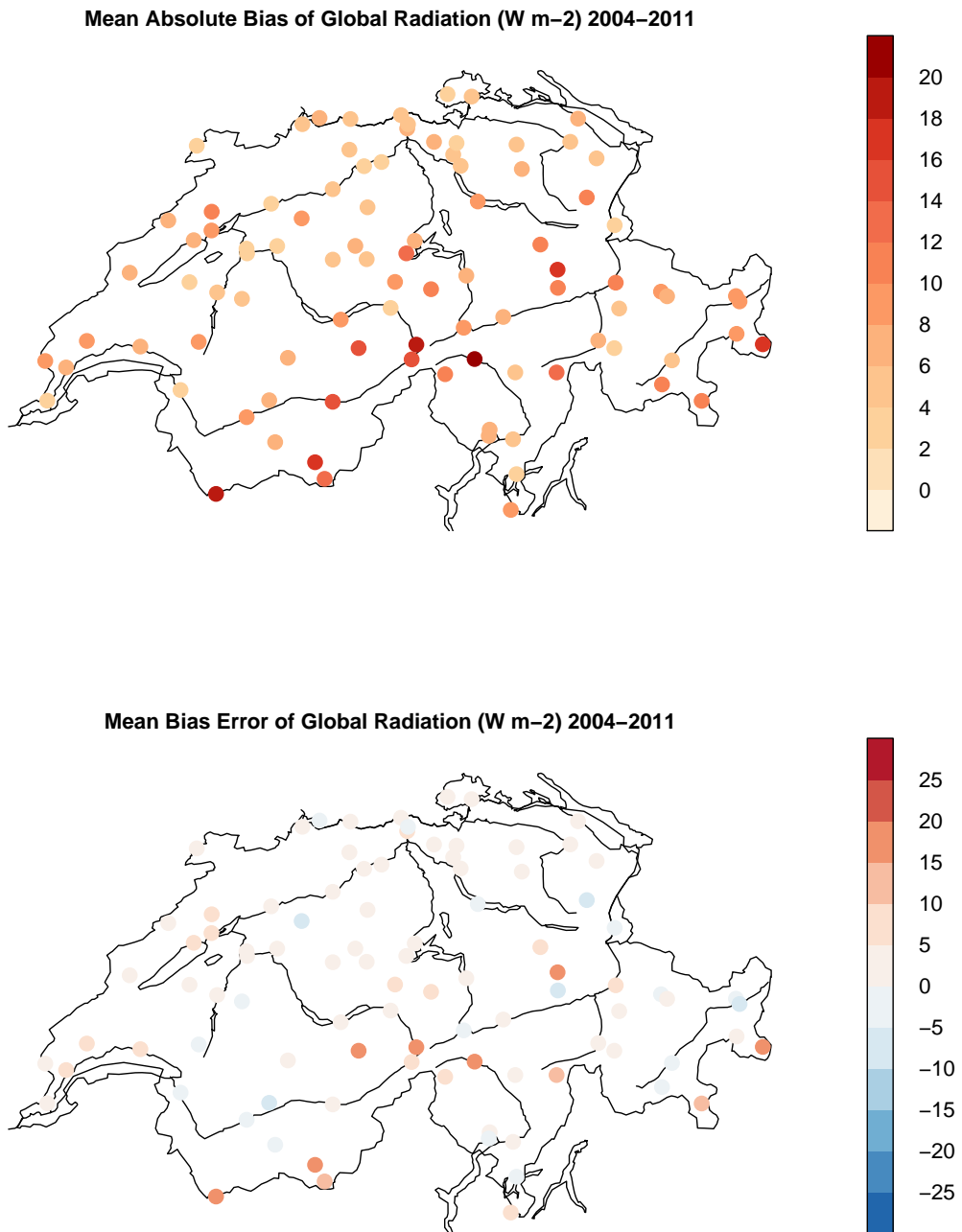


**Figure 10:** Monthly validation of the “HelioMont” global radiation mean absolute bias (mab, top panel) and mean bias error (mbe, bottom panel) with SwissMetNet.

## 15.4 Validation of Radiation Components

Direct beam and diffuse radiation components and direct normalized irradiance are consistently measured with the BSRN instrumentation. They are generally not available for either the ASRB or SMN station network. Radiation components are thus validated over the wide range of climate zones provided by BSRN but not specifically in mountainous environments. Direct beam radiation is derived from the global and diffuse radiation measurements. Direct normal irradiance is measured by BSRN.

The seasonal cycle of radiation components are represented accurately with mean absolute biases ranging in the order of 5–10 W m<sup>-2</sup> for direct beam and diffuse radiation and 10–20 W m<sup>-2</sup> for direct normal irradiance at most temperate measurement stations (Figure 11).

Table 17 demonstrates that on the monthly time scale direct beam radiation is has a mab of <10 W m<sup>-2</sup> at stations located within the temperate climate zone (except Palaiseau). Bermuda, Sede-Boqer and Tamanrasset have a mab of 20, 15 and 19 W m<sup>-2</sup>. The high mab at Palaiseau (15 W m<sup>-2</sup>) is explained by a difference of more than 100 W m<sup>-2</sup> during April which needs further investigation in both the station time series and the satellite data. The large error in the De-Aar station is explained by suspicious station data (it is shifted by 100 W m<sup>-2</sup> during January–June).

The error in diffuse radiation is in the order of 5 W m<sup>-2</sup>, except at Bermuda, Sede-Boqer and Tamanrasset (Table 18). Since Tamanrasset shows acceptable performance for SIS, either the aerosol climatology or the employed direct-diffuse radiation splitting is responsible for this error. The large error for Bermuda extends over all radiation components and is likely related to the sun glint issue discussed earlier. At Sede-Boqer the station measurement of diffuse radiation is shifted by around 50 W m<sup>-2</sup> compared to the satellite measurement during June–September which needs further investigation.

Direct normalized irradiance (DNI, Table 19) errors are in the order of 20 W m<sup>-2</sup> on the monthly time scale, except for Sede-Boqer and Tamanrasset, where they range up to 30 W m<sup>-2</sup>. Monthly mean DNI station measurements for Camborne differ by more than 50 W m<sup>-2</sup> from the satellite data which needs further investigation, especially since all other radiation components at this station have a very low bias.

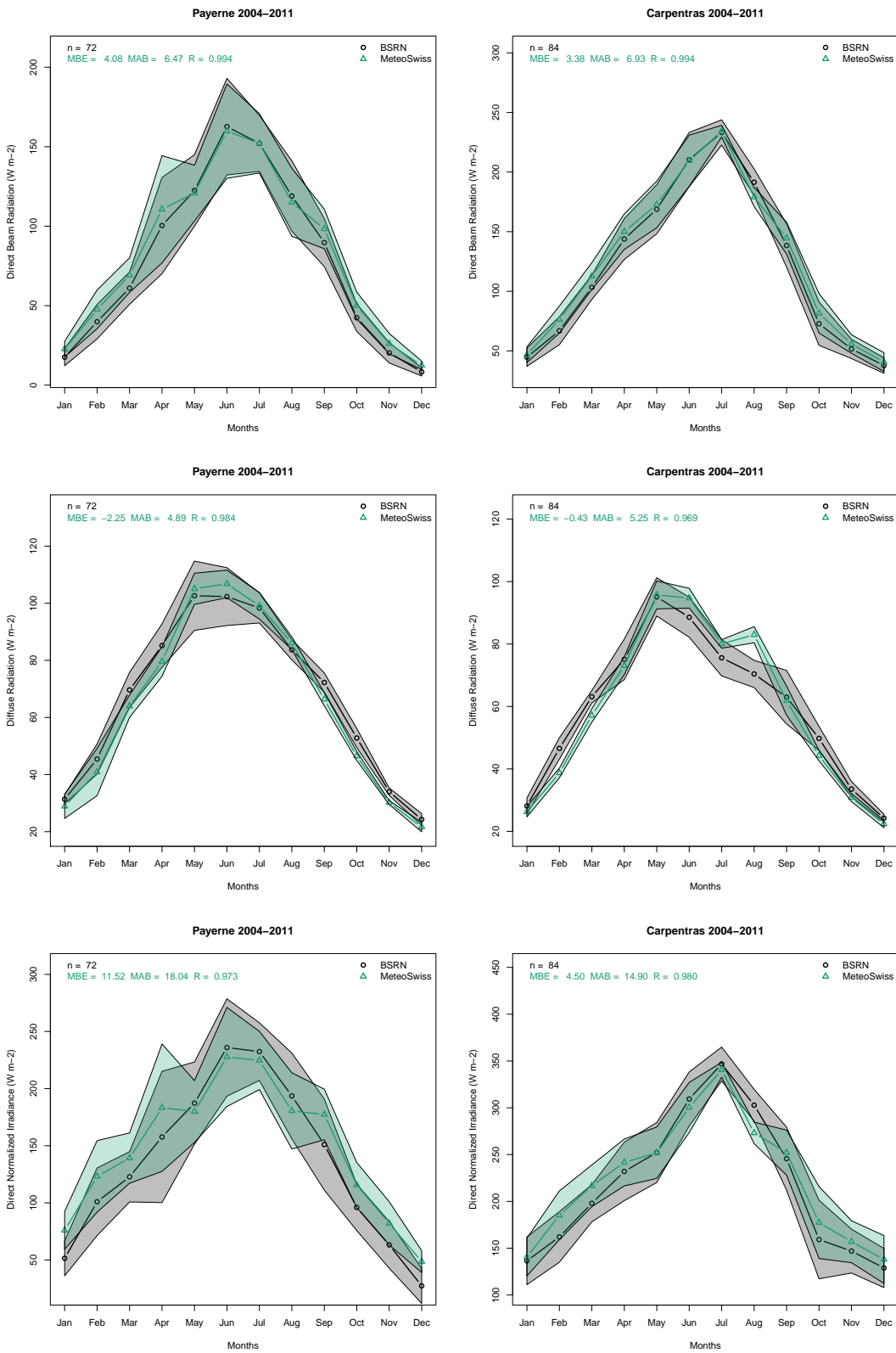


**Figure 11:** Monthly comparison of direct beam (top), diffuse (middle) and direct normalized (bottom) solar irradiance with BSRN stations Payerne (left) and Carpentras (right) for the years 2004–2011. The shaded area represents the inter-annual variability (standard deviation of monthly values).

**Table 17:** Monthly comparison of Direct Beam Radiation with BSRN (2004–2011). n = number of observations, mbe = mean bias error, mab = mean absolute bias, r = Pearson correlation. Values marked with a (\*) have a suspicious seasonal cycle or unrealistic offsets in the station measurements.

Station			"HeliMont"		
No	Name	n	mbe	mab	r
			W m-2	W m-2	-
1	Bermuda	73	18.55	19.54	0.902
2	Cabauw	70	1.19	3.46	0.993
3	Camborne	34	7.15	7.73	0.991
4	Carpentras	84	3.38	6.93	0.994
5	De-Aar	12	57.75*	70.58*	0.605*
6	Lerwick	25	-1.68	12.09	0.804
7	Lindenberg	36	-10.07	10.58	0.991
8	Palaiseau	22	15.68*	15.74*	0.774*
9	Payerne	72	4.08	6.47	0.994
10	Sede-Boqer	84	1.66	15.35	0.973
11	Tamanrasset	84	-14.50	19.14	0.830
12	Toravere	78	-10.80	11.97	0.987

**Table 18:** Monthly comparison of Diffuse Radiation with BSRN (2004–2011). n = number of observations, mbe = mean bias error, mab = mean absolute bias, r = Pearson correlation. Values marked with a (\*) have a suspicious seasonal cycle or unrealistic offsets in the station measurements.

Station			"HeliMont"		
No	Name	n	mbe	mab	r
			W m-2	W m-2	-
1	Bermuda	73	-15.29	16.51	0.922
2	Cabauw	70	-2.66	4.18	0.994
3	Camborne	34	-2.00	4.42	0.986
4	Carpentras	84	-0.43	5.25	0.969
5	De-Aar	12	3.89	13.75	0.719
6	Lerwick	25	-0.22	5.26	0.978
7	Lindenberg	36	3.99	6.42	0.985
8	Palaiseau	41	-6.34	9.22	0.807
9	Payerne	72	-2.25	4.89	0.984
10	Sede-Boqer	84	13.63*	16.17*	0.689*
11	Tamanrasset	84	18.16	19.35	0.910
12	Toravere	78	6.24	8.24	0.985

**Table 19:** Monthly comparison of Direct Normalized Irradiance with BSRN (2004–2011). n = number of observations, mbe = mean bias error, mab = mean absolute bias, r = Pearson correlation.

No	Station Name	n	"HelioMont"		
			mbe W m-2	mab W m-2	r -
1	Bermuda	73	4.33	17.11	0.913
2	Cabauw	70	4.52	10.41	0.982
3	Camborne	36	28.55*	28.83*	0.827*
4	Carpentras	84	4.50	14.90	0.980
5	De-Aar	12	-13.13	25.21	0.782
6	Lerwick	25	10.58	20.44	0.908
7	Lindenberg	36	-19.48	23.38	0.973
8	Palaiseau	42	21.51	23.53	0.757
9	Payerne	72	11.52	18.04	0.973
10	Sede-Boqer	84	9.00	30.43	0.785
11	Tamanrasset	84	-21.12	30.86	0.831
12	Toravere	78	-19.79	24.95	0.967

## 15.5 Validation of Clear Sky Radiation

Clear sky radiation was derived from ASRB station measurements and satellite-based all sky radiation by only selecting the time steps where the clear sky index  $K = G/G_{cf} \geq 0.99$ .  $G_{cf}$  is the modeled clear sky radiation from “HeliMont” and  $G$  is the ASRB-measured or MSG-derived all sky SIS. Clear sky radiation comparisons are thus only performed when both the station measurement and the satellite time series are close to the “potential” (modeled) clear sky radiation. This screening is only possible on the sub-daily time scale.

Clear sky radiation has a negative mean bias error of around -10 to -25  $W m^{-2}$  with a corresponding mean absolute bias of 10-25  $W m^{-2}$  on the hourly time scale (Table 20). Despite the above strict threshold Figure 12 demonstrates that a large part of this negative mean bias error is likely to be caused by the false inclusion of only slightly partly cloudy cases in the MSG data during the analysis. With 1000  $W m^{-2}$  clear sky irradiance a small 1% radiative cloud forcing can already generate a negative bias of -10  $W m^{-2}$ . Figure 12 also demonstrates that the clear sky radiation is likely unbiased for the Swiss lowlands but underestimated in both mountainous regions and for southern Switzerland. This might likely be related to the large scale aerosol climatology which, in comparison to the large scale water vapor fields, is not downscaled to the fine scale orography of the Alps.

**Table 20:** Hourly comparison of clear sky Global Radiation with ASRB (2004–2010). n = number of observations, mbe = mean bias error, mab = mean absolute bias, r = Pearson correlation.

Station		MeteoSwiss			
No	Name	n	mbe	mab	r
			W m-2	W m-2	-
1	Locarno-Monti	6160	-24.99	25.76	0.996
2	Payerne	3416	-8.26	12.12	0.999
3	Davos	5217	-21.65	22.32	0.994
4	Cimetta	6388	-17.90	21.57	0.998
5	Maennlichen	5160	-16.07	19.57	0.998
6	SLF-Versuchsfeld	5199	-24.46	26.35	0.989
7	Weissfluhjoch	5858	-18.13	21.17	0.997
8	Eggishorn	5735	-18.97	24.16	0.997
9	Gornergrat	8425	-13.01	16.29	0.998

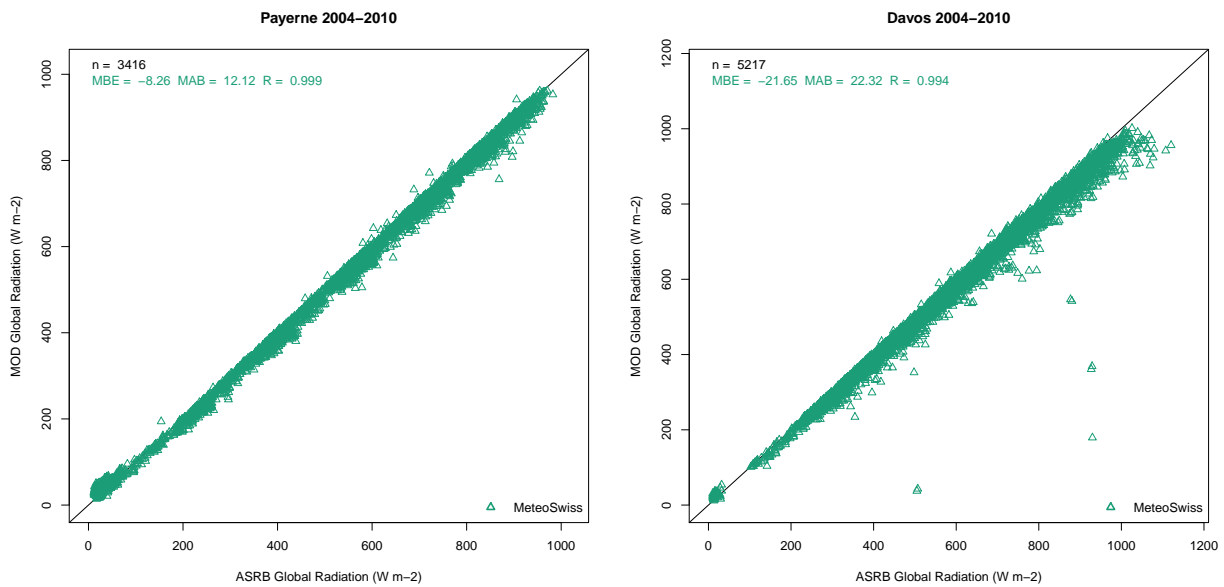


**Figure 12:** Hourly comparison of clear sky Global Radiation with ASRB (2004–2010).



## 16 Intercomparison

### 16.1 Intercomparison with Duerr et al. 2009

The dataset generated by *Dürr and Zelenka* (2009) (D09) was the starting point for the current version of “HelioMont”. D09 thus serves as a benchmark for the new developments described in this report. *Dürr et al.* (2010) reported relative monthly biases in the order of 10% depending on season and station. Highest mean absolute biases of 10–30 W m<sup>-2</sup> were observed during spring. Negative mean bias errors occurred over snow-covered locations.

Figure 13 documents the methodological improvements that were made by changing the empirical cloud mask to a probabilistic cloud mask, by modifying the clear sky compositing, and introducing both an infrared cloud index and a physically-based clear sky radiative transfer model. The differences between D09 and “HelioMont” are not obvious for the lowland stations Payerne and Locarno-Monti. The mab however decreases from around 10–20 W m<sup>-2</sup> in D09 to 5–10 W m<sup>-2</sup> in “HelioMont” for the Alpine stations Davos, Cimetta, SLF-Versuchsfeld, Weissfluhjoch, Eggishorn and Gornergrat. The biases in D09 are negative at all high elevation stations which suggests that the algorithm used in D09 either falsely identifies snow as clouds or does not sufficiently include the radiative effects of snow. Compared to D09 the spread of the bias was reduced at almost all ASRB stations which increases the suitability of “HelioMont” for climate monitoring purposes.

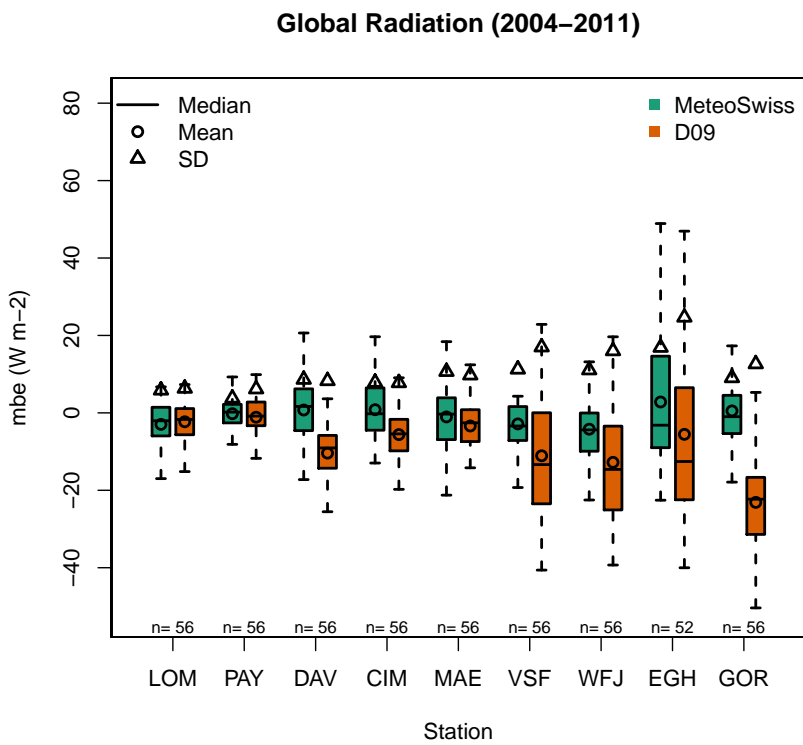
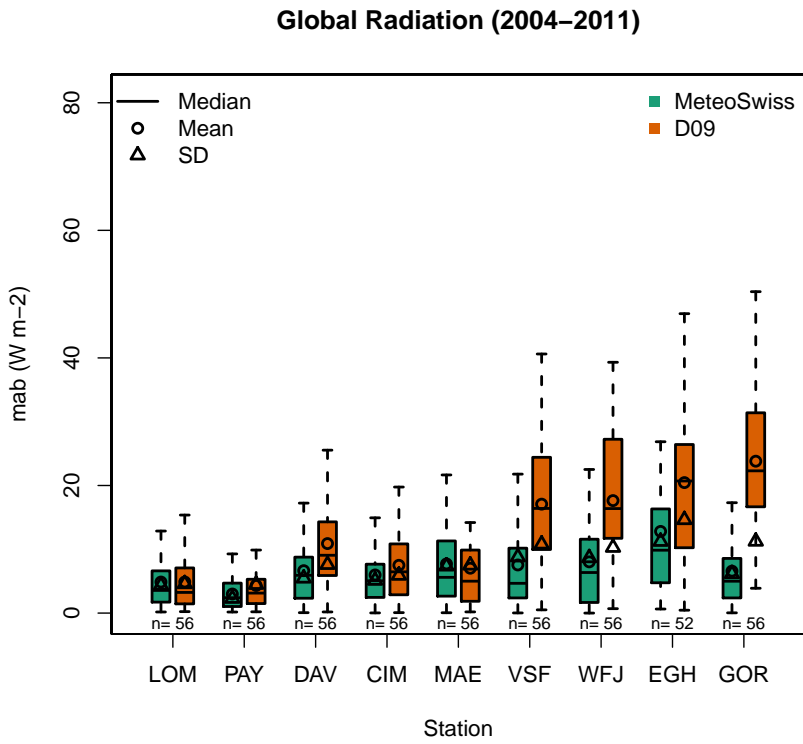


**Figure 13:** Monthly inter-comparison of mean absolute bias (mab, top panel) and mean bias error (mbe, bottom panel) of the “HelioMont” global radiation with *Dürr and Zelenka (2009)* at ASRB sites.

## 16.2 Intercomparison with HelioClim

Helioclim (<http://www.helioclim.org>) is an ongoing effort of the Ecole des Mines de Paris (Armines) Center for Energy and Processes to provide information on solar radiation for research purposes and for commercial applications. HelioClim data can be accessed through the SoDa Service (<http://www.soda-is.com>). HelioClim-1 (HC1) data is freely available up to 2005 and is based on MFG (Cros *et al.*, 2004). HelioClim-3 (HC3) is based on an improved algorithm using MSG data and is generated since 2004. It is only available through commercial licensing but can be accessed in almost real-time (Rigollier *et al.*, 2004). Both HC1 and HC3 serve as reference data sets since they are widely used within the European and African solar energy community.

HC1 has unrealistic negative mean bias errors of around -20 to -50 W m<sup>-2</sup> even at lowland stations (Figure 14). In mountain environments and over snow HC1 under-estimates global radiation. Some of these deficiencies were already demonstrated by Posselt *et al.* (2012). HC3 offers a higher precision compared to HC1. However, at the Swiss lowland stations the associated mean absolute biases are around 3-4 times higher than for “HelioMont” (12-14 W m<sup>-2</sup> compared to 3-5 W m<sup>-2</sup>). In mountainous environment and over snow HC3 over-estimates global radiation by around 15-20 W m<sup>-2</sup> while the mean bias error for “HelioMont” is in the order of 5-10 W m<sup>-2</sup>.

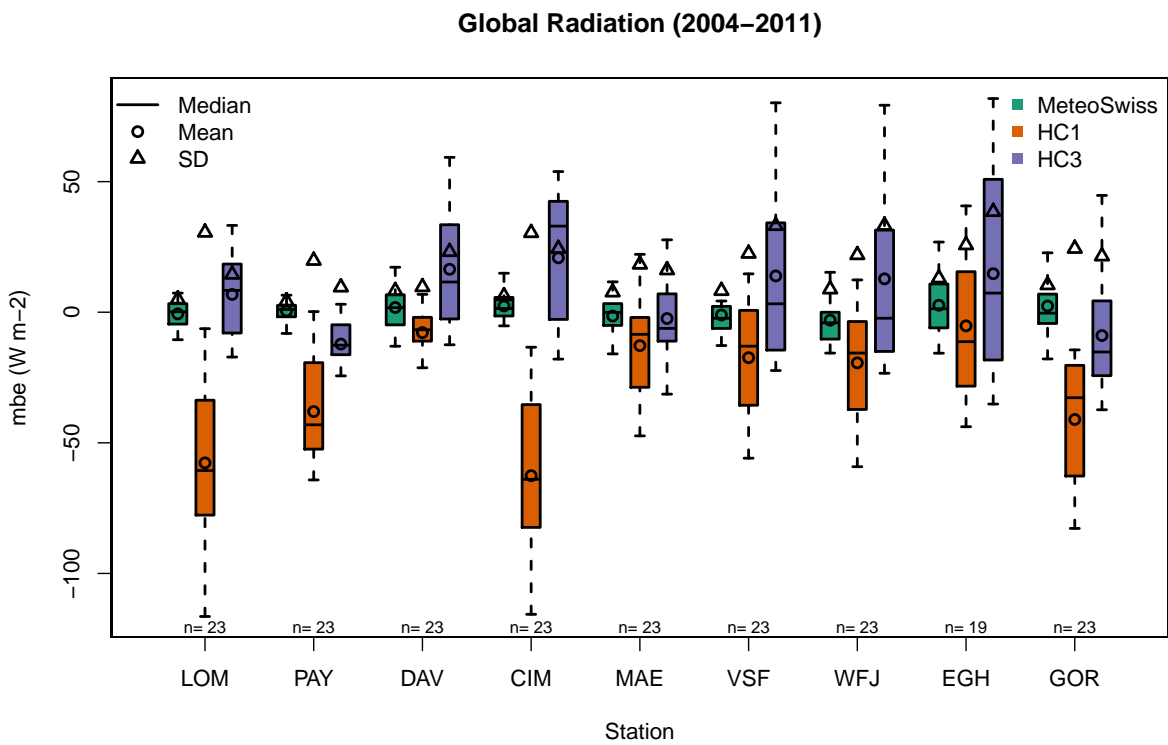
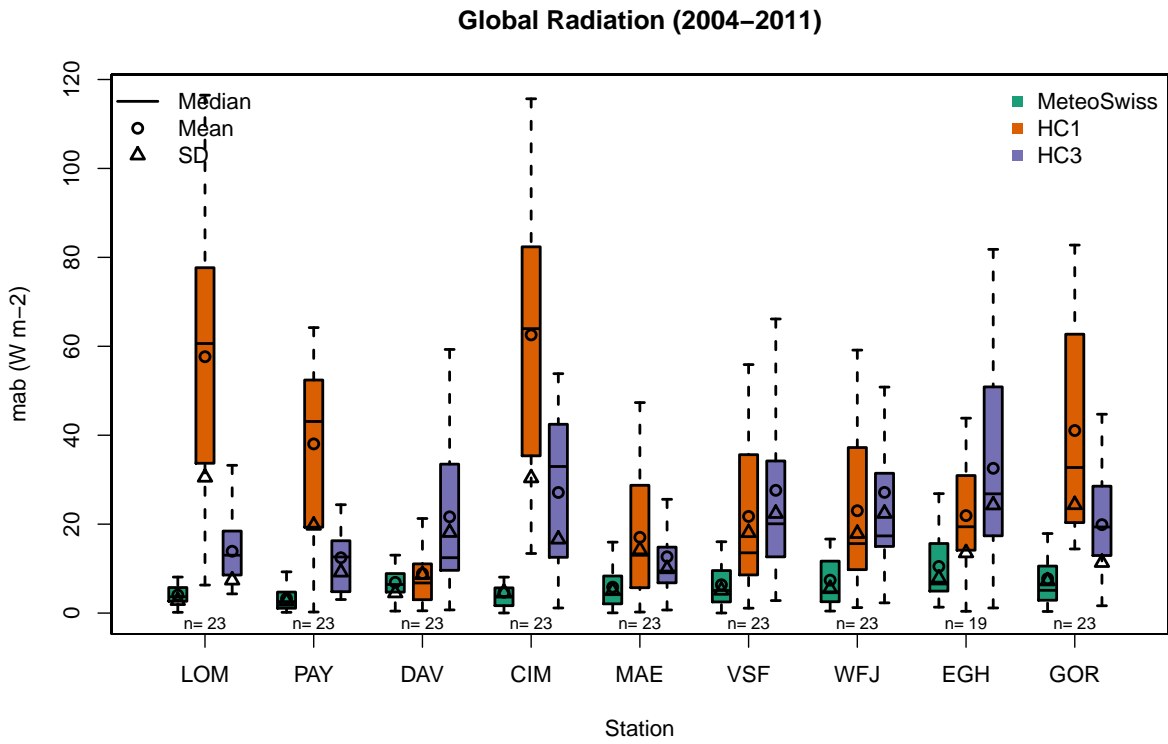


**Figure 14:** Monthly inter-comparison of mean absolute bias (mab, top panel) and mean bias error (mbe, bottom panel) of the “HelioMont” global radiation with HelioClim 1 and 3 at ASRB sites.

### 16.3 Inter-comparison with ISCCP and GEWEX

The International Satellite Cloud Climatology Project (ISCCP) was established in 1982 as part of the World Climate Research Program (WCRP) to collect and analyze satellite radiance measurements to infer the global distribution of clouds, their properties, and their diurnal, seasonal, and inter-annual variations (<http://isccp.giss.nasa.gov/>). ISCCP is the longest ongoing satellite climatology project and it is widely used by the global climate modeling community to evaluate simulated cloud states and atmospheric radiation fluxes (*Rossow and Duenas, 2004*). The Climatological Summary Product Surface Radiative Fluxes (FD-SRF) at a spatial resolution of 280km and with a 3 hourly time step from 2004–2007 is used in this inter-comparison (*Zhang et al., 2004*). Station data are extracted by nearest-neighbor sampling the coarse ISCCP grid to station locations.

The goal of the Global Energy and Water Exchanges (GEWEX) is to provide global earth radiation budget and energy flux datasets. Within GEWEX the SRB project determines surface and top-of-atmosphere radiative fluxes to support the analysis of climate variations and decadal to centennial climate trends (<http://gewex-srb.larc.nasa.gov/>, *Gupta et al. (1999)*). The Release 3.0 of the GEWEX-SRB daily shortwave surface radiation data from 2004–2009 was used in this inter-comparison *Gupta et al. (2006)*. It uses the ISCCP cloud parameters to calculate shortwave surface radiation fluxes by use of the *Pinker and Laszlo (1992)* algorithm.

Both GEWEX and ISCCP under-estimate monthly mean global radiation at all ASRB stations, with mean absolute biases increasing at high elevation stations (Figure 15). Some of these effects could be due to the inferior spatial resolution of these two inter-comparison datasets. However, according to *Zelenka et al. (1999)* (Figure 6) the spatial variogram of monthly mean global radiation does not significantly increase for distances of 0–175 km. It only becomes very sensitive to distance at sub-daily time resolution. The mismatch in spatial resolution can thus only partly contribute to the spread of the mean absolute bias. This mismatch is likely below  $10 \text{ W m}^{-2}$  such as found for low-elevation stations Payerne or Locarno-Monti. At high elevation stations like Weissfluhjoch or Gornergrat the mean absolute bias is much higher. This is more likely due to mis-classification of snow as clouds in the employed processing schemes. Monthly mean absolute biases for GEWEX and ISCCP are in the order of  $30\text{--}50 \text{ W m}^{-2}$  for high elevation stations (compared to  $5\text{--}10 \text{ W m}^{-2}$  for “HelioMont”) which renders these datasets unsuitable for solar radiation and climate monitoring applications in Alpine terrain.

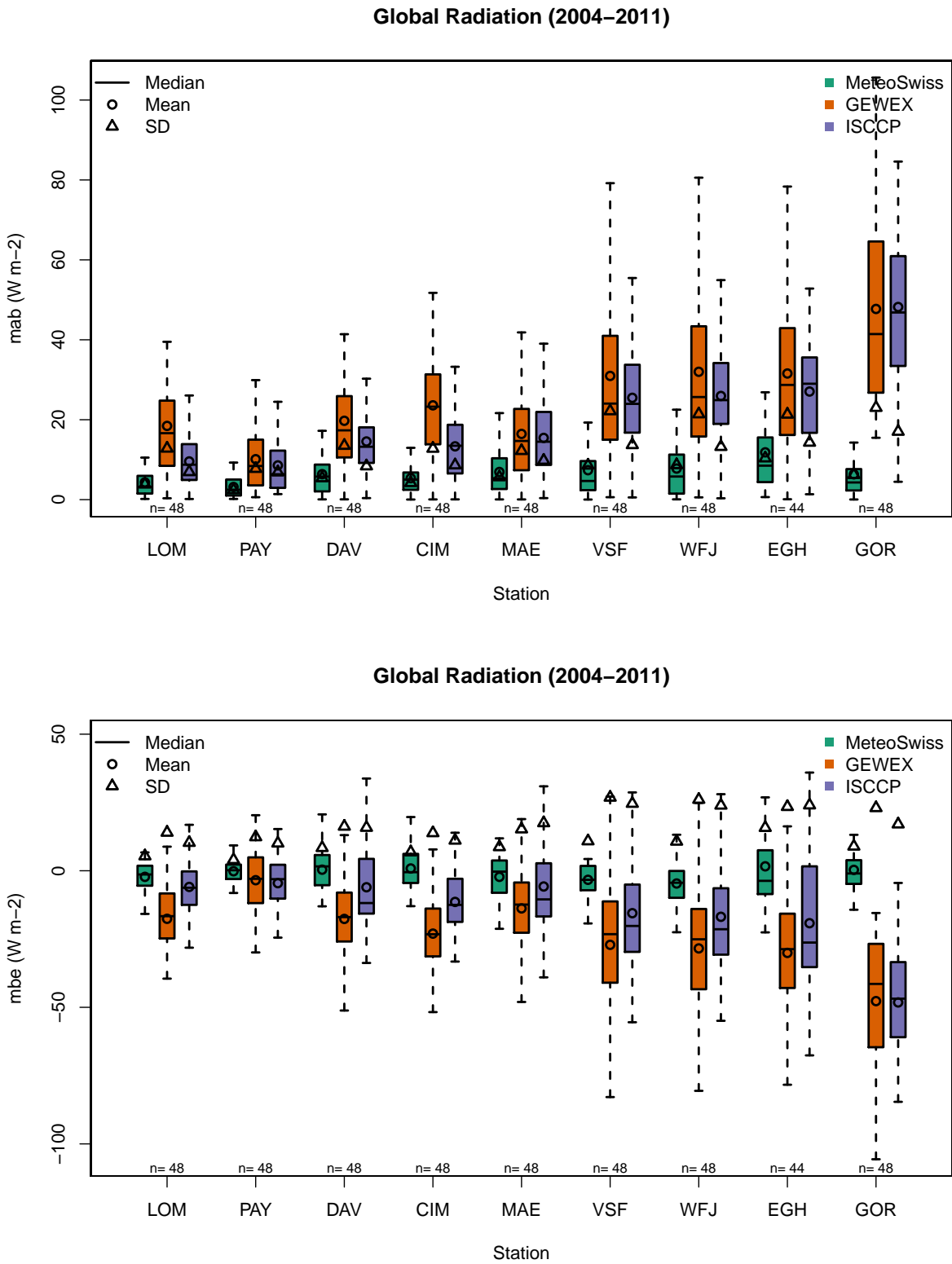


**Figure 15:** Monthly inter-comparison of mean absolute bias (mab, top panel) and mean bias error (mbe, bottom panel) of the “HelioMont” global radiation with GEWEX SRB and ISCCP DX at ASRB sites.

## 16.4 Intercomparison with ECMWF ERA Interim

The European Center for Medium-Range Weather Forecasts (ECMWF) Interim reanalysis project (ERA Interim) covers the period from 1979 until now and has become a widely used dataset for climate analysis, climate monitoring and for climate model evaluation (<http://www.ecmwf.int>, Dee *et al.* (2011)). Surface radiation fluxes are available on a 6-hourly time step at the T255 spatial resolution with global coverage. The ERA Interim dataset is a model-based re-analysis constrained by surface and upper air data in combination with many infrared and microwave satellite sensors available on geostationary and polar platforms. Surface radiation fluxes are only available as forecasted fields and they are cumulated over the forecast period. In this inter-comparison the 0 h UTC forecast for the time period 2004–2012 (re-gridded to a regular  $1^\circ \times 1^\circ$  global grid) is used, where the mean 6-hourly surface solar irradiance was calculated by subtracting the T +0 h and T +6 h forecast steps from each other. Station data are extracted by nearest-neighbor sampling the coarse ERA Interim grid to station locations.

Despite the low spatial resolution the ERA Interim data have low mean bias errors in the order of  $-10 \text{ W m}^{-2}$  (Table 16). Both mean absolute biases and mean bias errors become substantially larger than “HeliMont” for the stations SLF-Versuchsfeld, Weissfluhjoch, Eggishorn and Gornergrat. In comparison to most satellite-based datasets the ERA Interim model-based data is not affected by the cloud-snow confusion issue. However, the realism of modeled snow cover and scaling issues of snow-radiation effects in the coarse ERA Interim dataset are likely responsible for the negative bias at high elevation stations.

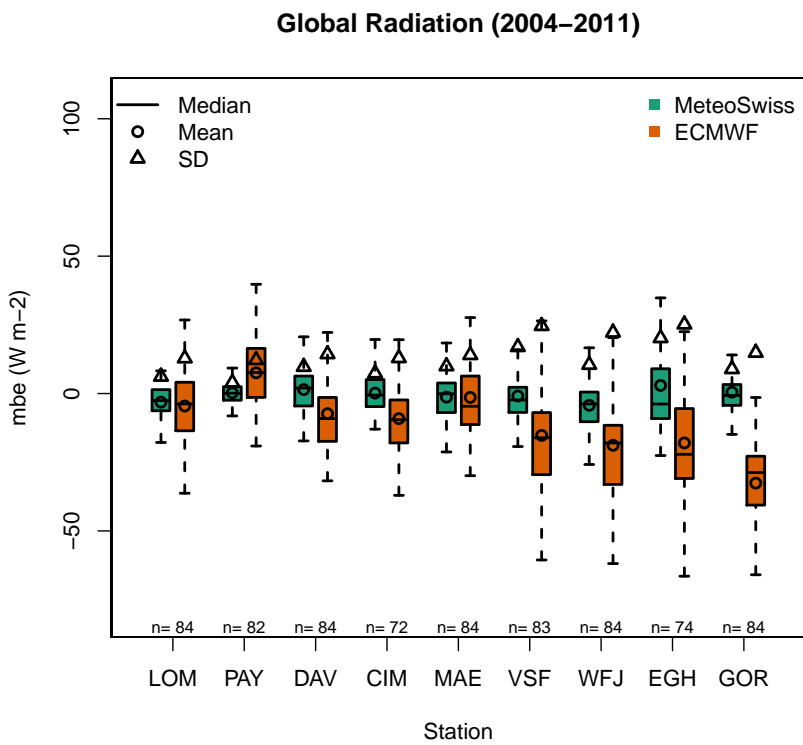
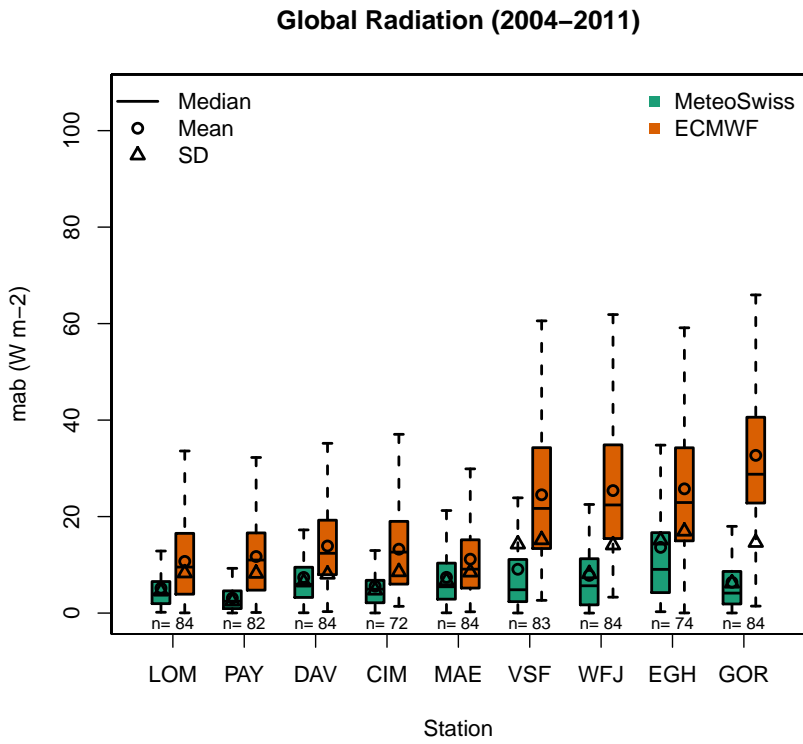


**Figure 16:** Monthly inter-comparison of mean absolute bias (mab, top panel) and mean bias error (mbe, bottom panel) of the “HeliMont” global radiation with ECMWF ERA Interim at ASRB sites.



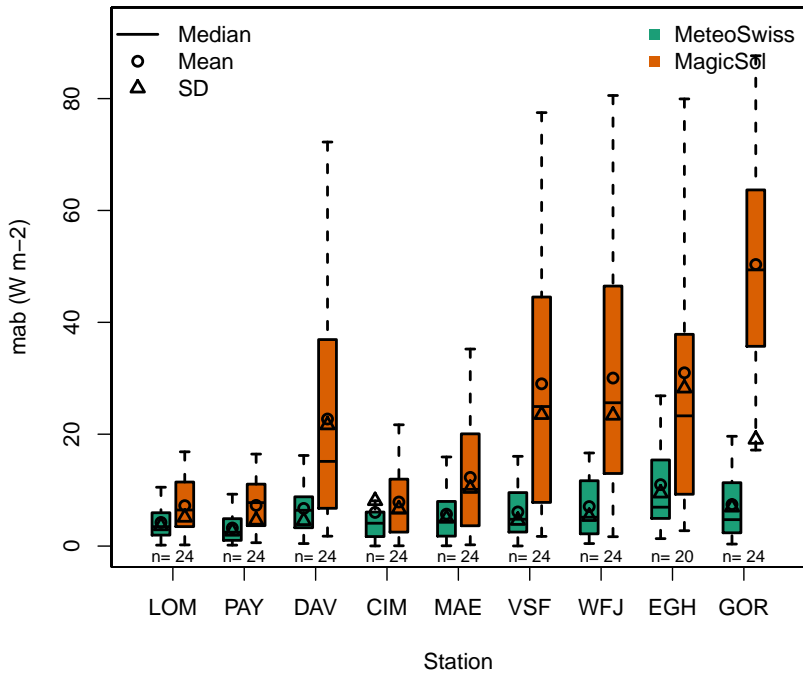
## 16.5 Intercomparison with CM SAF

During the Continuous Development and Operations Phase (CDOP-1) CM SAF generated publicly available surface solar radiation climate data records covering both the first and second generation Meteosat satellites (<http://wui.cmsaf.eu>). The MagicSol dataset provides global radiation and direct beam radiation at the hourly time step with a spatial resolution of  $0.03^\circ$  for the time period 1983–2005. It is based on MFG MVIRI data and uses a climate version of the well known Heliosat algorithm (Posselt *et al.*, 2012). MagicSol covers the full Meteosat disc and aims at providing stable and homogeneous surface solar radiation climatologies for climate analysis, climate monitoring and solar energy applications. Complementary to MagicSol CM SAF generates an operational surface solar irradiance data set since 2004 (here referred to as CM SAF). It is based on MSG SEVIRI data and uses a radiative transfer model to calculate both clear sky and cloudy surface radiation fluxes with the help of the operational CM SAF cloud mask (Müller *et al.*, 2009).

Both CM SAF datasets fulfill GCOS requirements in flat terrain ( $15 \text{ W m}^{-2}$  mean absolute bias for monthly mean values). The employed algorithms are not specifically created for mountainous terrain and bright surface targets. Dürr *et al.* (2010) demonstrated that the operational CM SAF data set has a substantial negative bias over snow covered areas, specifically during spring when ToA solar radiation increases and snow cover still persists.

Of all above presented inter-comparison datasets the CM SAF Operational dataset performs best over the Swiss lowland stations Payerne and Locarno-Monti, closely followed by the CM SAF MagicSol dataset (Figures 17 and 18). The CM SAF Operational dataset has a lower mab than “HeliMont” for Locarno-Monti ( $4.5$  versus  $6.3 \text{ W m}^{-2}$ ) but a higher mab for Payerne ( $5.6$  versus  $3.2 \text{ W m}^{-2}$ ). Both the MagicSol and the Operational datasets have a mab  $< 10 \text{ W m}^{-2}$  for Cimetta comparable to “HeliMont”. At most other high elevation stations mab increases to  $20\text{--}50 \text{ W m}^{-2}$  for MagicSol and  $30\text{--}50 \text{ W m}^{-2}$  for the Operational dataset. Mean bias errors become highly negative for SLF-Versuchsfeld, Weissfluhjoch and Gornergrat for both CM SAF datasets. The bias is around  $-20 \text{ W m}^{-2}$  for MagicSol and  $-40 \text{ W m}^{-2}$  for the Operational dataset. While the radiative cloud forcing of MagicSol is calculated with the classical Heliosat approach which is known to have deficiencies in snow covered areas, the CM SAF operational dataset depends on the cloud optical thickness parameter derived with a multi-channel algorithm (CM SAF, 2010). Our analysis demonstrates that the latter approach can be beneficial for certain high elevation stations (Maennlichen) but it still yields high errors, very likely due to snow/cloud issues, at most other high elevation stations (SLF-Versuchsfeld, Weissfluhjoch, Eggishorn and Gornergrat).

### Global Radiation (2004–2011)



### Global Radiation (2004–2011)

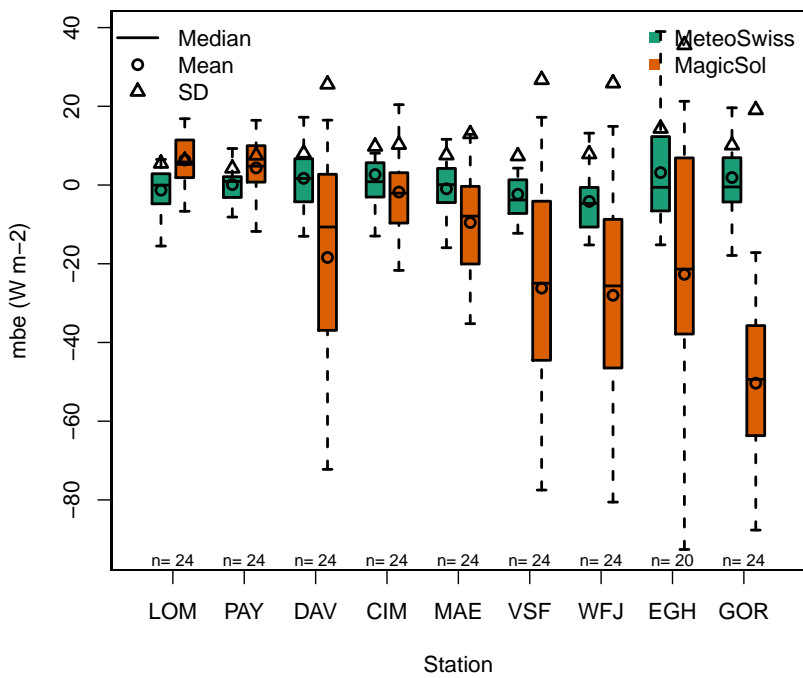


**Figure 17:** Monthly inter-comparison of mean absolute bias (mab, top panel) and mean bias error (mbe, bottom panel) of the “HelioMont” global radiation with the CM SAF MagicSol dataset at ASRB sites.

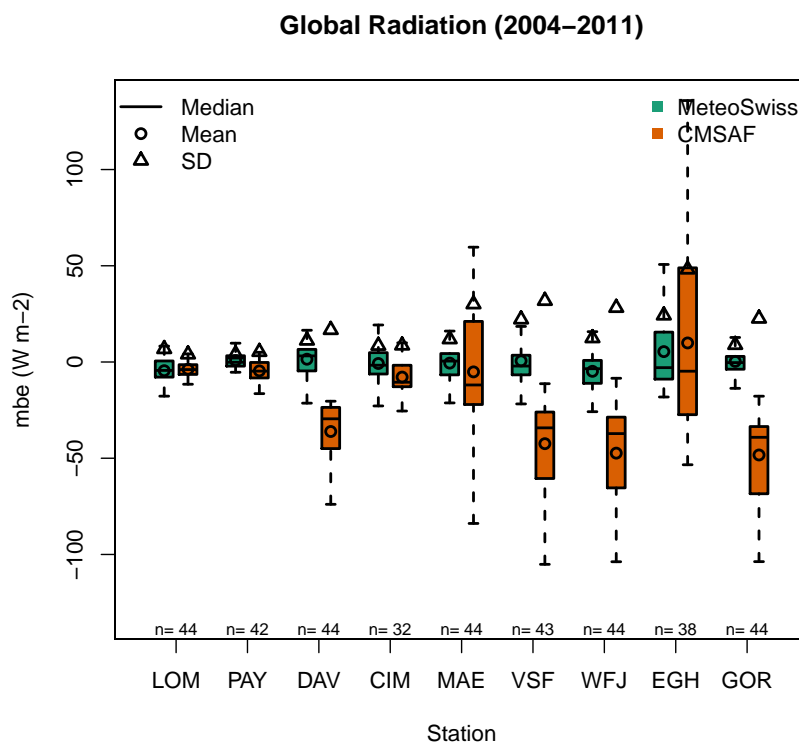
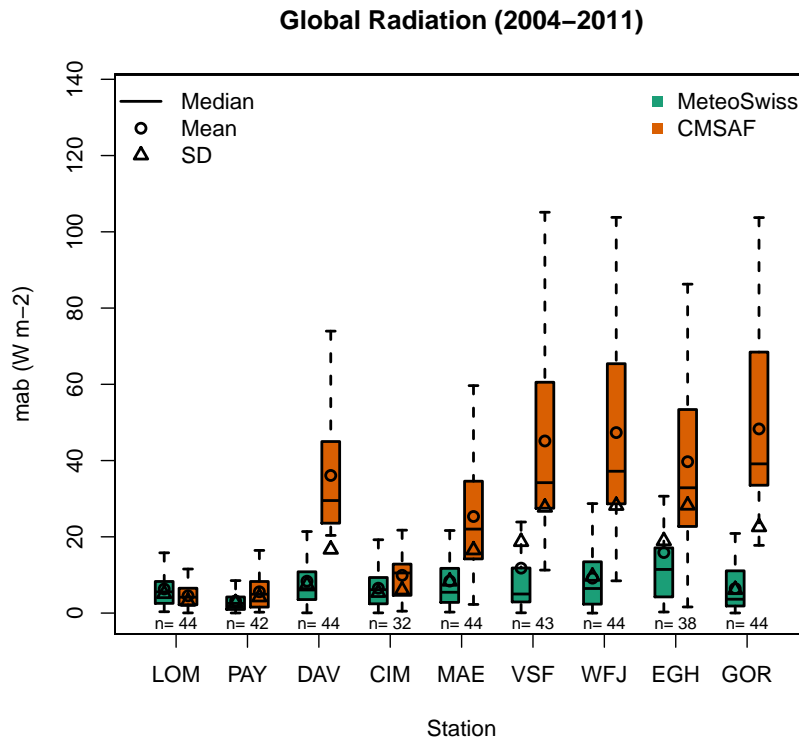


**Figure 18:** Monthly inter-comparison of mean absolute bias (mab, top panel) and mean bias error (mbe, bottom panel) of the “HeliMont” global radiation with the CM SAF operational dataset at ASRB sites.

## 17 Outlook and Suggestions for Improvements

The “HelioMont” framework calculates the surface solar radiation flux including radiation flux components from MSG SEVIRI data. “HelioMont” mostly integrates well established methods into a physically-based and self-consistent processing system. Some algorithms, such as the infrared cloud index, have been specifically developed for “HelioMont”. Others, like the cloud mask, have been substantially modified from the published ones. These algorithms will need to be individually evaluated as a next step since the validation carried out for this report is limited to surface radiation fluxes. During the CM SAF Continuous Development and Operations Phase 2 (CDOP-2) a version of the cloud mask described here will for instance be evaluated, implemented and extended for its applicability to both MFG MVIRI and MSG SEVIRI. Also, a continuous development of “HelioMont” could include the following improvements and enhancements. They could help to remedy some of the remaining deficiencies found in the validation section of this report and they are important to render “HelioMont” into a more generally applicable processing framework for satellite climatology in complex terrain.

### 17.1 Radiance Inter-Calibration

Top-of-Atmosphere radiances are calculated by use of the EUMETSAT-provided calibration factors as part of the MSG Level 1.5 data. They are not necessarily up-to-date and neither qualify for an absolute radiometric calibration traceable to S.I. standards. Under the umbrella of the World Meteorological Organization (WMO) the Global Space-based Inter-Calibration System (GSICS) has become the de-facto standard for calibration of space-based earth observation sensors (*Goldberg et al.*, 2011). Several space agencies including EUMETSAT provide current and historic radiance calibration coefficients derived by inter-comparison with reference radiometers during simultaneous Nadir overpasses (SNO's) for thermal channels that could replace the standard MSG Level 1.5 calibration coefficients when converting DN's to radiances. Currently these calibration factors are limited to thermal channels and they are only applicable to modern sensors (inter-calibration with IASI). However under the umbrella of GSICS various inter-calibration methods for solar channels are developed and inter-calibration for solar and thermal channels is currently carried out back in time to older sensor generations where applicable (inter-calibration of MVIRI thermal channels with HIRS). Like any modern satellite-based climate data record processing “HelioMont” relies on a Fundamental Climate Data Record (FCDR) providing well-calibrated radiances in both space and time. It is thus recommended to implement GSICS-based inter-calibration coefficients as soon as they become

available for solar channels and for heritage sensors such as MFG MVIRI.

## 17.2 Satellite Sensors

The “HelioMont” framework has been developed for MSG SEVIRI. The cloud masking, clear sky compositing and the surface solar radiation processing would also be applicable to heritage sensors like MFG MVIRI with a higher uncertainty. A climatological surface radiation time series covering the Alps could thus be derived back to 1983 with a consistent set of algorithms. The physical algorithms in “HelioMont” could also be applied to other geostationary sensors with some modifications. They would for instance include the high and low-resolution channel co-registration, the radiance calculation, the satellite data format and the analysis of the metadata such as quality flags. Further, several spectrally-dependent algorithms such as the calculation of the maximum planetary reflectance in dependence of the satellite and sun orbital geometry would need to be adapted to the spectral configuration of each specific sensor type.

## 17.3 Cloud Masking

The aggregated and continuous rating cloud mask employed in “HelioMont” offers several advantages over traditional binary decision tree cloud masks. However, the method still requires the empirical estimation of scaling and offset coefficients in order to weight and de-bias individual scores before summing them up for the final cloud amount metric. These limitations have recently been overcome by the advent of physically-based cloud masks employing an optimal estimation of the most probable cloud state using multi-spectral and all-sky radiative transfer model simulations (*Poulsen et al., 2012*). The resulting cloud state also includes an uncertainty estimate which accurately represents the power of the spectral discrimination for a given scene composition and sensor type. In comparison to empirical methods they allow the joint retrieval of cloud macrophysical and microphysical properties such as cloud height, top temperature, cloud droplet size or liquid and ice water path. In future versions of “HelioMont” such a cloud mask based on optimal estimation should be carefully evaluated. Special emphasis would need to be given to the temporal scores. Temporal variability is not currently used in optimal estimation approaches. Temporal variability is however very powerful for cloud masking geostationary satellite data with a poor spectral coverage.

## 17.4 Clear Sky Compositing

In “HelioMont” clear sky compositing is needed to calculate cloud free diurnal cycles of reflectance and brightness temperature by use of empirical models. The retrieved clear sky states include atmospheric and surface directional effects. They are thus Top-of-Atmosphere (ToA) states. As a next step the clear sky compositing could be turned into a more physically-based retrieval of clear sky surface states. For solar channels the atmospherically corrected surface reflectance, the surface bidirectional reflectance distribution function, and the hemispherical black and white-sky narrow- and broad-band albedo could be retrieved. However, most classical albedo retrieval methods ignore the effects of complex terrain such as terrain shadow and non plane-parallel illumination conditions. An

all-terrain broad-band hemispherical surface albedo algorithm would thus need to be developed. It could then serve as input to the calculation of the terrain-reflected diffuse radiation component and for cloud screening. For thermal channels the clear sky radiative land surface temperature could be derived from the clear sky ToA brightness temperature by use of a split-window or single channel LST retrieval. This will be achieved during CM SAF CDOP-2. A MFG MVIRI and MSG SEVIRI LST retrieval will be developed in collaboration with the LSA SAF which will result in a 30+ year full disk LST CDR covering both Meteosat generations. Clear sky LST retrieval could then be extended with an all sky LST model which would allow to derive a climate data record of LST.

## 17.5 Cloud Index

The cloud index is one of the last remaining empirical components in “HelioMont”. Since the advent of Heliosat almost three decades ago its formulation has been unchanged. Limitations of the cloud index have been partly overcome here by the choice of yet another empirical method called the “infrared cloud index”. However, in analogy to the proposed optimal estimation approach for cloud masking (see above), a radiative transfer model could also be employed to invert the most likely cloud optical thickness for a given spectral reflectance and brightness temperature combination. This cloud optical thickness including its uncertainty can then be used in RTM forward simulations to calculate the all-sky surface radiation components. However, in comparison to the empirical cloud index which employs ToA clear sky reflectance and brightness temperature as background fields, the physically consistent method requires the presence of atmospherically corrected broad-band and narrow-band hemispherical surface albedo and radiative surface temperature (for both water and land) as background fields. They would have to be concurrently calculated by clear sky radiative transfer modeling as part of the clear sky compositing (see above).

## 17.6 Surface Radiation

Validation of modeled direct and diffuse radiation components with ground-based measurements is currently limited due to the following differences in the methods used for both measurement and modeling. For calculating the direct radiation the sun is modeled as a point source (as in most other radiative transfer models, including libRadtran). It should however be modeled as a disc with its actual radius in order to be more compatible with pyrheliometers which measure the direct radiation component by use of an instrument opening angle which is slightly larger than the sun’s disc. The measured direct beam component can thus also include some diffuse radiation in regions with a high aerosol load. Diffuse radiation further has an anisotropic distribution on the hemisphere, which is often highly condensed around the sun’s disc. The shadow band of pyranometers on the other hand excludes some of the hemisphere. The measured diffuse radiation can thus underestimate the actual hemispherical diffuse radiation. These differences need to be accounted for when comparing modeled and measured radiation components.

The calculation of the clear sky surface radiation would highly benefit from replacing the currently large-scale aerosol climatology with a daily aerosol reanalysis dataset including the vertical structure. The availability of spectrally resolved radiation components would be beneficial for yield estimates of

photovoltaic (PV) solar power applications since PV panels have a material-specific spectral response. Spectrally resolved irradiance could be calculated by use of a new gnu-MAGIC clear sky model (R. Müller, personal communication). However, the application of the broad-band clear sky index for spectrally resolved irradiance would need to be evaluated. Especially at lower wavelengths, such as for UV radiation, the scattering of radiation in clouds increases and the broad-band all sky diffuse-to-direct radiation parameterization employed in Heliosat may not be applicable any more.

The simplified grid-scale radiation calculation could be extended to a sub-grid parameterization of topographic effects (*Helbig and Loewe, 2012*) which would also include a better treatment of terrain-reflected radiation (*Helbig et al., 2009, 2010*). The power of a subgrid-scale parameterization however strongly depends on the availability of realistic subgrid-scale boundary conditions such as surface albedo, cloudiness or the aerosol load.

## 17.7 Cloud Parallax

Cloud parallax occurs due to the slant viewing geometry of non-nadir Meteosat pixels. At 45° Longitude or Latitude this effect amounts in a geometric shift of up to 10 km (3 SEVIRI pixels or 8 HRV pixels) for 10 km high clouds. The correction of cloud parallax is thus important for the retrieval of instantaneous cloud physical properties or the Heliosat cloud index. It plays a lesser role in the climatological processing since geometrical errors very often compensate in time, except in mountain regions, where cloud locations are not random in space but strongly follow orographic features. Orthorectification and cloud parallax correction are both geometric corrections and could be performed in one single step. However, while orthorectification is a regular reprojection of a continuous field, cloud parallax correction needs to be applied only to a subset of all pixels (the clouds). The cloud parallax correction is currently implemented in “HelioMont”, but methods have to be developed that allow to fill the void area of cloud locations after clouds were geometrically displaced. Clouds may be displaced onto previously cloud-free pixels. A cloud parallax correction should also allow to combine displaced clouds with the underlying cloud-free surface area. Thus, while the geometric formulation of cloud parallax correction is straight forward its practical implementation is non-trivial. The benefit of cloud parallax correction for the retrieved instantaneous surface radiation fields would be larger for near real-time applications like the monitoring and nowcasting of solar energy production than for climatological applications.

## 17.8 Bias Correction

As demonstrated in the validation section, the mean bias error of satellite-derived surface radiation data versus the high quality ASRB station data is below  $\pm 5 \text{ W m}^{-2}$  on the daily, monthly and yearly time scale. This very low bias is in the order of the ground-based pyranometer instrument uncertainty. It would thus not justify the application of a station-based bias correction of the satellite-derived surface radiation fields. However, when considering the whole SMN station network, mean monthly biases for individual stations become as high as  $\pm 20 \text{ W m}^{-2}$ . These biases may depend on the station data accuracy and representativeness, so a de-biasing procedure would have to include a proper quality and suitability screening of station data. On sub-daily time scale mean absolute biases

strongly increase due to the different spatial and temporal coverage of the satellite measurement and the ground measurement. The mean bias error remains at a low value. On this time scale, a de-biasing would not help to remove the high random errors. As a first step a simple climatological de-biasing method using an inverse-distance weighted bias field for daily or monthly surface radiation fields could be evaluated. Based on these results a more complex geostatistical algorithms like kriging with external drift may be considered for de-biasing. Biases in the satellite-derived surface radiation can for instance arise due to missing snow detection, image registration, clear sky compositing, aerosol boundary conditions or subgrid-scale cloudiness. Most of these effects are strongly influenced by topography, so the de-biasing would likely have to take into account terrain elevation, slope and aspect as external fields to model the spatial bias distribution.

## 17.9 Uncertainties

Uncertainties for physical quantities calculated by “HeliMont” can be estimated by validating them with ground-observed quantities. Such a validation is not readily available for all variables (like cloud top height or solar radiation on an inclined plane) and it cannot be provided by grid point. Several parts of “HeliMont”, such as the cloud masking and clear sky compositing, already provide empirically derived uncertainty estimates for each grid point. These uncertainty estimates could be propagated to the downstream processing of physical quantities in order to provide a pixel-wise uncertainty estimate for variables such as direct normal irradiance. A pixel-wise uncertainty estimation is straight forward when physically-based radiative transfer models with the optimal estimation are used for all parts of the retrieval. The provision of pixel-wise uncertainty estimate would be of high benefit for applications like solar energy forecasting or climate model evaluation.



## 18 Applications

“HelioMont” surface radiation and cloud data are currently used in the following projects:

- EU Interreg project PV ALPS (<http://pvalps.eurac.edu>): Using “HelioMont” to derive publicly available solar energy assessments which help authorities to decide how solar energy can be exploited in the Swiss canton of Grisons and in the Italian region South Tyrol
- MeteoSwiss publishes monthly and annual means and anomalies of global radiation since 2004 as part of their climate monitoring activities ([http://www.meteoschweiz.admin.ch/web/en/climate/climate\\_today/swiss\\_climate\\_maps.html](http://www.meteoschweiz.admin.ch/web/en/climate/climate_today/swiss_climate_maps.html)).
- The solar cadaster of the Swiss city St. Gallen employed “HelioMont” data in its full time resolution of 15 minutes (<http://www.stadt.sg.ch/home/raum-umwelt/bauen-sanieren/energiefonds-foerderbeitraege/solaranlagen-strom/solarkataster.html>).
- The Meteonorm database (Version 7.0) includes monthly surface solar radiation components over Europe calculated by “HelioMont” at the MSG SEVIRI HRV resolution (Meteonorm by Meteotest AG, <http://meteonorm.com>).
- Short-term (6 hour) prediction of solar radiation for specific PV power plants (Mont Soleil and Stade de Suisse) in Bern, carried out by Meteotest AG and financed by BKW FMB Energie AG (<http://solforecastbkw.meteotest.ch>)
- Evaluation of the diurnal cycle of summer convection with COSMO-CLM by Michael Keller. CHIRP II funded PhD, Center for Climate Systems Modeling (<http://www.c2sm.ethz.ch/>).
- Climate research at the ETH Institute for Atmospheric and Climate Science (IACETH) by Wolfgang Langhans, Cathy Hohenegger and others (<http://www.iac.ethz.ch>).
- Solar cadaster covering the entire Switzerland (Project by the Federal Office of Energy BfE, The Federal Office of Meteorology and Climatology MeteoSwiss and Swisstopo)
- Evaluation of Sky Camera-based cloud detection performance by the Physikalisch Meteorologisches Observatorium Davos (PMOD)
- Analysis of the Geometric Accuracy of Satellite-Based Products of GCOS Switzerland by the ETH Institute for Geodesy and Photogrammetry ([https://www.rdb.ethz.ch/projects/project.php?proj\\_id=28997](https://www.rdb.ethz.ch/projects/project.php?proj_id=28997)).
- International Energy Agency (IEA) Solar Heating & Cooling (SHC) Programme, Task 46: Solar Resource Assessment and Forecasting. Intercomparison and validation of direct normal irradiance estimates from satellite retrievals (Pierre Ineichen, University of Geneva).

## Abbreviations

ASRB	Alpine Surface Radiation Budgetnetwork
AVHRR	Advanced Very High Resolution Radiometer (NOAA/Metop)
BRDF	Bidirectional Reflectance Distribution Function
BSRN	Baseline Surface Radiation Network
C2SM	Center for Climate Systems Modeling (ETH Zurich, Switzerland)
CDOP	Continuous Development and Operations Phase
CGIAR	Consultative Group on International Agricultural Research
CM SAF	Satellite Application Facility on Climate Monitoring
CGMS	Coordination Group for Meteorological Satellites
COSMO	Consortium for Small-scale Modeling
DN	Digital Number
DNI	Direct Normal Irradiance
DWD	German Weather Service
ECEF	Earth-Centered Earth-Fixed coordinate system
ECMWF	European Centre for Medium-Range Weather Forecasts
ECV	Essential Climate Variables
ETH	Federal Institute of Technology (Zurich, Switzerland)
EUMETCast	EUMETSATs flexible dissemination system for environmental data and products
EUMETSAT	European Organisation for the Exploitation of Meteorological Satellites
FCDR	Fundamental Climate Data Record (e.g. calibrated radiances)
FIFO	First-In First-Out
GCOS	Global Climate Observing System
GEWEX	Global Energy and Water Cycle Experiment

GOES	Geostationary Operational Environmental Satellite
GSHHS	Global, Self-consistent, Hierarchical, High-resolution Shoreline
GSICS	Global Space-based Inter-Calibration System (CGMS/WMO)
HIRS	High Resolution Infrared Radiation Sounder (on NOAA POES platforms)
HRV	SEVIRI High Resolution Visible Channel
IACETH	Institute for Atmospheric and Climate Research (ETH Zurich, Switzerland)
IASI	Infrared Atmospheric Sounding Interferometer (Metop)
IEA	International Energy Agency
IR	Infrared
ISCCP	International Satellite Cloud Climatology Project
LSA SAF	Land Surface Analysis Satellite Application Facility
LST	Land Surface Temperature (radiative)
LUT	Look Up Table
MAB	Mean Absolute Bias
MAGIC	Mesoscale Atmospheric Irradiance Code
MBE	Mean Bias Error
MFG	Meteosat First Generation
MLB	Modified Lambert-Beer equation
MSG	Meteosat Second Generation
MTG	Meteosat Third Generation
MVIRI	Meteosat Visible and Infrared Imager (MFG)
NASA	National Aeronautics and Space Administration (USA)
NDSI	Normalized Difference Snow Index
NIR	Near Infrared
NN	Nearest Neighbor
NOAA	National Oceanic and Atmospheric Administration (USA)
NWP SAF	Satellite Application Facility for Numerical Weather Prediction
PMOD	Physikalisch Meteorologisches Observatorium Davos
RTM	Radiative Transfer Model
SAF	Satellite Application Facility

SEVIRI	Spinning Enhanced Visible and Infrared Imager (MSG)
SIS	Surface Incoming Solar radiation
SPARC	Separation of Pixels using an Aggregated Rating over Canada
SSP	Sub-Satellite Point
SMN	SwissMetNet
SRTM	Shuttle Radar Topography Mission
TCDR	Thematic Climate Data Record (e.g. physical quantities)
ToA	Top of Atmosphere
TSI	Total Solar Irradiance
UNFCCC	United Nations Framework Convention on Climate Change
USGS	United States Geographical Survey
UTC	Universal Time Coordinate
UTM	Universal Transverse Mercator projection
VIS	Visible
VISSN	MVIRI visible channel
WCRP	World Climate Research Programme
WMO	World Meteorological Organization
WRC	World Radiation Center (PMOD, Davos Switzerland)
WV	Water Vapor

## List of Figures

Figure 1	Monthly Global Radiation Climatology for May (2004-2011, $\text{W m}^{-2}$ ) over Switzerland calculated from the MSG SEVIRI HRV channel and with a 100 m spatially resolved terrain model. . . . .	10
Figure 2	The classification tree (left) versus the aggregated rating (right) cloud masking method. . . . .	21
Figure 3	The cloud mask is used to separate clear sky from cloudy pixels. The clear sky visible reflectances and infrared brightness temperature fields including their uncertainty are successively used to model the diurnal course of clear sky reflectance and brightness temperature. These composited clear sky diurnal cycles in turn serve as the background fields for the next day's cloud masking. This method requires external model forcing only for spin-up and becomes self-consistent afterwards. . . . .	29
Figure 4	Meteosat clear sky reflectance (blue) and corresponding model fits to the cloud masked data of the last 10 days (orange) at four Alpine locations (see Table 3) on 5 August 2008. . . . .	32
Figure 5	Meteosat clear sky brightness temperatures (blue) and corresponding model fits to the cloud masked data of the last 10 days by use of the <i>Mannstein et al.</i> (1999) model (orange) at four Alpine locations (see Table 3) on 5 August 2008. . . . .	35
Figure 6	Meteosat clear sky brightness temperatures (blue) and corresponding model fits to the cloud masked data of the last 10 days by use of the <i>Göttsche and Olesen</i> (2009) model (orange) at four Alpine locations (see Table 3) on 5 August 2008. . . . .	37
Figure 7	Cloud anisotropy for water (left) and ice (right) clouds using a cloud optical thickness of 128, a sun zenith angle of $40^\circ$ and a surface albedo of 0.2. . . . .	43
Figure 8	Illustration of the geometrical relationships between the sun position and a tilted plane from an observer viewpoint on the earth's surface. . . . .	61
Figure 9	Illustration of the geometrical relationships between the sun position and the satellite position from an observer viewpoint on the earth's surface. . . . .	62
Figure 10	Monthly validation of the "HelioMont" global radiation mean absolute bias (mab, top panel) and mean bias error (mbe, bottom panel) with SwissMetNet. . . . .	82
Figure 11	Monthly comparison of direct beam (top), diffuse (middle) and direct normalized (bottom) solar irradiance with BSRN stations Payerne (left) and Carpentras (right) for the years 2004–2011. The shaded area represents the inter-annual variability (standard deviation of monthly values). . . . .	84
Figure 12	Hourly comparison of clear sky Global Radiation with ASRB (2004–2010). . . . .	88
Figure 13	Monthly inter-comparison of mean absolute bias (mab, top panel) and mean bias error (mbe, bottom panel) of the "HelioMont" global radiation with <i>Dürr and Zelenka</i> (2009) at ASRB sites. . . . .	90
Figure 14	Monthly inter-comparison of mean absolute bias (mab, top panel) and mean bias error (mbe, bottom panel) of the "HelioMont" global radiation with HelioClim 1 and 3 at ASRB sites. . . . .	92
Figure 15	Monthly inter-comparison of mean absolute bias (mab, top panel) and mean bias error (mbe, bottom panel) of the "HelioMont" global radiation with GEWEX SRB and ISCCP DX at ASRB sites. . . . .	94

Figure 16	Monthly inter-comparison of mean absolute bias (mab, top panel) and mean bias error (mbe, bottom panel) of the “HelioMont” global radiation with ECMWF ERA Interim at ASRB sites. . . . .	96
Figure 17	Monthly inter-comparison of mean absolute bias (mab, top panel) and mean bias error (mbe, bottom panel) of the “HelioMont” global radiation with the CM SAF MagicSol dataset at ASRB sites. . . . .	98
Figure 18	Monthly inter-comparison of mean absolute bias (mab, top panel) and mean bias error (mbe, bottom panel) of the “HelioMont” global radiation with the CM SAF operational dataset at ASRB sites. . . . .	99

## List of Tables

Table 1	Offset and scale factors for each of the SPARC scores. These factors are valid for the SEVIRI sensor and might need to be adjusted for other sensors. Most match the original AVHRR-based factors. . . . .	22
Table 2	Parameters of the clear sky reflectance model . . . . .	31
Table 3	Geographic locations of diurnal clear sky composites displayed in Figures 4, 5 and 6.	33
Table 4	Parameters of the <i>Mannstein et al. (1999)</i> model . . . . .	34
Table 5	Parameters of the <i>Göttsche and Olesen (2009)</i> model . . . . .	36
Table 6	Infrared cloud index parameter start values, lower and upper bounds and default values in the case of unsuccessful fitting. . . . .	45
Table 7	Empirical coefficients needed to calculate the equation of time and declination . .	61
Table 8	Inter-annual validation of the “HelioMont” Global Radiation with ASRB (2004–2010). $n$ = number of observations, $mbe$ = mean bias error, $mab$ = mean absolute bias, $r$ = Pearson correlation. Values marked with a (*) have a distinct local horizon influencing station measurements. . . . .	76
Table 9	Monthly validation of the “HelioMont” Global Radiation with ASRB (2004–2010). $n$ = number of observations, $mbe$ = mean bias error, $mab$ = mean absolute bias, $r$ = Pearson correlation, $ac$ = correlation of anomalies. Values marked with a (*) have a distinct local horizon influencing station measurements. . . . .	76
Table 10	Daily validation of the “HelioMont” Global Radiation with ASRB (2004–2010). $n$ = number of observations, $mbe$ = mean bias error, $mab$ = mean absolute bias, $r$ = Pearson correlation, $r^*$ = Pearson correlation of clear sky normalized values. Values marked with a (*) have a distinct local horizon influencing station measurements.	77
Table 11	Hourly validation of the “HelioMont” Global Radiation with ASRB (2004–2010). $n$ = number of observations, $mbe$ = mean bias error, $mab$ = mean absolute bias, $r$ = Pearson correlation, $r^*$ = Pearson correlation of clear sky normalized values. Values marked with a (*) have a distinct local horizon influencing station measurements.	77
Table 12	Inter-annual comparison of “HelioMont” Global Radiation with BSRN (2004–2011). $n$ = number of observations, $mbe$ = mean bias error, $mab$ = mean absolute bias, $r$ = Pearson correlation. . . . .	79
Table 13	Monthly validation of “HelioMont” Global Radiation with BSRN (2004–2011). $n$ = number of observations, $mbe$ = mean bias error, $mab$ = mean absolute bias, $r$ = Pearson correlation, $ac$ = correlation of anomalies. . . . .	79
Table 14	Daily comparison of “HelioMont” Global Radiation with BSRN (2004–2011). $n$ = number of observations, $mbe$ = mean bias error, $mab$ = mean absolute bias, $r$ = Pearson correlation, $r^*$ = Pearson correlation of clear sky normalized values. . . .	80
Table 15	hourly comparison of “HelioMont” Global Radiation with BSRN (2004–2011). $n$ = number of observations, $mbe$ = mean bias error, $mab$ = mean absolute bias, $r$ = Pearson correlation, $r^*$ = Pearson correlation of clear sky normalized values. . . .	80
Table 16	Validation of Global Radiation with SMN (2004–2011). $n$ = number of observations, $mbe$ = mean bias error, $mab$ = mean absolute bias, $r$ = Pearson correlation, $r^*$ = Pearson correlation of clear sky normalized values, $ac$ = correlation of anomalies.	81

Table 17	Monthly comparison of Direct Beam Radiation with BSRN (2004–2011). n = number of observations, mbe = mean bias error, mab = mean absolute bias, r = Pearson correlation. Values marked with a (*) have a suspicious seasonal cycle or unrealistic offsets in the station measurements. . . . .	85
Table 18	Monthly comparison of Diffuse Radiation with BSRN (2004–2011). n = number of observations, mbe = mean bias error, mab = mean absolute bias, r = Pearson correlation. Values marked with a (*) have a suspicious seasonal cycle or unrealistic offsets in the station measurements. . . . .	85
Table 19	Monthly comparison of Direct Normalized Irradiance with BSRN (2004–2011). n = number of observations, mbe = mean bias error, mab = mean absolute bias, r = Pearson correlation. . . . .	86
Table 20	Hourly comparison of clear sky Global Radiation with ASRB (2004–2010). n = number of observations, mbe = mean bias error, mab = mean absolute bias, r = Pearson correlation. . . . .	87



## References

- Anderson, G. P., S. A. Clough, F. X. Kneizys, J. H. Chetwynd, and E. P. Shettle (1986), Afgl atmospheric constituent profiles (0-120 km), *Environmental Research Papers, No. 954 AFGL-TR-86-0110*, Air Force Geophys. Lab., Hanscom Air Force Base, Bedford, MA 01731, USA.
- Babst, F., R. W. Müller, and R. Hollmarm (2008), Verification of ncep reanalysis shortwave radiation with mesoscale remote sensing data, *IEEE Geosci Remote S*, 5(1), 34–37, doi:10.1109/LGRS.2007.907537.
- Berrisford, P., D. Dee, K. Fielding, M. Fuentes, P. Kallberg, S. Kobayashi, and S. Uppala (2009), The era-interim archive version 1.0, *ERA Report Series 1*, ECMWF, European Centre for Medium Range Weather Forecasts Shinfield Park, Reading, Berkshire RG2 9AX, United Kingdom.
- Beyer, H., C. Costanzo, and D. Heinemann (1996), Modifications of the heliosat procedure for irradiance estimates from satellite images, *Sol Energy*, 56(3), 207–212.
- Buzzi, M. (2008), Challenges in operational numerical weather prediction at high resolution in complex terrain, Nr. 17714, ETH Zurich, doi:10.3929/ethz-a-005698833.
- Cano, D., J. Monget, M. Albuissou, H. Guillard, N. Regas, and L. Wald (1986), A method for the determination of the global solar-radiation from meteorological satellite data, *Sol Energy*, 37(1), 31–39.
- CM SAF (2010), Cloud physical products avhrr / seviri, *Algorithm Theoretical Basis Document 1.1*, Satellite Application Facility on Climate Monitoring.
- Coordination Group for Meteorological Satellites (1999), LRIT/HRIT global specification, *Tech. Rep. CGMS 03, Issue 2.6*, CGMS Secretariat EUMETSAT, Am Kavalleriesand 31, P.O.Box 100555, D-64205 Darmstadt, Germany.
- Cros, S., M. Albuissou, M. Lefevre, C. Rigollier, and L. Wald (2004), Helioclim: a long-term database on solar radiation for europe and africa, in *Proceedings of Eurosun 2004*, vol. 3, pp. 916–920, PSE GmbH, Freiburg, Germany.
- Dee, D. P., et al. (2011), The era-interim reanalysis: configuration and performance of the data assimilation system, *Q. J. R. Meteorol. Soc.*, 137, 553–597.
- Deneke, H. M., and R. A. Roebeling (2010), Downscaling of meteosat seviri 0.6 and 0.8  $\mu\text{m}$  channel radiances utilizing the high-resolution visible channel, *Atmospheric Chemistry and Physics*, 10(20), 9761–9772, doi:10.5194/acp-10-9761-2010.

- Dürr, B., and A. Zelenka (2009), Deriving surface global irradiance over the alpine region from meteosat second generation data by supplementing the heliosat method, *International Journal of Remote Sensing*, 30(22), 5821–5841.
- Dürr, B., A. Zelenka, R. Müller, and R. Philipona (2010), Verification of cm-saf and meteoswiss satellite based retrievals of surface shortwave irradiance over the alpine region, *International Journal of Remote Sensing*, 31(15), 4179–4198, doi:10.1080/01431160903199163.
- EUMETSAT (2000), The meteosat archive, format guide no. 1, basic imagery openmtp format, *Technical Report Revision 2.1*, Meteorological Archive and Retrieval Facility EUMETSAT, Am Kavalleriesand 31, D-64295 Darmstadt, Germany.
- EUMETSAT (2007a), A planned change to the msg level 1.5 image product radiance definition, *Tech. Rep. EUM/OPS-MSG/TEN/06/0519*, EUMETSAT Am Kavalleriesand 31, D-64295 Darmstadt, Germany.
- EUMETSAT (2007b), Typical geometrical accuracy for msg-1/2, *Tech. Rep. EUM/OPS/TEN/07/0313*, EUMETSAT Am Kavalleriesand 31, D-64295 Darmstadt, Germany.
- EUMETSAT (2008), On differences in effective and spectral radiance msg level 1.5 image products, *Tech. Rep. EUM/OPS-MSG/TEN/08/0161*, EUMETSAT Am Kavalleriesand 31, D-64295 Darmstadt, Germany.
- EUMETSAT (2010), MSG Level 1.5 Image Format Definition, *Technical Report EUM/MSG/ICD/105*, EUMETSAT, Eumetsat-Allee 1, D-64295 Darmstadt, Germany.
- EUMETSAT (2011), Meteosat first generation user handbook, *Tech. Rep. EUM/OPS/USR/10/1537, issue v1A*, EUMETSAT Eumetsat-Allee 1, D-64295 Darmstadt, Germany.
- EUMETSAT (2012a), Conversion from radiances to reflectances for seviri warm channels, *Tech. Rep. EUM/MET/TEN/12/0332*, EUMETSAT, Am Kavalleriesand 31, D-64295 Darmstadt, Germany.
- EUMETSAT (2012b), The conversion from effective radiances to equivalent brightness temperatures, *Tech. Rep. EUM/MET/TEN/11/0569*, EUMETSAT Am Kavalleriesand 31, D-64295 Darmstadt, Germany.
- Fontana, F. (2010), Evaluation of a probabilistic cloud masking algorithm for climate data record processing: Sparc: a new scene identification algorithm for msg seviri, *Visiting Scientist Report 14*, EUMETSAT Satellite Application Facility on Climate Monitoring.
- Fu, Q., P. Yang, and W. Sun (1998), An accurate parameterization of the infrared radiative properties of cirrus clouds for climate models, *Journal of Climate*, 11(9), 2223–2237.
- Funk, M. (1984), Räumliche verteilung der massenbilanz auf dem rhonegletscher und ihre beziehung zu klimaelementen, Diss. eth nr. 7643, ETH Zürich.
- Gautier, C., G. Diak, and S. Masse (1980), A simple physical model to estimate incident solar-radiation at the surface from GOES satellite data, *J. Appl. Meteorol.*, 19(8), 1005–1012.
- GCOS (2010), Implementation plan for the global observing system for climate in support of the UNFCCC, *Tech. Rep. GCOS-138 (GOOS-184, GTOS-76, WMO-TD/No. 1523)*, World Meteorological Organisation, Chairperson, Publications Board World Meteorological Organization (WMO) 7 bis, avenue de la Paix P.O. Box No. 2300 CH-1211 Geneva 2, Switzerland.

- GCOS (2011), Systematic observation requirements for satellite-based products for climate. 2011 update. supplemental details to the satellite-based component of the “implementation plan for the global observing system for climate in support of the unfccc (2010 update)”, *Report 154*, World Meteorological Organization, Chairperson, Publications Board World Meteorological Organization (WMO) 7 bis, avenue de la Paix P.O. Box No. 2300 CH-1211 Geneva 2, Switzerland.
- Gieske, A., J. Hendrikse, V. Retsios, B. van Leeuwen, B. Maathuis, M. Romaguera, J. Sobrino, W. Timmermans, and Z. Su (2005), Processing of msg - 1 seviri data in the thermal infrared - algorithm development with the use of the sparc2004 data set, in *Proceedings of the ESA WPP-250, SPARC final workshop, 4-5 July, 2005. Enschede : ESA, 2005.*, 8 pp.
- Goldberg, M., et al. (2011), The global space-based inter-calibration system, *Bulletin of the American Meteorological Society*, 92(4), 467–475, doi:10.1175/2010BAMS2967.1.
- Göttsche, F., and F. Olesen (2009), Modelling the effect of optical thickness on diurnal cycles of land surface temperature, *Remote Sensing of Environment*, 113(11), 2306–2316, doi:10.1016/j.rse.2009.06.006.
- Gupta, S. K., N. A. Ritchey, A. C. Wilber, C. H. Whitlock, G. G. Gibson, and P. W. S. Jr. (1999), Climatology of surface radiation budget derived from satellite data, *J. Clim.*, 12, 2691–2710.
- Gupta, S. K., P. W. S. Jr., S. J. Cox, J. C. Mikovitz, and T. Zhang (2006), 22-year surface radiation budget data set, *GEWEX NEWS*, 16(4), 12–13.
- Hammer, A., D. Heinemann, C. Hoyer, R. Kuhlemann, E. Lorenz, R. Muller, and H. Beyer (2003), Solar energy assessment using remote sensing technologies, *Remote Sensing of Environment*, 86(3), 423–432, doi:10.1016/S0034-4257(03)00083-X.
- Helbig, N., and H. Loewe (2012), Shortwave radiation parameterization scheme for subgrid topography, *Journal of Geophysical Research-Atmospheres*, 117, doi:DOI10.1029/2011JD016465.
- Helbig, N., H. Loewe, and M. Lehning (2009), Radiosity approach for the shortwave surface radiation balance in complex terrain, *Journal of the Atmospheric Sciences*, 66(9), 2900–2912, doi:DOI10.1175/2009JAS2940.1.
- Helbig, N., H. Loewe, B. Mayer, and M. Lehning (2010), Explicit validation of a surface shortwave radiation balance model over snow-covered complex terrain, *Journal of Geophysical Research-Atmospheres*, 115, doi:DOI10.1029/2010JD013970.
- Hu, Y., and K. Stamnes (1993), An accurate parameterization of the radiative properties of water clouds suitable for use in climate models, *Journal of Climate*, 6(4), 728–742.
- Ineichen, P., and R. Perez (1999), Derivation of cloud index from geostationary satellites and application to the production of solar irradiance and daylight illuminance data, *Theor Appl Climatol*, 64(1-2), 119–130.
- Ineichen, P., and R. Perez (2002), A new airmass independent formulation for the linke turbidity coefficient, *Sol Energy*, 73(3), 151–157.
- Ipe, A. (submitted), The gerb edition 1 products seviri scene identification - part i: Methodology, *IEEE Transactions On Geoscience and Remote Sensing*.

- Jarvis, A., J. Rubiano, A. Nelson, A. Farrow, and M. Mulligan (2004), Practical use of srtm data in the tropics – comparisons with digital elevation models generated from cartographic data, *Working Document 198*, Centro Internacional de Agricultura Tropical (CIAT), International Center for Tropical Agriculture, Apartado Aereo 6713 Cali, Colombia.
- Jimenez-Munoz, J. C., J. A. Sobrino, and C. Mattar (2012), Recent trends in solar exergy and net radiation at global scale, *Ecological Modelling*, *228*, 59–65, doi:DOI10.1016/j.ecolmodel.2011.12.027.
- Kasten, F. (1996), The linke turbidity factor based on improved values of the integral rayleigh optical thickness, *Solar Energy*, *56*(3), 239–244.
- Kasten, F., and A. T. Young (1989), Revised optical air mass tables and approximation formula, *Applied Optics*, *28*(22), 4735–4738.
- Kasten, F., K. Dehne, H. D. Behr, and D. Bergholter (1984), Spatial and temporal distribution of diffuse and direct solar radiation in germany, *Technical report Research Rept. No. T 84–125*, 128 pp., German Federal Ministry of Research and Technology,.
- Kato, S., T. Ackerman, J. Mather, and E. Clothiaux (1999), The k-distribution method and correlated-k approximation for a shortwave radiative transfer model, *Journal of Quantitative Spectroscopy & Radiative Transfer*, *62*(1), 109–121.
- Khlopenkov, K. V., and A. P. Trishchenko (2007), Sparc: New cloud, snow, and cloud shadow detection scheme for historical 1-km avhrr data over canada, *J Atmos Oceanic Tech*, *24*(3), 322–343, doi:10.1175/JTECH1987.1.
- Kinne, S. (2008), *Clouds in the perturbed climate system*, chap. Climatologies of cloud related aerosols: Particle number and size, ISBN: 978-0-262-01287-4, The MIT Press.
- Linke, F. (1922), Transmissions-koeffizient und truebungsfaktor, *Beitr. Phys. fr. Atmos.*, *10*, 91–103.
- Mannstein, H., H. Broesamle, C. Schillings, and F. Trieb (1999), Using a meteosat cloud index to model the performance of solar thermal power stations, in *The 1999 EUMETSAT Meteorological Satellite Data Users' Conference, 6-10 September 1999*, vol. EUM P 26, pp. 239–246, EUMETSAT, Copenhagen, Denmark.
- Marty, C., R. Philipona, C. Fröhlich, and A. Ohmura (2002), Altitude dependence of surface radiation fluxes and cloud forcing in the alps: results from the alpine surface radiation budget network, *Theoretical and Applied Climatology*, *72*(3), 137–155, doi:10.1007/s007040200019.
- Matsoukas, C. (2005), A new parameterisation for efficient and accurate look-up tables, *Cm saf visiting scientist report*, Department of Environment, University of the Aegean.
- Mayer, B., and A. Kylling (2005), Technical note: The libradtran software package for radiative transfer calculations - description and examples of use, *Atmospheric Chemistry and Physics*, *5*, 1855–1877.
- Morland, J., M. A. Liniger, H. Kunz, I. Balin, S. Nyeki, C. Matzler, and N. Kampfer (2006), Comparison of gps and era40 iuv in the alpine region, including correction of gps observations at jungfrauoch (3584 m), *J. Geophys. Res.-Atmos.*, *111*(D4), D04,102, doi:10.1029/2005JD006043.

- Möser, W., and E. Raschke (1984), Incident solar-radiation over europe estimated from meteosat data, *J Clim Appl Meteorol*, 23(1), 166–170.
- Müller, R., et al. (2004), Rethinking satellite-based solar irradiance modelling – the solis clear-sky module, *Remote Sensing of Environment*, 91(2), 160–174, doi:10.1016/j.rse.2004.02.009.
- Müller, R. W., C. Matsoukas, A. Gratzki, H. D. Behr, and R. Hollmann (2009), The cm-saf operational scheme for the satellite based retrieval of solar surface irradiance - a lut based eigenvector hybrid approach, *Remote Sensing of Environment*, 113(5), 1012–1024, doi:10.1016/j.rse.2009.01.012.
- Ohmura, A., et al. (1998), Baseline surface radiation network (bsrn/wcrp): New precision radiometry for climate research, *B Am Meteorol Soc*, 79(10), 2115–2136.
- Overpeck, J. T., G. A. Meehl, S. Bony, and D. R. Easterling (2011), Climate data challenges in the 21st century, *Science*, 331(6018), 700–702, doi:10.1126/science.1197869.
- Philipona, R. (2012), Greenhouse warming and solar brightening in and around the alps, *Int. J. Climatol.*, doi:10.1002/joc.3531.
- Philipona, R., C. Marty, C. Fröhlich, and A. Heimo (1996), Measurements of the longwave radiation budget in the alps, in *Current Problems in Atmospheric Radiation*, edited by W. Smith and K. Stamnes, DEEPAK, pp. 786–789, IRS.
- Pinker, R., and I. Laszlo (1992), Modeling surface solar irradiance for satellite applications on a global scale, *J. Appl. Meteorol.*, 31, 194–211.
- Posselt, R., R. Müller, R. Stöckli, and J. Trentmann (2011), Spatial and temporal homogeneity of solar surface irradiance across satellite generations, *Remote Sensing*, 3, 1029–1046, doi:10.3390/rs3051029.
- Posselt, R., R. W. Müller, R. Stöckli, and J. Trentmann (2012), Remote sensing of solar surface radiation for climate monitoring – the CM-SAF retrieval in international comparison, *Remote Sens. Environ.*, 118, 186–198, doi:10.1016/j.rse.2011.11.016.
- Poulsen, C. A., R. Siddans, G. E. Thomas, A. M. Sayer, R. G. Grainger, E. Campmany, S. M. Dean, C. Arnold, and P. D. Watts (2012), Cloud retrievals from satellite data using optimal estimation: evaluation and application to atsr, *Atmos. Meas. Tech.*, 5, 1889–1910, doi:10.5194/amt-5-1889-2012.
- Remund, J., L. Wald, M. Lefevre, T. Ranchin, and J. Page (2003), Worldwide linke turbidity information, *Proceedings of ISES Solar World Congress, 16-19 June 2003*, 1–13.
- Ricchiazzi, P., S. Yang, C. Gautier, and D. Sowle (1998), Sbdart: A research and teaching software tool for plane-parallel radiative transfer in the earth's atmosphere, *Bulletin of the American Meteorological Society*, 79(10), 2101–2114.
- Rigollier, C., O. Bauer, and L. Wald (2000), On the clear sky model of the esra – european solar radiation atlas - with respect to the heliosat method, *Sol Energy*, 68(1), 33–48.
- Rigollier, C., M. Lefevre, and L. Wald (2004), The method heliosat-2 for deriving shortwave solar radiation from satellite images, *Sol Energy*, 77(2), 159–169, doi:10.1016/j.solener.2004.04.017.

- Rossow, W., and E. Duenas (2004), The international satellite cloud climatology project (isccp) web site: An online resource for research, *B Am Meteorol Soc*, *85*, 167–172, doi:10.1175/BAMS-85-2-167.
- Schmetz, J., P. Pili, S. Tjemkes, D. Just, J. Kerkmann, S. Rota, and A. Ratier (2002), Seviri calibration, *B Am Meteorol Soc*, *83*(7), ES52–ES53.
- Schulz, J., et al. (2009), Operational climate monitoring from space: the eumetsat satellite application facility on climate monitoring (cm-saf), *Atmos Chem Phys*, *9*(5), 1687–1709.
- Simpson, J., and J. Stitt (1998), A procedure for the detection and removal of cloud shadow from avhrr data over land, *Ieee T Geosci Remote*, *36*(3), 880–897.
- Simpson, J., Z. Jin, and J. Stitt (2000a), Cloud shadow detection under arbitrary viewing and illumination conditions, *Ieee T Geosci Remote*, *38*(2), 972–976.
- Simpson, J., T. McIntire, Z. Jin, and J. Stitt (2000b), Improved cloud top height retrieval under arbitrary viewing and illumination conditions using avhrr data, *Remote Sensing of Environment*, *72*(1), 95–110.
- Skartveit, A., and J. Olseth (1987), A model for the diffuse fraction of hourly global radiation, *Sol Energy*, *38*(4), 271–274.
- Solomon, S., D. Qin, M. Manning, Z. Chen, M. Marquis, K. Avery, M. Tignor, and H. Miller (Eds.) (2007), *Intergovernmental Panel on Climate Change: Climate Change 2007: The Physical Science Basis. Contribution of Working Group I to the Fourth Assessment Report of the Intergovernmental Panel on Climate Change*, Cambridge University Press, Cambridge, United Kingdom and New York, NY, USA, 996 pp.
- Stamnes, K., S. Tsay, W. Wiscombe, and K. Jayaweera (1988), Numerically stable algorithm for discrete-ordinate-method radiative-transfer in multiple-scattering and emitting layered media, *Applied Optics*, *27*(12), 2502–2509.
- Stamnes, K., S.-C. Tsay, W. Wiscombe, and I. L. and (2000), Disort, a general-purpose fortran program for discrete-ordinate-method radiative transfer in scattering and emitting layered media: Documentation of methodology, *Tech. Rep. DISORT Report v1.1*, Dept. of Physics and Engineering Physics Stevens Institute of Technology Hoboken, NJ 07030.
- Stephens, L. G. (1994), *Remote Sensing of the Lower Atmosphere*, Oxford University Press, 523 pp.
- Swisstopo (2005), Approximate solution for the transformation ch1903 - wgs84, *Tech. rep.*, Bundesamt für Landestopografie swisstopo.
- Tan, B., R. Wolfe, J. Masek, F. Gao, and E. F. Vermote (2010), An illumination correction algorithm on landsat-tm data, in *Geoscience and Remote Sensing Symposium (IGARSS)*, pp. 1964–1967, IEEE International.
- Tarpley, J. D. (1979), Estimating incident solar-radiation at the surface from geostationary satellite data, *J. Appl. Meteorol.*, *18*(9), 1172–1181.
- USGS (1996), GTOPO30, Digital Media.

- Vollmer, M., and S. Gedzelmann (2006), Colours of the sun and moon: the role of the optical air mass, *European Journal of Physics*, 27, 299–309.
- Vonder Haar, T. H., and J. S. Ellis (1978), Determination of the solar energy microclimate of the united states using satellite data, *Final Report NASA Grant NAS5-22372*, Colorado State University.
- Wessel, P., and W. Smith (1996), A global, self-consistent, hierarchical, high-resolution shoreline database, *Journal of Geophysical Research-Solid Earth*, 101(B4), 8741–8743.
- Wild, M., A. Ohmura, H. Gilgen, and E. Roeckner (1995), Regional climate simulation with a high resolution gcm: surface radiative fluxes, *Climate Dynamics*, 11(8), 469–486.
- Wild, M., A. Ohmura, H. Gilgen, J. J. Morcrette, and A. Slingo (2001), Evaluation of downward longwave radiation in general circulation models, *J. Climate*, 14(15), 3227–3239.
- World Meteorological Organization (2008), Guide to meteorological instruments and methods of observation, *Tech. Rep. WMO-No. 8, Seventh Edition*, World Meteorological Organization.
- Zelenka, A., R. Perez, R. Seals, and D. Renne (1999), Effective accuracy of satellite-derived hourly irradiances, *Theor Appl Climatol*, 62(3-4), 199–207.
- Zhang, Y., W. Rossow, A. Lacis, V. Oinas, and M. Mishchenko (2004), Calculation of radiative fluxes from the surface to top of atmosphere based on isccp and other global data sets: Refinements of the radiative transfer model and the input data, *J Geophys Res-Atmos*, 109(D19), D19,105, doi:10.1029/2003JD004457.

## Acknowledgment

EUMETSAT and CM SAF are acknowledged for providing research funding during CDOP-1 used to develop several parts of the algorithms presented in this report. The documentation and validation were partly supported through the Interreg program IV Italy - Swiss by the European Funds for Regional Development (EFRE). MeteoSwiss, specifically the climate division, are greatly acknowledged for supporting “HelioMont” as part of their strategy to create and provide high quality Alpine climate data sets to the public. Bruno Dürr has built the initial version of a MSG processing framework suitable to derive solar irradiance over Alpine terrain. It served as a valuable starting point for developing “HelioMont”.

Many thanks go to Rebekka Posselt. Together with our DWD colleagues Richard Müller and Jörg Trentmann she has created the first climate data record of solar irradiance from Meteosat data spanning two satellite generations. The “MagicSol” dataset covers Europe and Africa and is publicly available at <http://wui.cmsaf.eu>. Several of the analysis scripts from Rebekka Posselt were used in the validation section. Christoph Frei is acknowledged for providing the map plotting routines used to generate the solar irradiance maps for Switzerland. The SODA service is acknowledged for providing the HelioClim-1 data. Jan Remund (Meteotest) is acknowledged for providing the HelioClim-3 data. EUMETSAT’s Satellite Application Facility on Climate Monitoring (CM SAF) is acknowledged for providing the CM SAF operational SIS data. The ISCCP DX data were obtained from the International Satellite Cloud Climatology Project data archives at NOAA/NESDIS/NCDC. Christian Steger has greatly helped to build the so-called Global Radiation Climate Analysis Tool (CAT) useful to extract climatological analyses from the complex set of gridded data created by “HelioMont”.

Finally, we are grateful to the careful internal and external review carried out by Laurent Vuilleumier (MeteoSwiss) and Anke Tetzlaff, Mariapina Castelli and Jochen Wagner (EURAC).







MeteoSchweiz  
Krähbühlstrasse 58  
CH-8044 Zürich

T +41 44 256 91 11  
[www.meteoschweiz.ch](http://www.meteoschweiz.ch)

MeteoSchweiz  
Flugwetterzentrale  
CH-8060 Zürich-Flughafen

T +41 43 816 20 10  
[www.meteoswiss.ch](http://www.meteoswiss.ch)

MeteoSvizzera  
Via ai Monti 146  
CH-6605 Locarno Monti

T +41 91 756 23 11  
[www.meteosvizzera.ch](http://www.meteosvizzera.ch)

MétéoSuisse  
7bis, av. de la Paix  
CH-1211 Genève 2

T +41 22 716 28 28  
[www.meteosuisse.ch](http://www.meteosuisse.ch)

MétéoSuisse  
Chemin de l'Aérologie  
CH-1530 Payerne

T +41 26 662 62 11  
[www.meteosuisse.ch](http://www.meteosuisse.ch)